2D Materials: Synthesis, Characterization, and Applications

Daniel A. Chenet

Submitted in partial fulfillment of the
Requirements for the degree
of Doctor of Philosophy
in the Graduate School of Arts and Sciences

COLUMBIA UNIVERSITY

2016

Abstract

2D Materials: Synthesis, Characterization, and Applications

Daniel A. Chenet

The isolation of monolayer graphene by Andre Geim and Konstantin Novoselov in 2004 created an explosion of layered materials research in the fields of condensed matter physics, material science, electrical engineering, chemistry, and nanobiology, to name a few. The applications have been broad from enhancing electrode performance in batteries to gas sensing to high-frequency analog flexible electronics. For several years and still to this day, graphene has provided a fertile ground for research due to its superior properties. However, failed efforts to engineer a substantial bandgap, a requirement for digital electronics, led researchers to look elsewhere in the periodic table for other layered materials with rich physics and an even broader application space. Fortunately, the technical expertise developed in the graphene system could, for the most part, be leveraged and modified in these new material systems.

This thesis presents a brief history of the field of two-dimensional electronics. The rediscovery - and it can only really be characterized as such since most of these materials were studied in the bulk form going back to the 1960s - of these two-dimensional materials with properties ranging from superconductivity, piezoelectricity, optical and electrical anisotropy, and large magnetoresistivity required the development of new characterization techniques to address the perturbations that accompanied the "thinning" of layers. Several characterization techniques were developed and are presented in this thesis. Moreover, in an effort to push these materials closer towards technological viability, synthesis techniques were developed that enabled the systematic study of a prototypical material system, molybdenum disulfide (MoS_2), in order to address the challenges that accompany scalability and determine the structure-property-function relationship.

Contents

List of Figures

List of Tables

Acknowledgments

I would like to acknowledge my fellow students, colleagues and advisors at Columbia University for their mentorship, support and the knowledge they shared with me, most specifically: Sunwoo Lee, Ghidewon Arefe, Nathan Finney, Dr. Yuanda Gao, Dr. Adam Hurst, Dr. Octavi Semonin, Dr. Zhengyi Zhang, Dr. Nick Petrone, Dr. Sasha Gondarenko, Professor Arend van der Zande, Professor Matteo Palma, Professor Jeffrey Kysar, Professor Colin Nuckolls, Professor John Kymissis, Professor James Im, Professor Arvind Narayanaswamy, and Professor James Teherani. I would especially like to thank Professor James Hone for his instruction, guidance, encouragement and friendship.

I've discovered that, in research, as well as in life, a change in scenery can do wonders in terms of gaining new perspective and seeing new angles. To that end, I also thank my colleagues at Army Research Laboratory. It was a pleasure working with and learning from Dr. Robert Burke, Matthew Chin, Dr. Sina Najmaei, Tyler Klarr, Daniel Rhodes, Dr. Barbara Nichols, Alex Mazzoni, and Dr. Madan Dubey.

Dedication

I would like to dedicate this work to my friends and family. To my friends, I thank you for making this long journey an enjoyable one. You dragged me out of the lab, probably kicking and screaming, when I needed to escape the most. To my family, I thank you for giving me your love and support always, but especially these last few years of graduate school. Specifically, I must thank my mother, Jeannie Mitchell, for always being a woman to whom I could look for whatever I needed. I have always been proud to be your son and much of what I do is to make you proud to be my mom. I also thank my maternal grandparents, Ralph and Adina Mitchell, for instilling within us all the importance of education and hard work, amongst many things. While your opportunities may have been limited, you made sure that we knew our potential was boundless. To my aunts and uncles, I thank you for being role models and for being the village that raised me. To my cousins, I thank you for being more like siblings. I know that we accomplish nothing in this life on our own. My success is your success.

CHAPTER 1

Introduction

1.1. Background

The explosion of research in two-dimensional (2D) materials came on the heels of the first isolation of graphene by Andre Geim and Konstantin Novoselov in 2004 [89]. Subsequent demonstrations of its superior electrical and mechanical properties created a wave of excitement, attracting researchers from the fields of condensed matter physics, electrical engineering, mechanical engineering, material science, chemistry, etc. The application space was and remains potentially broad for graphene; from high-speed analog circuits to conductive additives in composites to functionalized biosensors, it is a near certainty that graphene will find its way into industrial use. In addition to the much-deserved attention in its own right, graphene has served as the gateway to a broader and ever-expanding field of 2D materials. This class of materials includes the now ubiquitous transition metal dichalcogenides (TMDCs) and hexagonal boron nitride; but continues to expand and include layered perovskites, black phosphorus, silicene, and potentially many others. The solid-state electronic properties, and thus the potential application spaces, are extremely broad and diverse in these materials; and the major foci of academic research in this field are the determination of the ultimate limits of performance as well as the development of integration techniques in order to leverage these potentially disruptive material systems into previously inaccessible architectures and applications.

1.2. What are 2D Materials?

The most commonly-studied 2D materials are graphene and Group VI (molybdenum and tungsten) transition metal dichalcogenides. They are both characterized by a layer of

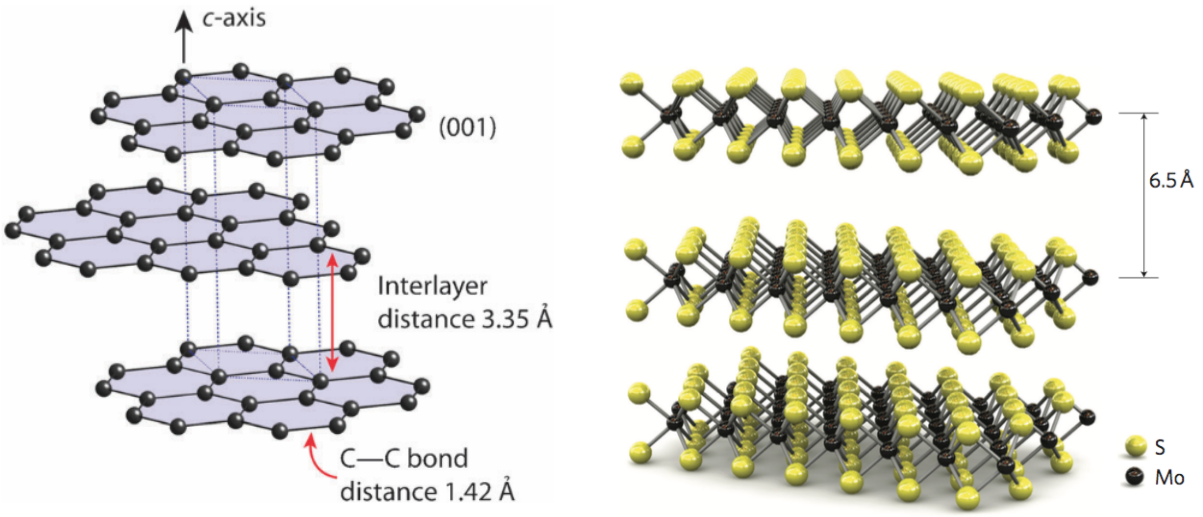

FIGURE 1.1. Ball and stick model for 3-layer graphene (left) and 3-layer MoS_2 (right). (Left) Single-layer graphene is held together by in-plane covalent sp2 carbon-carbon bonds. The interlayer separation is 3.35 Angstroms. Reproduced from [107]. (Right) Single-layer MoS_2has a center plane of trigonally-coordinated molybdenum atoms that are each bonded to 2 sulfur atoms above and below the plane. The interlayer separation is 6.5 Angstroms. Reproduced from [95]

in-plane, covalently-bonded atoms with weak out-of-plane van der Waals coupling between adjacent layers (see Figure 1.1). In the case of graphene, the single-atom-thick layer of carbon atoms are arranged in a hexagonal structure held together by strong sp2 covalent bonding. This structure leads to monolayer graphene's superior properties; namely, it has been shown to be the strongest material ever measured (10 times stronger than steel), more conductive than silver, and possesses highly mobile charge carriers that behave like massless Dirac fermions due to its linear dispersion at low energies [88, 58]. Once graphene transitions from monolayer to bilayer to a few layers, the bandstructure and, thus, the properties change - a recurring theme in this field.

Group VI transition metal dichalcogenides, however, exhibit multiple structures, albeit with different levels of stability, in just the X-M-X (chalcogen-transition metal-chalcogen) monolayer: hexagonal (2H), octahedral (1T), and distorted octahedral (1T') (see Figure

1.2) [13]. MoS_2, $MoSe_2$, WS_2, and WSe_2 are most stable in the hexagonal phase, which is semiconducting. Studies have shown that lithium intercalation, high doses of electron beam irradiation, and/or strain can be used to drive a transition into the 1T or 1T' phases [23, 72], which are both semi-metallic . This has been explored as a possible route to forming low-resistance electrical contacts to the semiconducting hexagonal phase with varying levels of success as well as a potential new material system for non-volatile memory applications. However, at room temperature, these phases are both very unstable and thus difficult to control and spatially manipulate. Another Group VI TMDC, $MoTe_2$, is also most stable in the hexagonal phase (α-phase) at room temperature; however, its monoclinic 1T' phase (β-phase) is also metastable at room temperatures [46]. WTe_2 is the largest departure from its Group VI counterparts as its room temperature phase is the semi-metallic, distorted octahedral phase (called 1T" due to its orthorhombic crystal structure) [13].

1.3. Why are they Interesting?

In general, the term "2D materials" is actually quite vague as there is a wide collection of materials that fall into this class with a broad range of properties. There are layered insulators, semimetals, small and moderate bandgap semiconductors [9, 77, 122]. There are layered materials, such as black phosphorus and ReS_2, that exhibit in-plane optical and electrical anisotropy [12, 74, 35, 122, 119, 37]. The 2H diatomic crystals, such as h-BN and MoS_2, possess nonzero piezoelectric coefficients in odd-numbered layers [20, 121, 131]. The only common thread amongst them all is that they possess strong covalent *intralayer* bonding with weak van der Waals *interlayer* coupling. This common thread simply means that the weak interlayer forces allow these bulk materials to be mechanically-exfoliated onto a substrate, isolating as few as one single monolayer, and so many of the techniques that were developed initially for the study of graphene can be, and have been, employed in these material systems. However, given that there are a wide range of properties exhibited in these

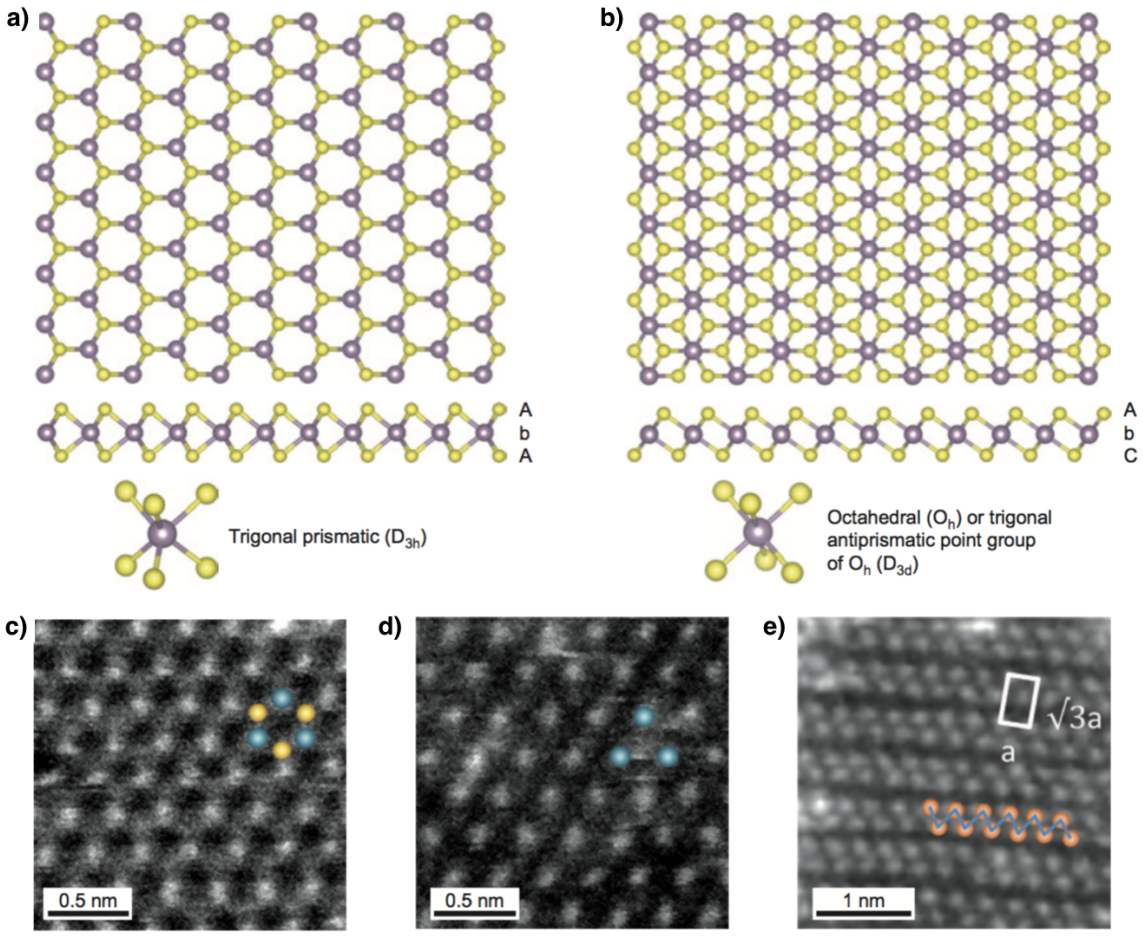

FIGURE 1.2. Monolayer structure of layered transition metal dichalcogenides. a) Hexagonal crystal structure, often referred to as 2H phase (trigonal prismatic D_{3h}). b) Octahedral structure (D_{3d}), often referred to as the 1T phase. c) and d) Transmission electron microscopy (TEM) image of the 2H and 1T phase. e) TEM image of another commonly observed structure referred to as distorted octahedral or 1T'. Reproduced from [13].

materials, it is useful to outline some of the more noteworthy properties in order to isolate particular areas where they may be able to close an existing technology gap:

(1) Superior elastic properties: strength and stiffness.

(2) Ultra-thin and flexible.

(3) Trap-free interfaces.

(4) Amenable to heterostructures.

(5) Strong light-matter interactions.

(6) Fertile ground for novel physics, such as the emerging field of valleytronics.

1.3.1. Elastic properties. Initial excitement over the elastic properties of 2D materials began with the early work of Lee, Kysar and Hone *et al.* in 2008. Their nanoindentation experiments measured the intrinsic elastic properties of free-standing graphene membranes prepared by mechanical exfoliation of nature graphite crystals. This work reported an effective Young's modulus of 1 TPa and an intrinsic breaking strength of 130 GPa at a strain of 25% [58]. Follow-up studies on graphene grown in large areas by chemical vapor deposition showed that grain boundaries that were still well-stitched were not significantly weaker than the pristine material [61].

Similar experiments performed on single domains of exfoliated and CVD-grown MoS_2 reported effective Young's moduli of 210 GPa and 264 GPa, respectively, with a breaking strength of 27 GPa at a strain of approximately 23% [75]. While notably weaker and less stiff than graphene, it is still quite remarkable for a 2D crystal. The remarkably high stiffness has motivated pursuits of tunable membrane resonators that operate at MHz frequencies [64, 73, 114]. The strain limits have motivated the integration of these materials into flexible electronics.

1.3.2. Flexibility. One of the application spaces where 2D materials probably hold the most promise is in flexible electronics. With in-plane strain limits on the order of 20%, they exceed the limits of conventional electronic materials. The field-effect mobilities in few-layer

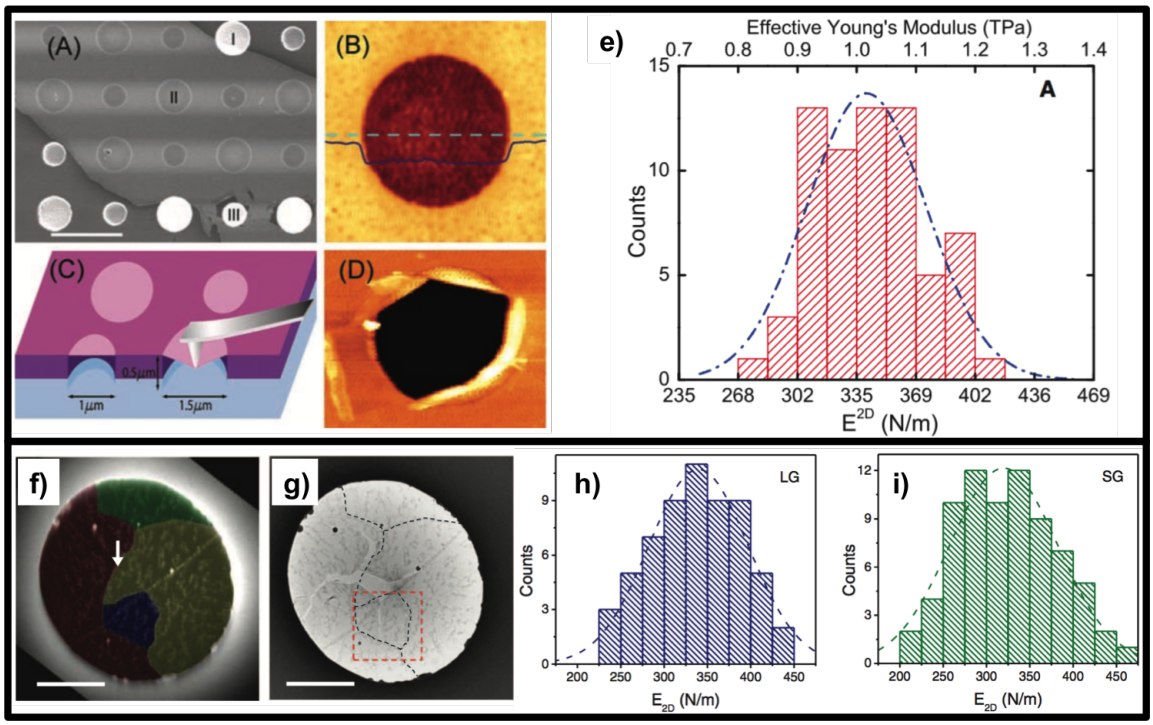

FIGURE 1.3. (a)-(e) Nanoindentation on pristine graphene prepared by mechanical exfoliation. Reproduced from [58]. (f)-(g) Nanoindentation of CVD graphene. LG and SG strand for "large grain" and "small grain", respectively. Reproduced from [61].

TMDCs are already competitive with doped metal oxides and organic semiconductors and they are being considered as potential candidates for semi-transparent thin film transistors (TFTs) in display technologies. Figures 1.4a and 1.4b illustrate that the TMDs and phosphorene are probably the most promising semiconductors for flexible digital logic applications [1]. In fact, high performance flexible devices and GHz frequency transistors have recently been demonstrated in separate reports on black phosphorus [132, 115].

1.3.3. Trap-free Interfaces. Another potential application for 2D materials is tunnel field-effect transitions (TFETs). TFETs are a potential low-power replacement to conventional transistors. They rely on quantum mechanical band-to-band tunneling instead of thermionic emission over a gate-modulated barrier in order to overcome the thermodynamic limits that plague conventional transistors. This would allow the transistors to be switched

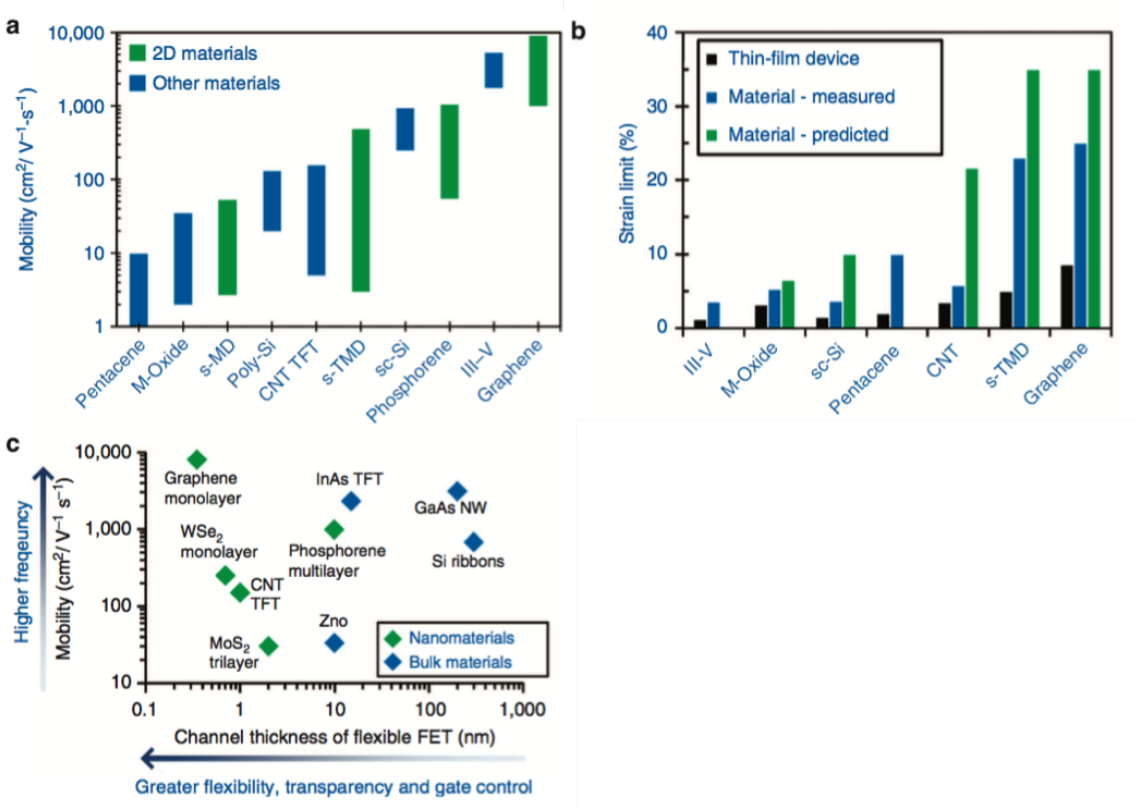

FIGURE 1.4. Performance comparison of layered materials and conventional semiconductors. (a) and (b) Mobility and strain limits for conventional semiconductors and 2D materials. (c) Mobility vs. channel thickness. Reproduced from [1].

on and off faster while dissipating less power. One impediment that limits conventional materials is the formation of interface traps between dissimilar materials that arise from lattice mismatches as well as the fact that 3D materials inherently have bonds out-of-plane. The absence of out-of-plane dangling bonds and atomically-thin form factors in 2D materials may promote the evolution of sub 60 mV/decade subthreshold swing transistors. In fact, a variation of this device has already been demonstrated (See Figure 1.5) in which the active device was a heterostructure of CVD-grown n-MoS_2 on bulk p-germanium [101]. This device, however, had performance limited by oxidation of the germanium – a problem that may be mitigated by the in-situ formation of a heterostructure TFET of all 2D materials, provided materials with the appropriate band offsets can be found.

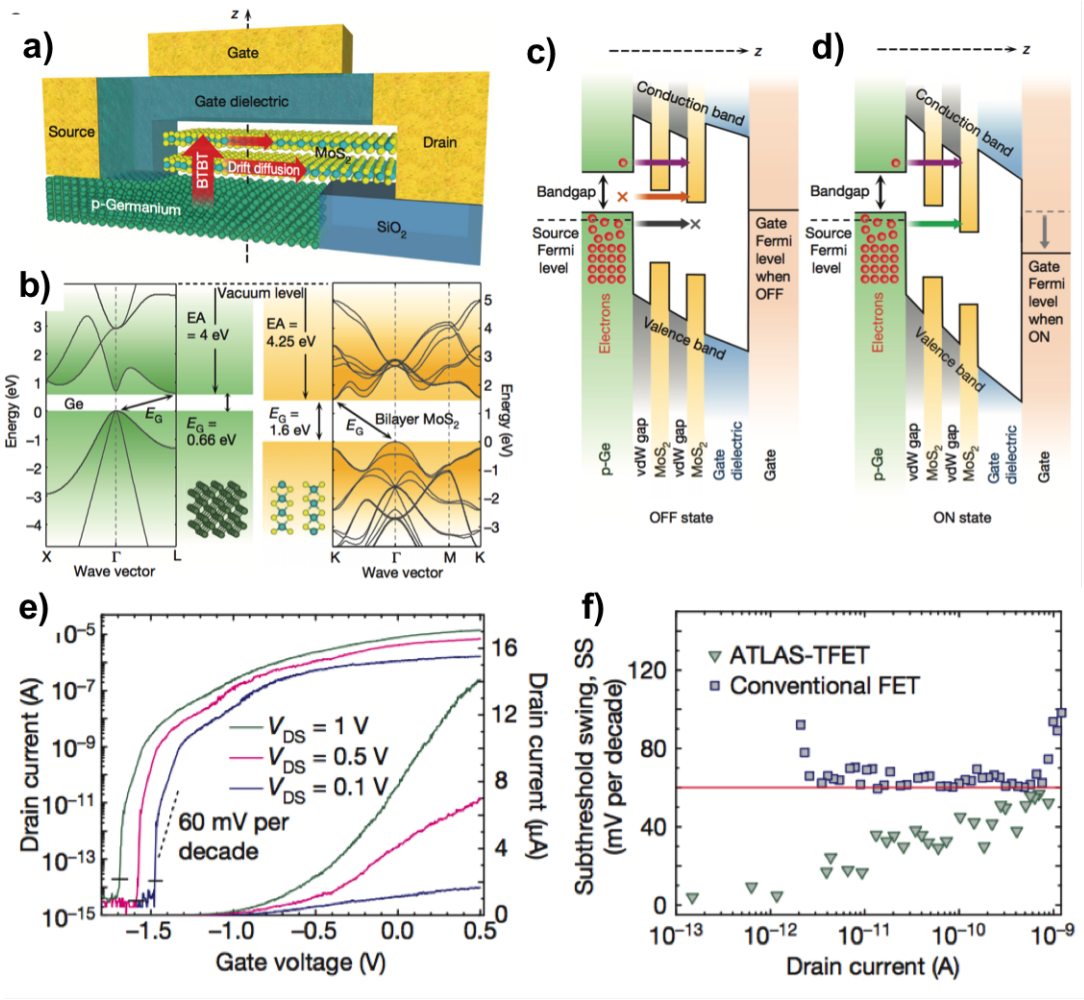

FIGURE 1.5. Bilayer on MoS_2 on germanium tunnel FET. (a) and (b) Schematic and band diagram representations of the device. (c) and (d) Band alignments in the OFF and ON states, respectively. (e) and (f) Transfer curve and comparison of subthreshold swing to conventional FET. Reproduced from [101].

1.3.4. Heterostructures. A trend in 2D materials research has been towards the formation of heterostructure architectures. There are several reasons for this:

(1) Improving carrier transport by isolating the channel from disorder and surface polar phonons that are everpresent in oxide dielectrics. This initally began with reports from Dean et al. and Wang et al. that demonstrated drastically improved performance in the electronic properties of graphene when using a layered h-BN dielectric

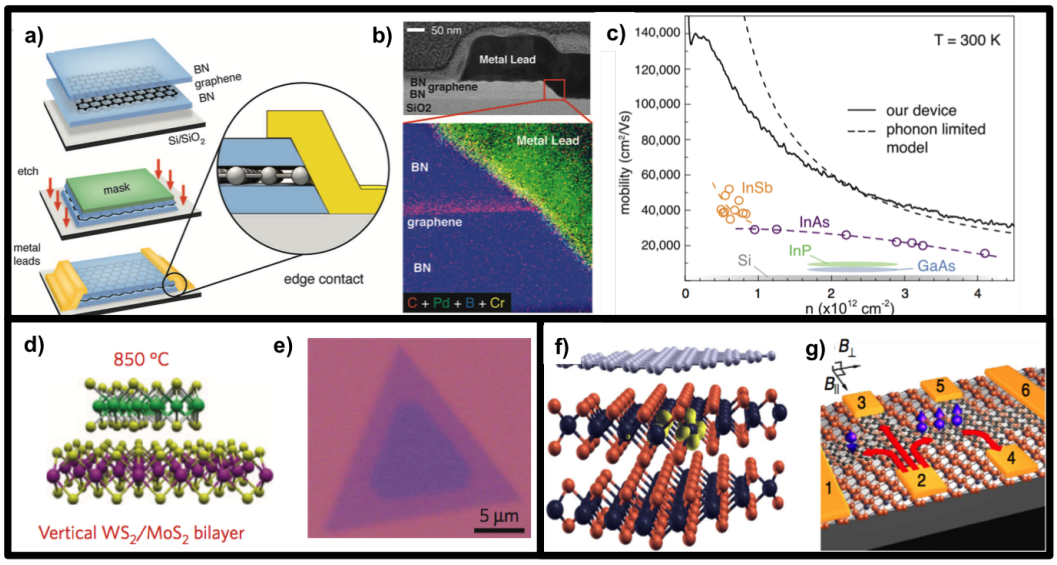

FIGURE 1.6. 2D material heterostructures. (a)-(e) hBN/graphene/hBN heterostructures with one-dimensional electrical contacts for ulta-high mobility transport. Reproduced from [116]. (d) and (e) CVD-grown vertical heterostructure of WS_2/MoS_2. Reproduced from [30]. (f) and (g) Spin-orbit coupling induced in graphene with a WS_2 substrate. Reproduced from [3].

[116, 17].

(2) Encapsulation of air-sensitive materials in air-stable h-BN in order to prevent degradation and boost performance [18].

(3) The formation of vertical heterojunctions that could enable light-harvesting and may provide a potential route towards band-to-band tunneling transistors, if the correct material stacks can be synthesized. This is particularly promising as there have been several reports of CVD-grown vertical structures of TMDCs [30].

(4) Using the properties of one material (strong spin-orbit coupling, for example) to induce novel physics in another by proximity [3].

1.3.5. Strong Light-Matter Interactions. One of the most remarkable properties of some of these 2D semiconductors are the extremely strong light-matter interactions they exhibit. The Group VI TMDCs absorb nearly 10% of incident photons in the visible range (see Figure 1.7) [70]. There are, of course, strong resonances at the direct optical transitions

(labeled A and B). It is quite remarkable that a monolayer (3-atoms thick) material is capable of that much absorption and it motivates their use in optoelectronics, potentially in high-speed photodetection and integrated onto on-chip photonic circuits.

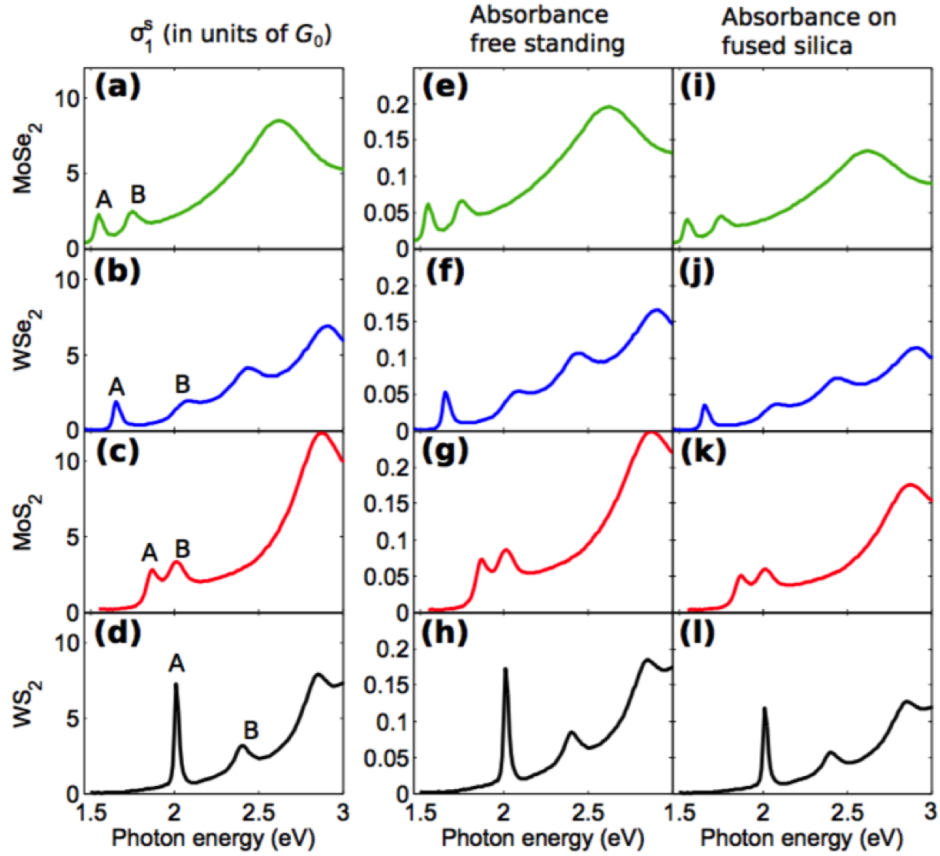

FIGURE 1.7. Absorbance of monolayer TMDCs. Reproduced from [70].

1.3.6. Novel Physics. Due to their non-centrosymmetric crystal structures and large spin-orbit coupling (band edge states composed primarly of transition metal d-orbitals), monolayer TMDCs have attracted significant interest for valleytronic applications. Valley-selective population adds a new degree of freedom, in addition to charge and spin, for the manipulation of charge carriers in semiconductors. Several studies on monolayer MoS_2 have demonstrated that, due to the coupling between valley and spin, helical excitation can selectively populate the K and K' valleys; left-handed circularly-polarized light creates excitons

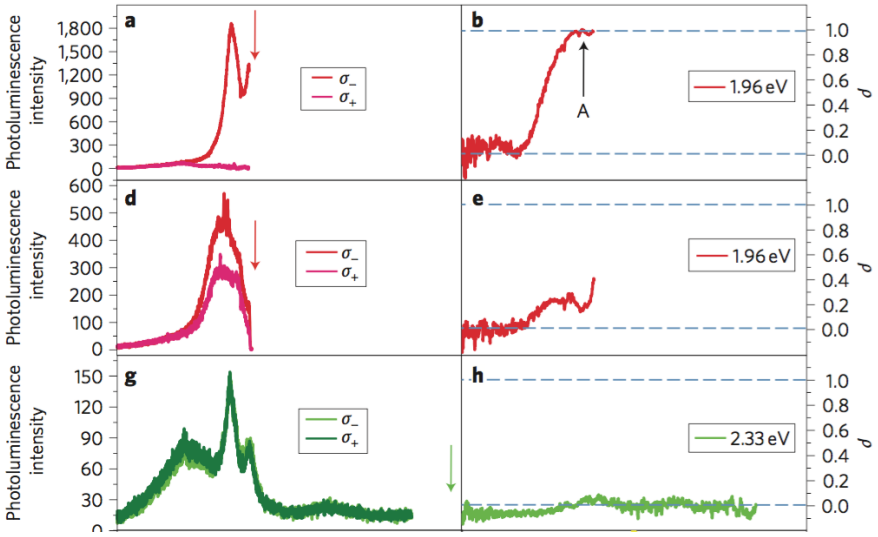

FIGURE 1.8. Polarization-resolved photoluminescence under left-handed circularly polarized excitation in 1L and 2L MoS_2. (a) and (b) PL spectra and helicity of 1L MoS_2 under excitation with 1.96 eV photons. (d) and (e) PL spectra and helicity of 2L MoS_2under excitation with 1.96 eV photons. (g) and (h) PL spectra and helicity of 1L MoS_2 under excitation with 2.33 eV photons. (b), (e), and (h) demonstrate that strong valley selectivity can be achieved with on-resonance excitation of the monolayer; while on-resonance excitation of bilayers and off-resonance excitation of monolayers result in weak to no selectivity, respectively. Reproduced from [80].

with electron spin down and hole spin at the K point and right-handed circularly-polarized light creates excitons with electron spin up and hole spin down at the K' point [81]. While it is not entirely clear how the valley selectivity in the monolayer can be manipulated, recent studies have also demonstrated that the valley selectivity in bilayer MoS_2 can be made tunable by using a gate electrode to break inversion symmetry [120, 65].

1.4. Advancing the Technology

In order to advance the 2D material technology, it is important to consider the phases of development required. Conventional CMOS technology has largely been following the ITRS (International Technology Roadmap for Semiconductors) that defines the performance goals and a timeline for them. However, silicon is a mature technology that has been around for

more than 30 years. It's properties and benefits are well-understood. The challenges it faces are mostly related to scaling limits; however, the ITRS was specifically created to ensure cooperation between all levels of the semiconductor industry with the goal of meeting these performance limits. The field of 2D materials, on the other hand, faces largely different challenges and, currently, lacks a consensus on what the long and short term goals should be. In order to motivate the following sections, a few of the major challenges are listed below:

(1) The field hasn't yet figured out which 2D materials have the electronic properties required to be implemented into functional devices. While graphene exhibits the highest carrier mobilities at room temperature, its lack of a bandgap precludes it from all digital logic applications. The ubiquitous Group VI TMDCs have rather low carrier mobilities at room temperature and are generally plagued by high contact resistances due to the current inability to intentionally dope the contact region. They may still have a future in TFETs, provided heterostructures with the appropriate band offsets can be made. Black phosphorus has high carrier mobilities at room temperature but it's environmental instability presents a challenge.

(2) Provided the appropriate materials and device architectures can be synthesized and demonstrated, there will need to be a careful characterization of the types of defects that will likely be unavoidable and how they will affect the performance of functional devices.

(3) Then, of course, there are the enormous challenges of scaling up the technology and obtaining a yield and reproducibility that will be competitive from an industrial perspective.

1.5. Outline

The purpose of this introduction was to give the reader a primer on the current status of the field of 2D nanoelectronics. However, when the work for this dissertation began 5 years

ago, little of what was presented was actually understood by the field. In 2010, graphene was receiving intense focus and the field had just discovered the indirect-to-direct bandgap transition in MoS_2. Much of what will be presented in this dissertation has helped to guide the trajectory of the field. It is also profoundly true that much of the work presented as part of this dissertation was influenced by the great work that was being done, simultaneously, by many research groups around the world. The remainder of this dissertation is organized in chapters as follows:

- Chapter 2: *Synthesis of 2D Materials.* This chapter will discuss the techniques by which 2D materials are generally prepared.
- Chapter 3: *Optical Characterization of 2D Materials.* This chapter will discuss optical spectroscopic techniques for characterizaing 2D materials. It will include some background theory and the derivation of some of the relevant physical equations.
- Chapter 4: *Characterization of Monolayer MoS_2 Grown by CVD.* This chapter will discuss the characterization of CVD-grown MoS_2 using a combination of techniques. It is a case study of what happens when we attempt to scale up 2D material technology. It seeks to probe the types and role of defects present in otherwise high-quality semiconductor material.
- Chapter 5: *Studies in Anisotropic TMDC ReS_2.* This chapter will discuss the characterization of ReS_2 by Raman, PL, and absorption spectroscopy. It is a case study on the anisotropic properties of some low-symmetry TMDCs.
- Chapter 6: *TMDC Alloys.* This chapter will discuss the characterization of TMDC alloys. This work was motivated by the pursuit of new phase-change materials as predicted by DFT calculations by Alexander Duerloo and Evan Reed at Stanford University and was performed in collaboration with Army Research Laboratory.
- Chapter 7: *2D Semiconductor Optoelectronics.* This chapter will discuss the performance of in-plane and out-of-plane optoelectronic devices fabricated using small-gap

layered semiconductors.

CHAPTER 2

Synthesis of 2D Materials

2.1. Chemical Vapor Deposition

Chemical vapor deposition (CVD) is a commonly used process to deposit thin films on a desired substrate. It involves using volatile precursors that can react or decompose onto a surface, yielding the desired material. There are several different versions of the CVD process, including low pressure CVD (LPCVD), plasma-enhanced CVD (PECVD), metal-organic CVD (MOCVD), and ambient pressure CVD (APCVD). They are used for depositing a wide range of materials, including polycrystalline silicon, silicon nitride, graphene, carbon nanotubes, and diamond. The process can sometimes be epitaxial where the desired material is deposited on a substrate that is nearly lattice-matched; however, deposition can also occur on amorphous substrates.

When this work began, most studies on TMDCs were on materials prepared by the mechanical exfoliation of bulk crystals. However, there were a couple of reports of depositing monolayer MoS_2 by chemical vapor deposition. Many of them were different variations on depositing molybdenum onto a substrate and annealing it at high temperature in the presence of sulfur, a carrier gas, and, sometimes, H_2. These methods, while successful at depositing MoS_2, usually produced very low quality material; the domain size was usually small (sub-micron) and they weren't able to preferentially grow monolayers.

In 2012, Lee *et al.* reported using solid precursors of sulfur and molybdenum trioxide (MoO_3) in an APCVD sytem using N_2 as a carrier gas [66]. They were able to grow ~10 micron sized domains on SiO_2 that they treated with seeding molecules. While our process was quite close to theirs, we did not use seeding molecules to nucleate the growth of monolayer

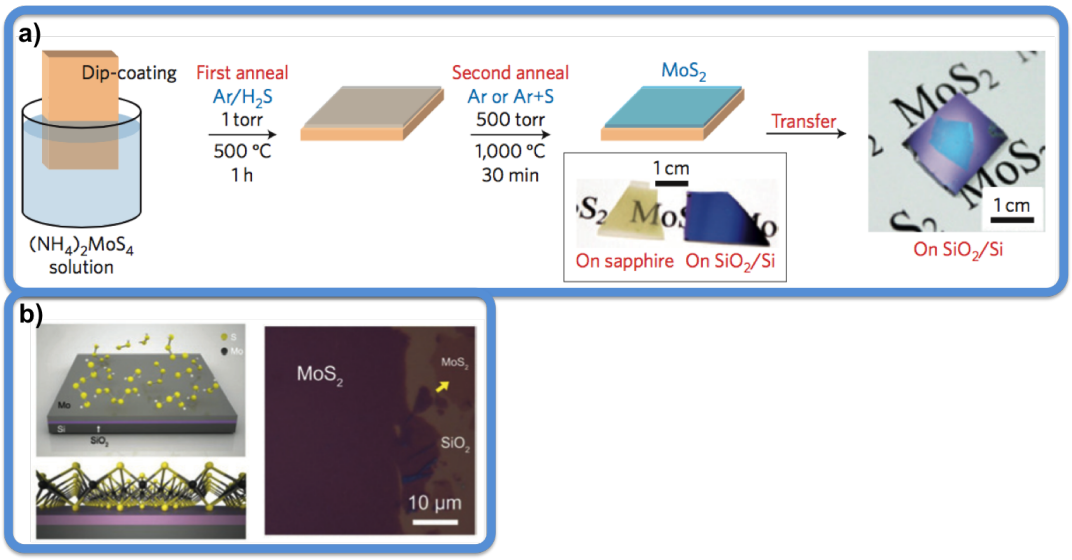

FIGURE 2.1. Other techniques for synthesizing MoS_2 by sulfurization of molybdenum films. (a) and (b) Reproduced from [76] and [128], respectively.

crystals. In fact, we found that the highest quality growths were achieved with meticulously cleaned substrates. The entire process is listed below.

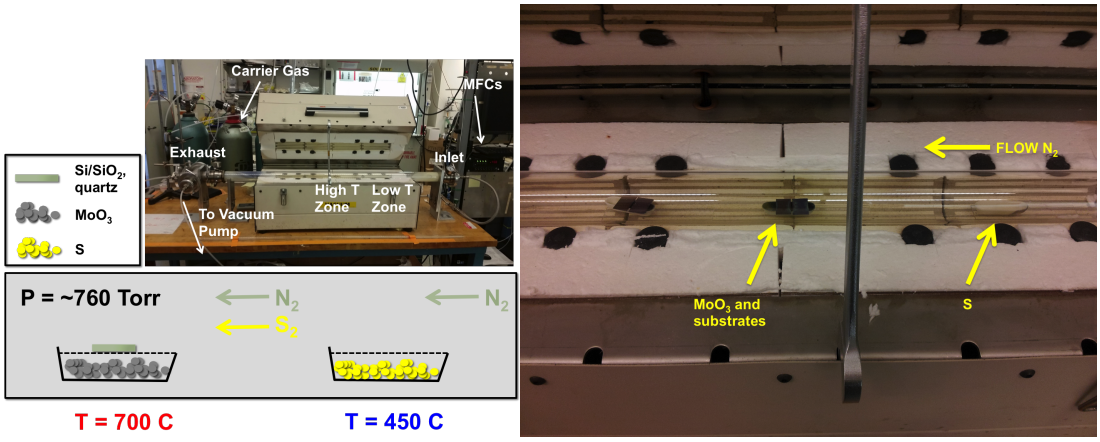

FIGURE 2.2. Schematic of MoS2 CVD Synthesis

Summary of Reaction.

- MoO_3 has a melting point of 795ºC and a low vapor pressure. Therefore, reactions would be expected to occur local to the solid powder. One option to circumvent this is to reduce the pressure inside the reaction chamber. However, sulfur has a high

vapor pressure and continuous pumping on the chamber would render controlling the amount of reactants impossible. The other option is to increase the volatility of the Mo reactant. MoO_3 is known to react with water vapor to form a more volatile species: $MoO_2(OH)_2$. However, this is undesirable as the presence of water in the reaction chamber alters the wetting dynamics on the substrate, promoting mostly nanoparticle growth. The best way is to use the sulfur itself as a reducing agent to form an intermediate MoO_{3-x} with increased volatility that may be further reduced into MoS_2 at the substrate surface. However, it is important to use the appropriate amount of sulfur in this method. Excess sulfur will result in the MoO_3 being completely reduced inside the crucible. Too little sulfur results in amorphous bulk deposition. Using the conditions below, the reaction is surface limited.

Substrate Preparation.

- Substrates were sonicated in acetone and isopropanol for 5 minutes each and then blow-dryed with N_2.
- Substrates were then soaked in a solution of 3:1 H_2SO_4:H_2O_2 for 1 hour; rinsed in deionized water; and then blow-dryed with N_2.

Precursor Preparation.

- 27 mg of MoO_3 (Sigma Aldrich) was loaded into an alumina boat.
- 130 mg of sulfur (Sigma Aldrich) was loaded into another alumina boat
- Note: it is important to store these precursors in a dry environment. They are hygroscopic and will quickly absorb water from a humid environment. When this occurs, monolayer growth will be impossible - only nanoparticles will nucleate.

Loading.

- The KF connectors on the exhaust side are removed so that precursors can be loaded from that side.

- The sulfur crucible is placed on a quartz slide and loaded into the fused quartz tube into the zone labeled "Low T Zone" using a quartz push rod.
- The MoO_3 crucible with a growth substrate placed over the top is loaded onto another quartz slide and they are carefully pushed into the "High T Zone" with the rod.
- The system is reconnected and the lid is closed.

Anneal.

- The system is slowly ramped to 105^{o}C and held there for 3 hours while the mass flow controllers (MFCs) are set to allow 500 sccm of N_2 to flow through the system.
- Note: the gas is flowing through the system and into an oil bubbler at the exhaust end. The purpose is to prevent the back-diffusion of oxygen and water vapor.
- Note: the Low T Zone must stay significantly below the melting point of sulfur (115^{o}C). Otherwise, there will be massive amounts of sulfur lost due to its high vapor pressure.

Ramp 1.

- The N_2 flow rate is dropped to 20 sccm.
- The system is ramped to 700^{o}C at a rate of 30^{o}C/min.
- Note: 700^{o}C is the temperature of the High T Zone. Since this is a single zone furnace, we do not have independent control over the 2 zones. However, when the High T Zone is at 700^{o}C, the Low T Zone is at ~450^{o}C.

Soak 1.

- The system is held at 700^{o}C for 5 minutes.

Cooling.

- The system is allowed to cool naturally to 590^{o}C, which takes about 19 minutes in this system.

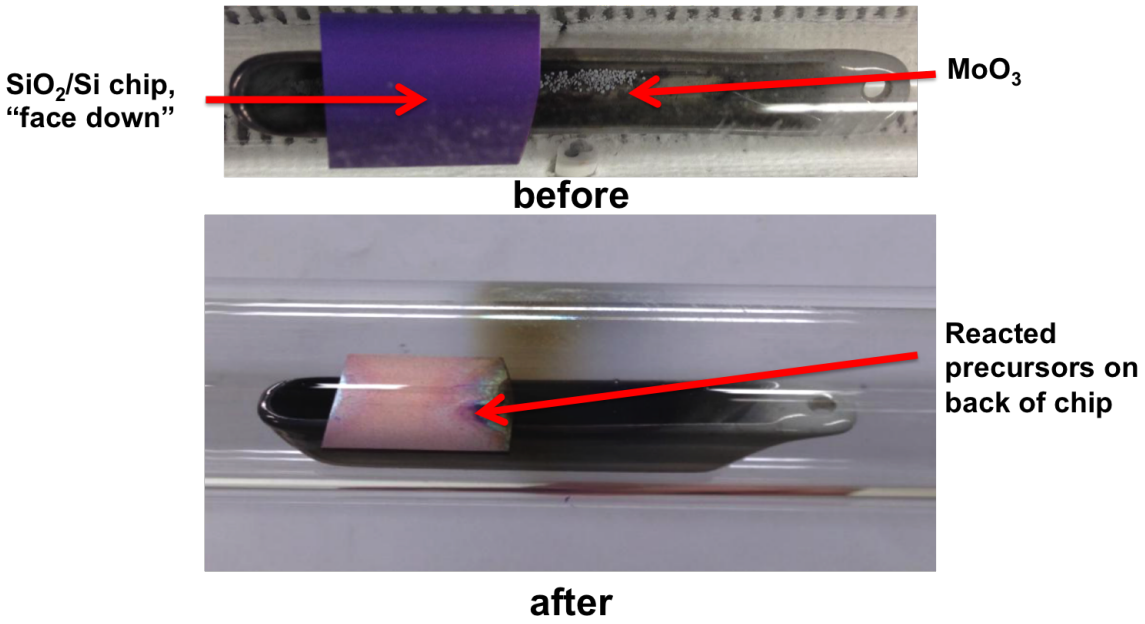

FIGURE 2.3. Optical image of a chip sitting above the MoO_3 crucible before and after the growth process.

Soak 2.

- The system is held at 590^{o}C for 5 minutes.

Quench.

- The temperature controller was set to room temperature; the N_2 flow was turned up to 500 sccm; and the lid to the furnace was opened for rapid cooling.

Results. At the end of the process, there will be noticeable amounts of bulk deposition on the backside (top) of the chip as well as in regions immediately above the crucible. There will be a region on the edges with continuous monolayer regions that transition into isolated domains (see Figure 2.4). Characterization of these isolated domains, as well as the regions where they merge together, will be discussed in Chapter 4.

FIGURE 2.4. Optical images of growth substrate at low (left) and high (right) magnifications.

CHAPTER 3

Optical Characterization of 2D Semiconductors

3.1. Raman Spectroscopy

3.1.1. Force Constant Model. Raman spectroscopy is one of the most powerful tools for characterizing crystalline materials. It has proven to be especially powerful in the study of layered materials, such as graphene, nanowires, and transition metal dichalcogenides [28, 31, 40, 43, 100, 109, 118, 119, 123]. In order to gain a better understanding of how to employ this spectroscopic technique, it is important to gain a physical understanding of what exactly is being probed. In general, most explanations of Raman spectroscopy, including the one given by Perkowitz [92], first consider vibrations in individual molecules before developing a treatment for crystals, which will also be our strategy. To this end, we first examine the force constant model as applied to a diatomic molecule [92]. We begin by considering two atoms of masses m_1 and m_2 that are positioned distances r_1 and r_2 from the center of gravity as depicted in Figure 3.1.

The equilibrium separation between the two atoms would therefore be $r_1 + r_2$ and the

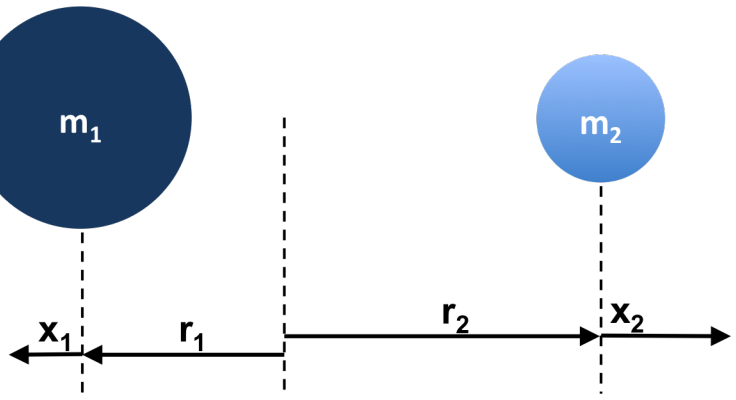

FIGURE 3.1. Center of masses in force constant model.

displacements of the two atoms are given by x_1 and x_2. The conservation of the center of gravity gives rise to equation 3.1:

$$m_1 r_1 = m_2 r_2$$

$$m_1(r_1 + x_1) = m_2(r_2 + x_2)$$

$$x_1 = \frac{m_2}{m_1} x_2 \tag{3.1}$$

If we next consider the restoring force determined by the displacements of the two atoms, we obtain equation 3.2:

$$F = -K(x_1 + x_2)$$

$$F = -K(\frac{m_2 + m_1}{m_1})x_2 = -K(\frac{m_1 + m_2}{m_2})x_1 \tag{3.2}$$

, where K is the force constant, also referred to as "stiffness". Combining 3.2 with Newton's 2nd law $\sum F = ma$, we obtain the equation for a 2-body classical mechanical system:

$$\frac{m_1 m_2}{m_1 + m_2}(\ddot{x}_1 + \ddot{x}_2) = -K(x_1 + x_2) \tag{3.3}$$

. Now we let $q = x_1 + x_2$, where q is the relative displacement, and $\mu = \frac{m_1 m_2}{m_1 + m_2}$, where μ is the effective mass. This yields equations 3.4 and 3.5:

$$\mu \ddot{q} = -Kq \tag{3.4}$$

$$\nu_0 = \frac{1}{2\pi}\sqrt{\frac{K}{\mu}} \tag{3.5}$$

, where ν_0 is the classical fundamental frequency of vibration. Now, it is important to note that this frequency of vibration was completely derived using classical mechanics for a simple harmonic oscillator. Although not derived here, the same frequency can be obtained using

quantum mechanics by solving Schrodinger's equation with a parabolic potential energy. There are, however, a few differences between the two approaches. The difference that is most important here is that the energy in a classical mechanical harmonic oscillator can change continuously, while the energy in a quantum mechanical harmonic oscillator can only change in discrete steps of hv.

Another clarification that must be made is that the motion of a diatomic molecule cannot be accurately described as a simple harmonic oscillator. In fact, the vibration is anharmonic and is best described by the Morse potential, which is given as:

$$V = D_e(1 - e^{-\beta q})^2 \tag{3.6}$$

, where D_e and β denote the bond dissociation energy and curvature at the bottom of the potential well, respectively. Both the harmonic (parabolic) and anharmonic (Morse) potentials are depicted in 3.2.

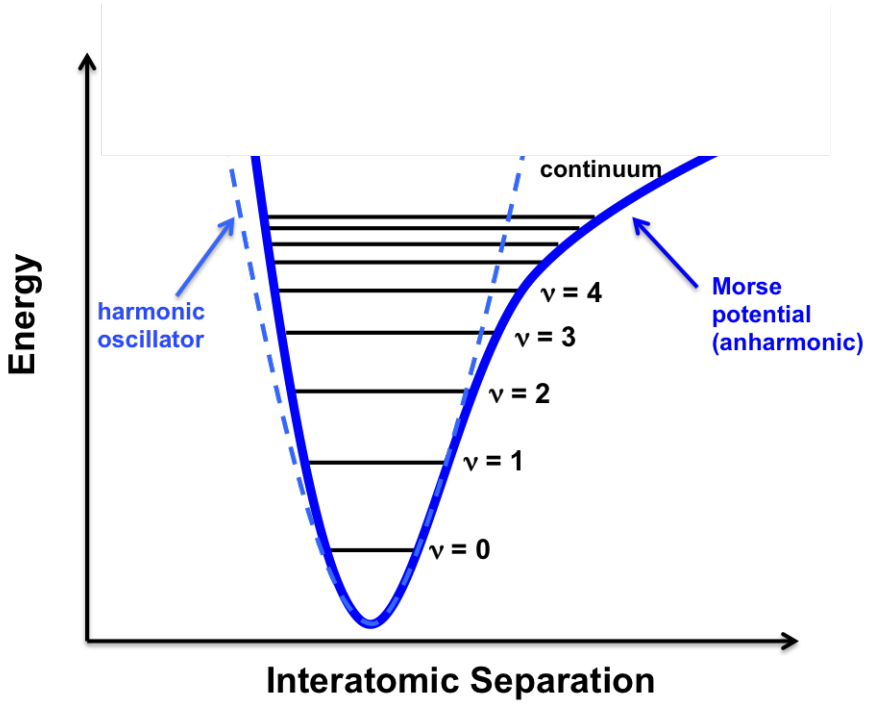

FIGURE 3.2. Potential wells for harmonic and anharmonic oscillators

The anharmonicity of the Morse potential gives rise to the existence of overtones ($v = 1, 2, 3, \ldots$), the relative population of which will be discussed later. Additionally, the solution of Schrodinger's equation using the Morse potential, rather than a parabolic potential, yields frequencies that are no longer equally spaced in energy by $h\nu$.

There are several important points in the preceding discussion that are critical to developing an intuition about the vibrations in molecular systems. The first is the dependence of the vibrational frequency on both the effective mass and stiffness of the system. One would expect that a decrease in stiffness or increase in mass would result in a red-shift in the vibration frequency. These are important when considering the shifts that are expected when a system is subjected to changes in temperature, strain, composition, etc. Additionally, the existence of overtones in an anharmonic oscillator should produce observable signals at different frequencies. While we have only discussed molecules to this point, these conclusions are also valid in crystals. Now that we have developed an understanding for the frequencies associated with vibrations in a molecule or crystal, it is important to understand how we may seek to observe them experimentally using Raman spectroscopy.

3.1.2. Electromagnetics and Selection Rules. To first order, the Raman response of a diatomic molecule under laser excitation can be described using classical electromagnetic theory. The incident radiation from a laser can be treated as an electromagnetic wave with oscillating electric field described by equation 3.7:

$$E = E_0 cos(2\pi\nu_0 t) \tag{3.7}$$

, where E_0 and ν_0 are the magnitude and frequency of the electromagnetic radiation, respectively. If this electromagnetic radiation is incident upon a diatomic molecule, it will induce a dipole moment given by equation 3.8:

$$P = \alpha E = \alpha E_0 cos(2\pi\nu_0 t) \tag{3.8}$$

, where α is the polarizability. Next, we consider a molecule vibrating at frequency ν_m with a nuclear displacement q given by equation 3.9:

$$q = q_0 cos(2\pi\nu_m t) \tag{3.9}$$

. For small vibrations, α is a linear function of q and can be approximated by equation 3.10:

$$\alpha = \alpha_0 + \left(\frac{\partial\alpha}{\partial q}\right)_0 q_0 + \dots \tag{3.10}$$

, where α_0, q_0, and $\left(\frac{\partial\alpha}{\partial q}\right)_0$ are all evaluated at the molecule's equilibrium position. Combining equations 3.8, 3.9, and 3.10 produces equation 3.11:

$$P = \alpha E = \alpha E_0 cos(2\pi\nu_0 t)$$

$$P = \alpha_0 E_0 cos(2\pi\nu_0 t) + \left(\frac{\partial\alpha}{\partial q}\right)_0 q_0 E_0 cos(2\pi\nu_0 t) cos(2\pi\nu_m t) + \dots$$

$$P = \alpha_0 E_0 cos(2\pi\nu_0 t) + \frac{1}{2}\left(\frac{\partial\alpha}{\partial q}\right)_0 q_0 \left[cos\left\{2\pi(\nu_0 + \nu_m)t\right\} + cos\left\{2\pi(\nu_0 - \nu_m)t\right\}\right] + \dots \tag{3.11}$$

.

The first term in equation 3.11 corresponds to Rayleigh scattering, which has a frequency equal to the excitation. The second and third terms correspond to anti-Stokes (higher frequency than excitation) and Stokes (lower frequency than excitation) Raman scattering, respectively. Analogous to classical mechanical systems, molecules have multiple vibrational modes and it can be seen from equation 3.11 that a requirement for a specific vibrational mode to be Raman-active is for $\left(\frac{\partial\alpha}{\partial q}\right)_0 \neq 0$. In other words, only vibrations that change the polarizability of the molecule can be Raman-active. To further illustrate this point, we turn to the prototypical example of CO_2.

A molecule with N atoms has 3N degrees of freedom, since each atom can move in 3 directions. Six of these degrees of freedom involve translations and rotations about the prin-

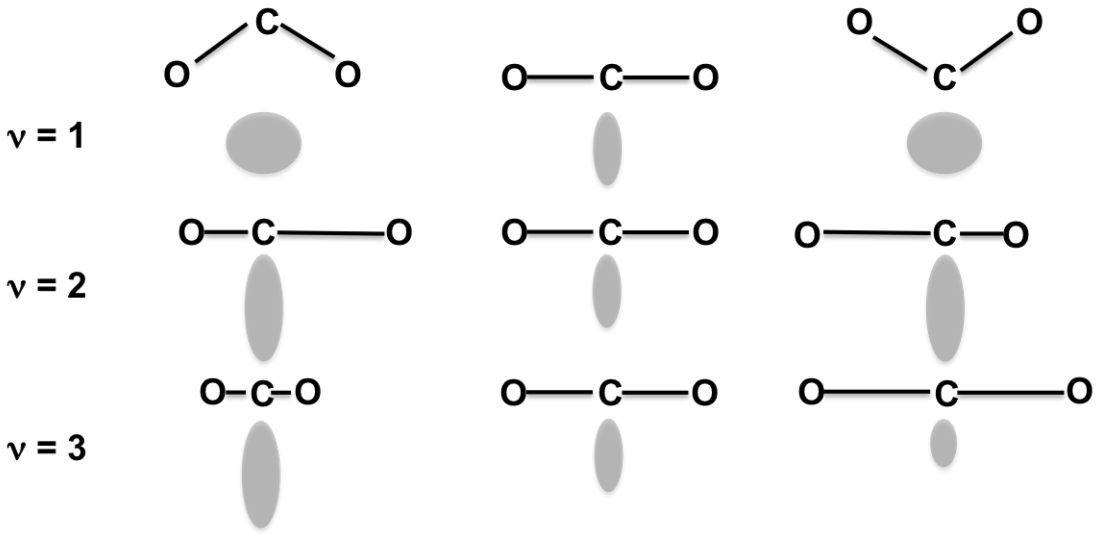

FIGURE 3.3. Change in polarizability ellipsoids for vibration modes in a CO_2 molecule.

cipal axes. However, in the case of linear molecules like CO_2, rotations about the molecule's axis do not exist. Therefore, it is expected that CO_2 has 3N-5 vibrational modes. These vibrational modes correspond to two doubly-degenerate symmetric bending modes ($\nu = 1$), an asymmetric stretching mode ($\nu = 2$), and a symmetric stretching mode ($\nu = 3$), all of which are depicted in 3.3. It can be seen that only the symmetric stretching mode produces a change in the polarizability ellipsoid (grey shaded regions) with small vibrations about the equilibrium position. Consequently, only vibrational mode ($\nu = 3$) is Raman-active.

3.1.3. Associated Energy Levels. Essential to the interpretation of Raman spectra is an understanding of the energy levels involved in Raman scattering. A molecule may be excited by incident radiation into what is sometimes referred to as a "virtual state" and, upon relaxation, will emit a photon when it reaches it's final state, which may be equal (Rayleigh), higher (Stokes), or lower (anti-Stokes) in energy than the initial state, schematically-represented in 3.4.

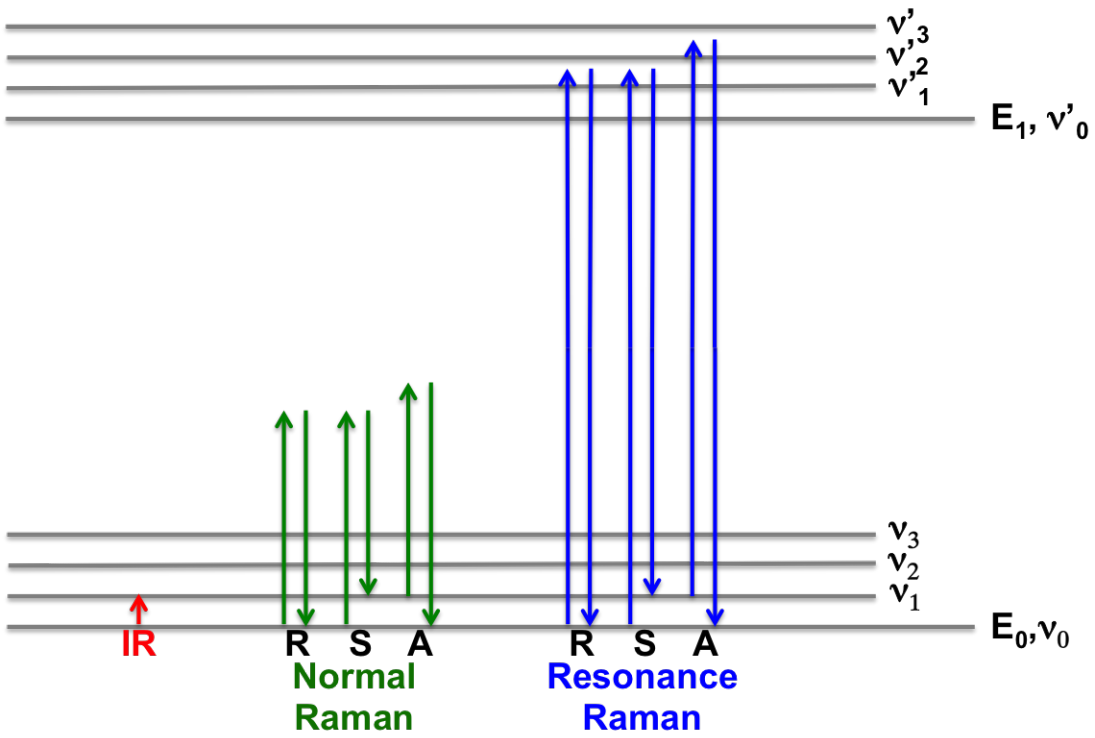

FIGURE 3.4. Schematic depicting energy levels for Raman scattering. R, S, and A denote Rayleigh, Stokes, and anti-Stokes scattering, respectively.

The probability that the molecule is initially in its vibrational ground state ($\nu = 0$) or a higher energy state (Ex. $\nu = 1$) depends upon temperature and is determined by a Maxwell-Boltzmann distribution. This fact has been used in numerous experiments to determine the temperature of a crystal by comparing the relative intensities of Raman signals corresponding to the Stokes (lower energy initial state) and anti-Stokes (higher energy initial state) scattering. However, in most experiments, particularly the ones presented in this dissertation, focus is directed towards Stokes scattering. This is largely due to both the higher probability of Stokes scattering (higher probability of molecules in lower energy state) as well as the ability and cost to obtain the proper optical filters to facilitate the experiment.

3.1.4. Raman Tensor. It is important to note that the quantities in equations 3.7 - 3.11 are directional; P, E and q are more accurately denoted $\overrightarrow{P}$, $\overrightarrow{E}$, and $\overrightarrow{q}$. The polarizability, α,

is actually a symmetric tensor, $\widetilde{\alpha}$. The Raman tensor, $\widetilde{R}$, is defined as the derivative of the polarizability tensor and, in general, is unique to a given vibration mode for a given crystal with a given point group symmetry (discussed later). The intensity observed when a laser is incident upon a crystal and interacts with one of its vibration modes can be described by equation 3.12:

$$I \propto |\hat{e}_i \cdot \widetilde{R} \cdot \hat{e}_s|^2 \tag{3.12}$$

, where $\hat{e}_i$ and $\hat{e}_s$ denote the unit vectors of the electric field for the incident and scattered photons, respectively. Equation 3.12 implies that both the propagation direction of the incident photons and the location of the detector greatly affect the observability of a particular Raman active mode. Most Raman experiments employ the back-scattering geometry, depicted in Figure 3.5. Incident and scattered photons travel along the same axis but in opposite directions, often denoted $z(xy)\bar{z}$, where z and $\bar{z}$ are the incident and scattered wave vectors and the electric field oscillates in the x-y plane.

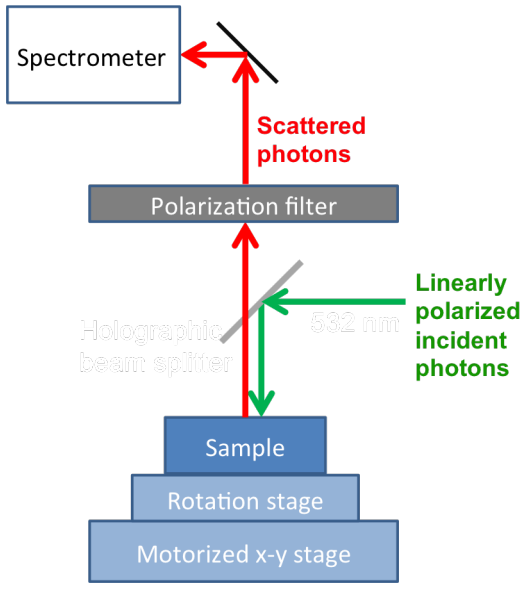

FIGURE 3.5. Raman backscattering geometry.

3.1.5. Group Theory in 2D van der Waals Materials. The Raman modes observable in a given crystal can be predicted based upon the point group to which the crystal belongs [108]. The point group is defined by the symmetry operations present in the crystal. It is now that we must make the distinction between crystals and molecules from a Raman perspective. Clearly, the number of atoms present in a crystal is innumerous and, thus, there must be some smaller repeating unit that can completely describe the structure. A unit cell is defined as the smallest repeatable volume that, when repeatable in all relevant directions, can completely reproduce the crystal lattice. Now, in order to determine the total number of vibration modes, one only needs to consider 3N, where N is the number of atoms in the unit cell. Another distinction from molecules is that rotations no longer exist but translations in the x, y, and z directions now correspond to acoustic modes, which are zero- or low-frequency phonon modes. The remaining 3N-3 phonon modes are optical phonons.

The crystals studied in this dissertation only include a few point groups, which are defined in Table 3.1. For each of these point groups, there exist character tables that list the expected Raman modes. Along with the character tables, Raman tensors can also be found for each of the Raman-active modes for a given point group. The values for each element in the Raman tensor are usually calculated using density functional theory (DFT) but they can also be determined experimentally; however, this can be quite difficult as the absolute intensities are affected by the experimental setup, electron-phonon coupling, and other factors, both intrinsic and extrinsic. As a result, the analysis of Raman spectra is often undertaken through relative comparisons and from a purely phenomenological perspective.

3.2. Absorption and Photoluminescence Spectroscopy

3.2.1. Introduction. Another useful technique for studying the properties of 2D semiconductors is photoluminescence spectroscopy. There are many texts which describe optical processes in semiconductors, including, Klingshirn, Pankove, Kittel, Perkowitz, and many others [51, 90, 49, 92]. In general, absorption and photoluminescence, two closely-coupled

Point Group	Raman-active Modes	Example Materials
D_{6h}	A_{1g}, E_{1g}, E_{2g}	bulk (MoS_2, α-$MoTe_2$)
D_{3h}	$A_1^{'}$, E', E"	odd-numbered layers (MoS_2, α-$MoTe_2$)
D_{3d}	A_{1g}, E_g	even-numbered layers (MoS_2, α-$MoTe_2$)
C_i	A_g	ReS_2
C_{2v}	A_1, A_2, B_1, B_2	WTe_2 and $Mo_{1-x}W_xTe_2$ alloys (semi-metallic)
C_{2h}	A_g, B_g	β-$MoTe_2$

TABLE 3.1. Point groups and symmetry operations of crystals considered in this work.

phenomena in semiconductors, are complex and, therefore, the reader is directed towards the aforementioned texts for a more thorough treatment. This section will, however, delve into some of the basics of absorption and photoluminescence in semiconductors and discuss more specific examples as applied to 2D semiconductors.

3.2.2. Maxwell's Relations. In order to develop an understanding of light-matter interactions in semiconductors, it is important to address the basic phenomena of an electromagnetic wave travelling through a medium starting with Maxwell's equations:

$$\begin{aligned} \vec{\nabla} \times \vec{H} &= \vec{j} + \frac{\partial \vec{D}}{\partial t} \\ \vec{\nabla} \times \vec{E} &= -\frac{\partial \vec{B}}{\partial t} \\ \vec{\nabla} \cdot \vec{D} &= \rho \\ \vec{\nabla} \cdot \vec{B} &= 0 \end{aligned} \tag{3.13}$$

, where $\vec{H}$, $\vec{E}$, $\vec{B}$, $\vec{D}$, $\vec{j}$, and ρ denote the magnetic field, electric field, magnetic induction, displacement, current density, and free carrier charge density, respectively. We begin by first solving the case of a propagating electromagnetic wave in vacuum. In order to solve Maxwell's equations in this case, we need the following constitutive relations between $\vec{E}$ and $\vec{D}$ and $\vec{H}$ and $\vec{B}$:

$$\overrightarrow{D} = \epsilon_0 \overrightarrow{E} \tag{3.14}$$

$$\overrightarrow{B} = \mu_0 \overrightarrow{H} \tag{3.15}$$

, where ϵ_0 and μ_0 are the permittivity and permeability of free space, respectively. In a vacuum medium, we have excluded both polarization and magnetization. Additionally, $\overrightarrow{j} = 0$ and $\rho = 0$. The solutions to Maxwell's equations yield the wave equations in both magnetic and electric field:

$$\overrightarrow{\nabla}^2 \overrightarrow{E} = \epsilon_0 \mu_0 \frac{\partial^2 \overrightarrow{E}}{\partial t^2} \tag{3.16}$$

$$\overrightarrow{\nabla}^2 \overrightarrow{B} = \epsilon_0 \mu_0 \frac{\partial^2 \overrightarrow{B}}{\partial t^2} \tag{3.17}$$

. For the experiments in this dissertation, the interactions of light and matter in the presence of a magnetic field were not measured and, thus, the magnetic effects are ignored in the following discussions.

In the case of electromagnetic waves incident upon a semiconductor, there are both bound and free charges that will affect the solutions to Maxwell's equations. We first consider the contribution of bound charges, which include the atomic cores and bound electrons. The polarization induced in these bound charges is given by:

$$\overrightarrow{P} = \chi \epsilon_0 \overrightarrow{E} \tag{3.18}$$

, where χ is the susceptibility of the material. This is, of course, a linear approximation; there are higher ordered terms but, for now, they can be ignored as we consider the low E-field limit. The displacement now includes a polarization term, $\overrightarrow{P}$, and can then be written

as:

$$\overrightarrow{D} = \epsilon_0 \overrightarrow{E} + \overrightarrow{P} = \epsilon_0(1+\chi)\overrightarrow{E} = \epsilon_{lattice}(\omega)\epsilon_0 \overrightarrow{E} \tag{3.19}$$

, where the term in parentheses represents the dielectric response function that we rename $\epsilon_{lattice}(\omega)$ to emphasize that it originates from bound charges in the lattice and is, in general, frequency-dependent. Another useful quantity is the conductivity $\sigma(\omega)$, which is related to aforementioned quantities by the following equation:

$$\overrightarrow{j} = \sigma(\omega)\overrightarrow{E} \tag{3.20}$$

. Conductivity, usually described by a tensor, is frequency-dependent, complex, and can contain nonlinear and spatially non-local relationships. Using equations 3.19 and 3.20 to solve Maxwell's equations and eliminating $\overrightarrow{B}$ yields the folllowing equation:

$$\overrightarrow{\nabla} \times \overrightarrow{\nabla} \times \overrightarrow{E} = \overrightarrow{\nabla}^2 \overrightarrow{E} - \overrightarrow{\nabla}(\overrightarrow{\nabla} \cdot \overrightarrow{E}) = \epsilon_{lattice}\epsilon_0\mu_0 \frac{\partial^2 \overrightarrow{E}}{\partial t^2} + \sigma\mu_0 \frac{\partial \overrightarrow{E}}{\partial t} \tag{3.21}$$

. If we consider an electromagnetic wave propagating with wavevector $\overrightarrow{q}$ and frequency ω given by:

$$\overrightarrow{E} = \overrightarrow{E_0} e^{i(\overrightarrow{q}\cdot\overrightarrow{z} - \omega t)} \tag{3.22}$$

, then equation 3.21 becomes:

$$q^2 \overrightarrow{E} - \overrightarrow{q}(\overrightarrow{q} \cdot \overrightarrow{E}) = \epsilon_{lattice}\epsilon_0\mu_0\omega^2 \overrightarrow{E} + \sigma\mu_0 i\omega \overrightarrow{E} = \omega^2 \epsilon(\omega)\epsilon_0\mu_0 \overrightarrow{E} \tag{3.23}$$

, where $\epsilon(\omega)$ is the total dielectric function and can be rewritten as:

$$\epsilon(\omega) = \epsilon_{lattice}(\omega) + i\frac{\sigma(\omega)}{\epsilon_0\omega} = \epsilon_1 + i\epsilon_2 \tag{3.24}$$

. This dielectric function describes the interaction of semiconductors with electromagnetic waves in the linear response limit. Another quantity commonly used in optics is the complex

index of refraction $\widetilde{n}$, which is given by:

$$\tilde{n} = n + ik \tag{3.25}$$

, where n is the real part of the index of refraction and describes the speed of light in a medium relative to its speed in vacuum. The quantity k is the extinction coefficient and is related to absorption through equation 3.26:

$$\alpha = \frac{2\omega k}{c} \tag{3.26}$$

. Equations 3.24 and 3.26 are related by:

$$\tilde{n} = \sqrt{\epsilon(\omega)} \tag{3.27}$$

.

3.2.3. Optical Processes in Semiconductors. The preceding description of electromagnetic waves propagating through a semiconductor was built entirely upon classical theory of electromagnetism. It was useful in deriving relations between how light and matter interact and for demonstrating that these light-matter interactions are, in general, frequency dependent. However, classical theory is incapable of describing *how* or *why* the interactions depend upon frequency. In order to describe how the interactions of light with semiconductors depend upon the frequency (or energy), quantum and solid-state physics are required. Griffiths, Ashcroft and Mermin, and Kittel are all excellent texts on this subject matter.

Electrons, or charge carriers, in general, do not behave the same in a crystal as they do in free space. This is a consequence of the fact that they will experience a periodic potential imposed by the crystal lattice (atomic cores) itself. Charge carriers will propagate as electromagnetic waves (Bloch waves) with wavevectors allowed for by the constraints of the crystal lattice. The dispersion relations (energy vs. wavevector) of these charge carriers are described and represented as multiple sets of continuous bands and can be

plotted in band diagrams. An example semiconductor band diagram is shown in Figure 3.6. When these charge carriers progagate through the crystal lattice, some of the waves will experience destructive interference from Bragg reflections, leaving forbidden energies at certain wavevectors [92]. These forbidden energies give rise to an energy gap, the hallmark of a semiconductor or insulator, depending upon the size of the energy gap. The valence band represents the highest range of energies (excluding defects or doping in the crystal) an electron would possess at absolute zero temperature, whereas the conduction band represents the lowest range of unoccupied states. The energy gap is defined as the difference in energy between the valence and conduction band edges.

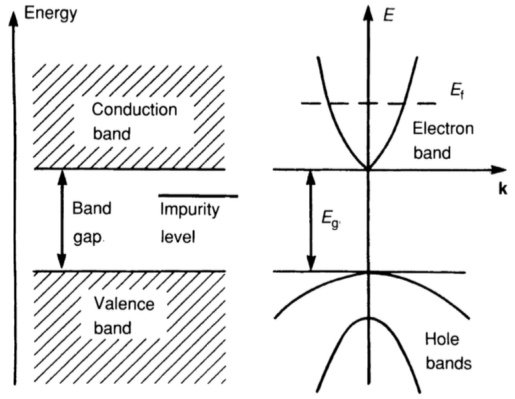

FIGURE 3.6. Energy band diagram of a direct gap semiconductor. Reproduced from [92].

Two important characteristics of a semiconductor is the size of this gap and whether or not the conduction band minimum (CBM) and valence band maximum (VBM) occur at the same wavevector. If the CBM and VBM occur at the same wavevector, the material is classified as a direct bandgap; if not, it is an indirect one. In the simplest picture, the size of the energy gap (direct or indirect) will determine the energies of photons the material will absorb; semiconductors absorb photons with energies equal to or greater than the bandgap. The subsequent emission of a photon (photoluminescence) will occur at the minimum allowable transition energy. The efficiency at which absorption and emission occur partly depends upon the bandgap type; direct bandgap semiconductors are efficient absorbers and emitters while

indirect bandgap semiconductors are, generally, less efficient. Other factors that affect the efficiency at which these optical processes occur include intrinsic (binding energies, density of states at the band edges, etc.) and extrinsic (defect density, defect type, temperature) properties inherent to the crystal, thus making photoluminescence a powerful spectroscopic tool. One of the reasons materials research on 2D van der Waals semiconductors has become so prevalent in the past several years was the discovery that Group VI TMDCs exhibit a modulation in the bandgap size and type (direct vs. indirect) as a function of the number of layers [79].

3.2.4. Absorption and Photoluminescence Measurements in 2D Materials. The first absorption measurements performed on layered materials in the mono- and few-layer limit were performed on graphene, a zero bandgap semiconductor, by Mak *et al.* in 2008 [78]. In that work, the absorption was measured using reflection contrast measurements that involve measuring the differential reflection between the substrate and the sample (graphene) supported on the substrate (left graph in Figure 3.7). Reflection contrast, denoted $\frac{\triangle R}{R}$, can be related to the absorbance of the thin film through equation 3.28:

$$Absorbance = \frac{(n_s^2 - 1)}{4} \frac{\triangle R}{R} \tag{3.28}$$

(right graph in Figure 3.7), where n_s is the index of refraction of the substrate. The caveat to this measurement is that it can only be accurate in samples where the thickness $d \ll \lambda$, which is the case for mono- and few-layered 2D materials.

Figure 3.8 is an example spectra of MoS2 obtained by mechanical exfoliation of naturally-occuring bulk crystals, as well as samples grown by chemical vapor deposition as part of this dissertation. Figure is an example photoluminescence (PL) spectra from the CVD-grown MoS2. It can be clearly seen that the PL spectra has much more narrow features. This is due to the fact that photoluminescence will occur at a very well-defined energy (the lowest energy transition), with hot photoluminescence being a minor caveat; whereas

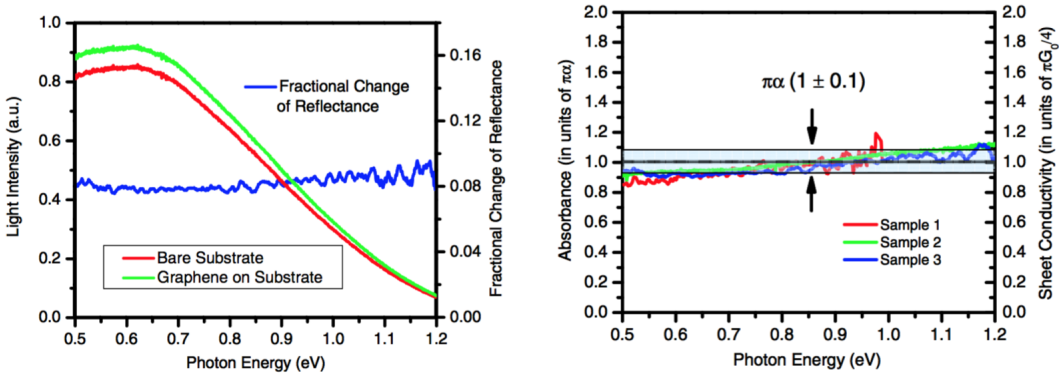

FIGURE 3.7. Graphene absorption spectrum measured by reflection contrast supported on a fused silica substrate. Reproduced from [78].

absorption will possess broader features over all energies larger than the bandgap. This makes photoluminescence spectroscopy a more powerful tool for analyzing small shifts in the electronic properties as a function of extrinsic factors (strain, defects, etc.), especially in direct-gap materials. The power of this technique will be demonstrated in Chapters 4 and 5.

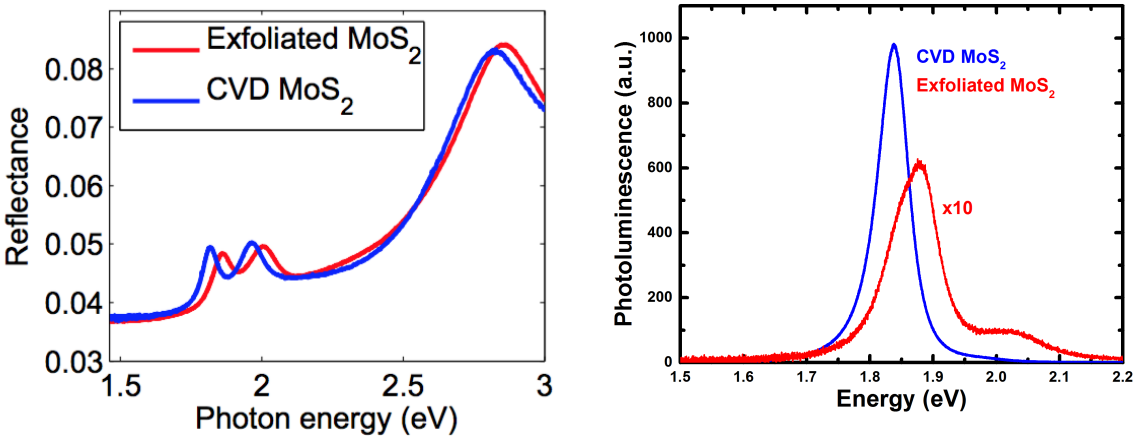

FIGURE 3.8. Reflectance (left) and photoluminescence (right) of monolayer MoS_2. CVD MoS_2 reflectance and photoluminescence peaks are red-shifted as compared to exfoliated crystals. The photoluminescence in CVD MoS_2 is notably more than 10 times brighter than in exfoliated samples. (Left) reproduced from [70].

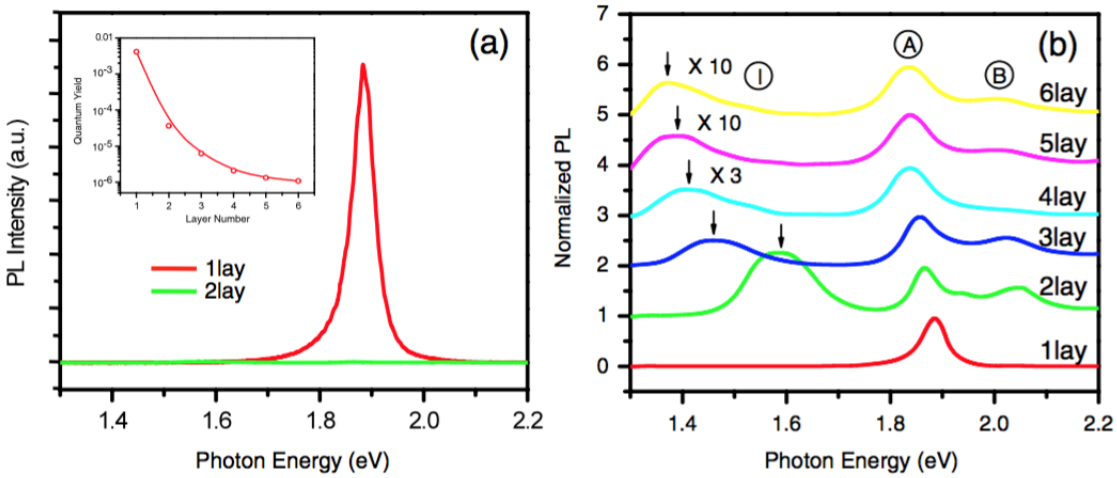

FIGURE 3.9. Evolution of the PL spectra in mono- to few-layer MoS_2. a) PL spectra of monolayer and bilayer MoS_2. A strong spectral peak is observed at ~1.87 eV in the monolayer, consistent with the evoltion of a direct optical gap. b) The PL spectra of 1 through 6 layers of MoS_2. The indirect gap blue shifts from ~ 1.4 eV in the 6-layer to 1.6 eV in the bilayer and disappears in the monolayer. Reproduced from [79].

3.2.5. Background on PL in Group VI TMDCs. The emergence of Group VI TMDCs to the forefront of 2D material research, following graphene, can be traced back to the seminal work by Mak *et al.* where they demonstrated an evolution of the optical bandgap in MoS_2 using photoluminescence spectroscopy shown in Figure 3.9 [79]. This similar phenomena has since been demonstrated in the other semiconducting Group VI TMDCs, $MoSe_2$, $MoTe_2$, WS_2, and WSe_2. DFT calculations, as well as angle-resolved photoemission spectroscopy (ARPES), have shown this phenomena to be attributed to reduced interlayer interactions that shift the band edges at the Γ point in the valence band [44], as well as another intermediate point between the Γ and K points in the conduction band [104]. This is shown in Figure 3.10. The result is a direct bandgap located at a point, K, at the corner of the Brillouin Zone (primitive unit cell in reciprocal lattice).

3.2.6. Effects of Doping and Strain on the PL Spectra of Monolayer MoS_2. An important clarification to the above description of the band structure of MoS_2 is that we are talking about the optical gap. The distinction must be made because, in these layered

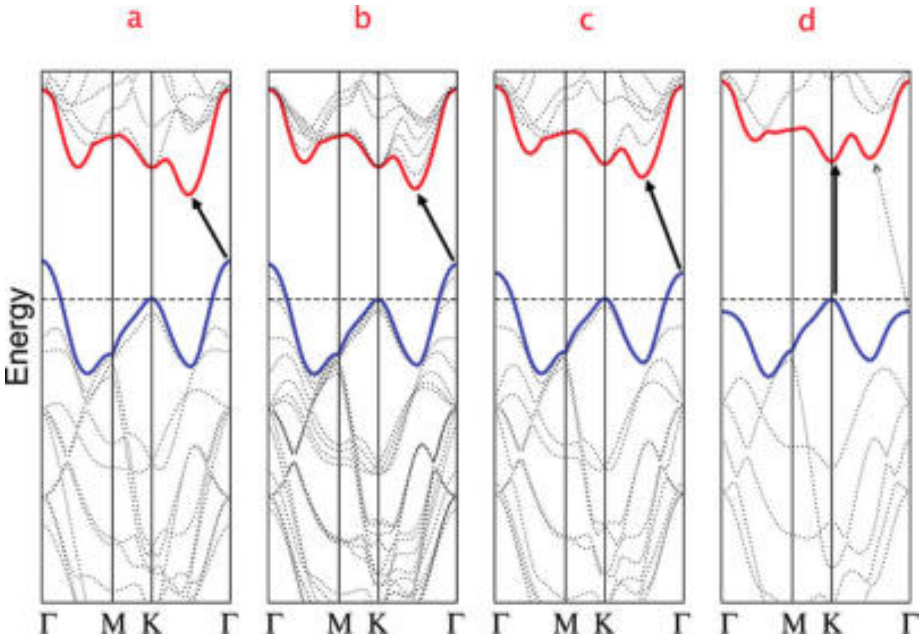

FIGURE 3.10. Evolution of band structure in (a) bulk, (b) trilayer, (c) bilayer, and (d) monolayer MoS_2. The transition is due to reduced interlayer interactions, which allows the valence band edge at the Γ point to drop below the edge at the K point. A shift is also observed at an intermediate point between the Γ and K points. Reproduced from [104].

TMDCs, there are pronounced coulombic interactions that modify the observed optical and electronic properties. Specifically, these materials exhibit strong excitonic effects. Due to the reduced dielectric screening present in two dimensional materials, optically excited electrons form strongly-bound quasiparticles, called excitons, with the holes they leave behind. In conventional semiconductors, such as silicon or germanium, exciton binding energies are on the order of a few meV; whereas, in monolayer TMDCs, exciton binding energies are on the order of 500 meV. Highly-doped monolayers also form another quasiparticle, known as a trion, which can either consist of 2 electrons and 1 hole (negatively-charged) or 2 holes and 1 electron (positively-charged). These trions typically have binding energies on the order of 25-30 meV. These binding energies can be strongly affected by the dielectric environment (substrate effects) and the doping of the sample [82].

The initial characterization of the effects of charge doping on the optical properties of

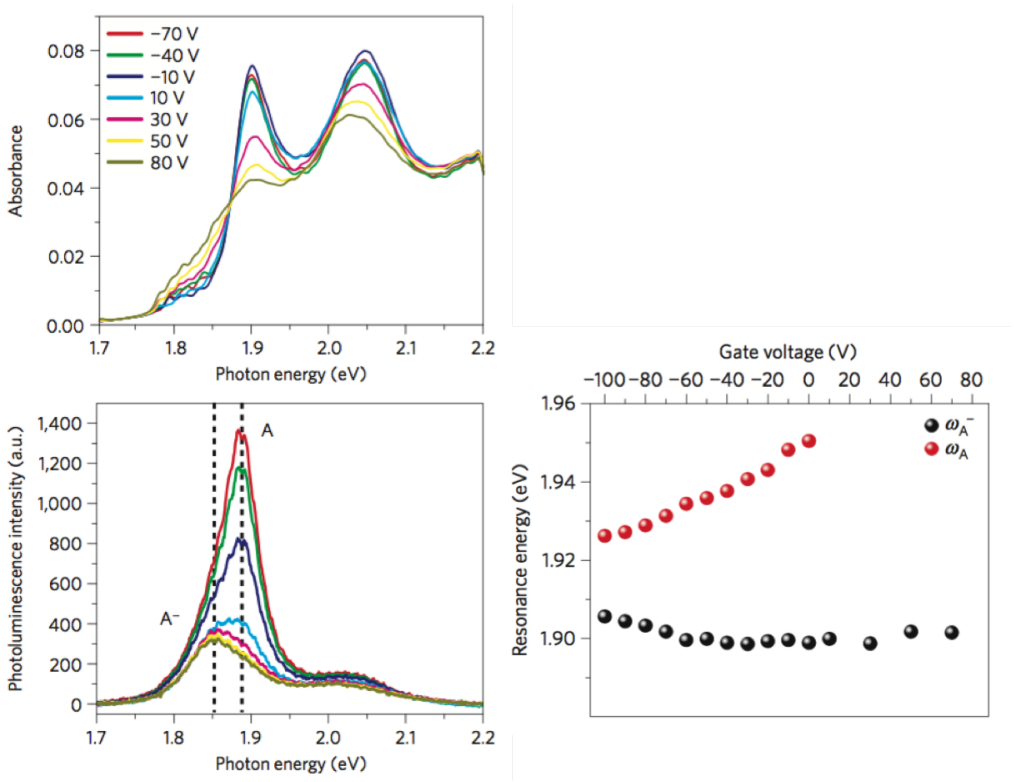

FIGURE 3.11. Trions in MoS_2. (top left) The absorption spectra as a function of gate voltage. (bottom left) PL spectra as a function of gate voltage. (bottom right) Energy of the negatively-charged trion (ω_A^-) and neutral exciton (ω_A) as a function of gate voltage. Reproduced from [82].

monolayer MoS_2 was reported by Mak *et al.* Using a gate voltage to modulate the electron density in the sample, the absorption and PL spectras were taken. Figure 3.11 (top left) and (bottom left) shows that the intensity of the A peak (neutral exciton) can be strongly tuned with the gate voltage. With a high positive gate voltage, the sample becomes highly electron doped and the neutral exciton is effectively quenched in both the absorption and the emission. With high negative gate voltage, the sample approaches intrinsic doping levels and the neutral exciton becomes stronger in both absorption and emission. Figure 3.11 (right) shows the resonance energy for the exciton and trion as a function of gate voltage. The neutral exciton shifts by more than 20 meV throughout the range, underscoring the effect of doping on the measured spectra [82].

Another extrinsic factor that affects the photoluminescence in monolayer MoS_2 is strain. Conley *et al.* explored this phenomena by transferring a crystal to a thin flexible substrate and measuring the photoluminescence as a function of curvature of the substrate, which they used to calculate the applied strain [14]. They observed shifts in the A exciton luminescence energy of approximately 50 meV at a strain of 1%. They also observed a decrease in the PL intensity with increased strain, which they attributed to an evolution of the bandstructure from a direct to indirect gap. This, as well as the aforementioned effects of doping and binding energies, underscores the complexity as well as the importance of discerning the origin of PL shifts.

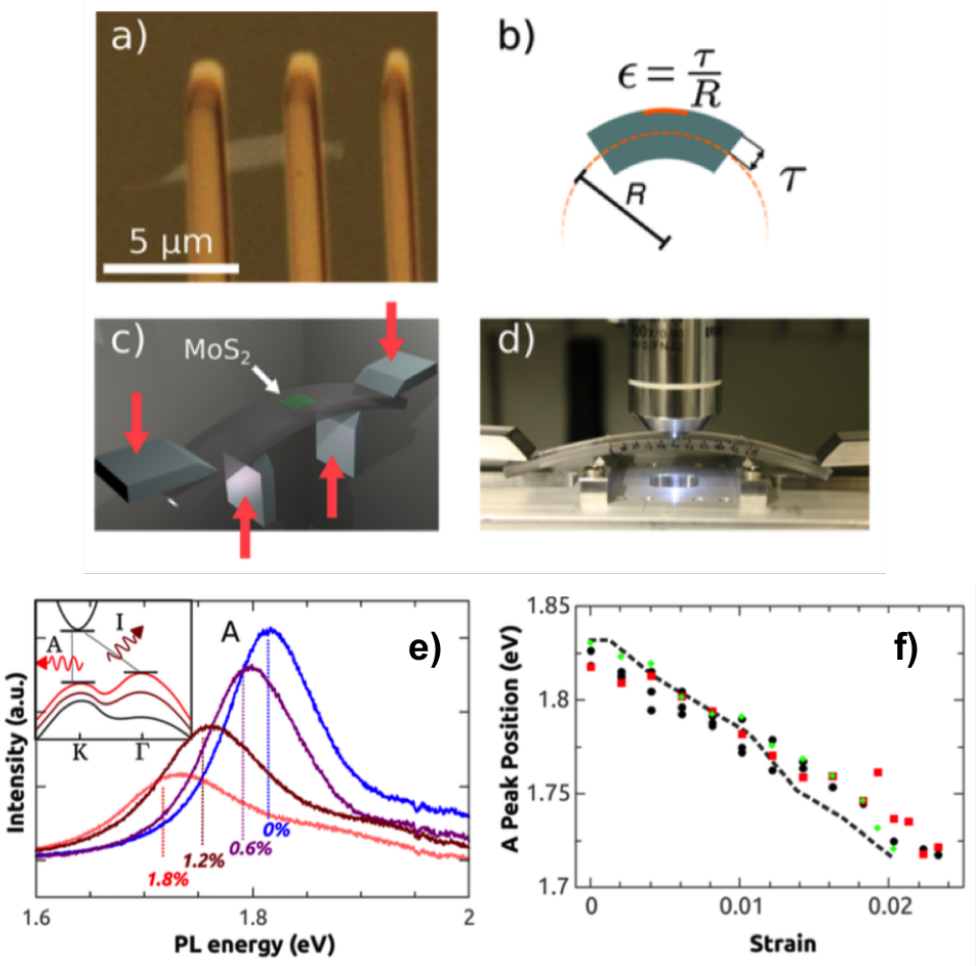

FIGURE 3.12. PL as a function of strain. (a-d) Device and four-point bending apparatus for applying strain on monolayer MoS_2. (e,f) Modulation of bandgap energy as a function of applied strain. Reproduced from [14]

CHAPTER 4

Molybdenum Disulfide Synthesis and Characterization

This chapter was adapted with permission from our paper: A. M. van der Zande, P. Y. Huang, D. A. Chenet et al., "Grains and Grain Boundaries in Highly Crystalline Monolayer Molybdenum Disulphide", Nature Materials, 12, 554-561 (2013).

4.1. Background

Molybdenum Disulfide (MoS_2) is an n-type layered semiconductor with an indirect band gap of 1.4 eV in the bulk that evolves into a direct band gap of 1.9 eV in the monolayer limit. Over the past several years, it has generated significant interest in the emerging fields of nanoelectronics, flexible electronics, and valley- and optoelectronics. Due to its abundance in nature and the ease with which laboratory samples could be obtained by mechanical exfoliation techniques, it has served as the prototypical material in the family of layered materials beyond graphene. Requisite to the pursuit and evaluation of MoS_2, as well as other layered materials, for technological applications is the development of synthesis and fabrication techniques that enable scalability. Furthermore, a thorough understanding of the performance limits as well as the role of defects requires a myriad of complementary characterization techniques that relate structure to property to function. To these ends, large-scale monolayer MoS_2 was synthesized by chemical vapor deposition (CVD). The films were synthesized directly on thermally-grown SiO_2 substrates and were composed of single domains up to 150 μm in size that merged together to form millimeter-scale continuous polycrystalline sheets. Transmission electron microscopy, photoluminescence and Raman spectroscopy, and electrical transport measurements were used to characterize these films.

4.2. Crystals Grown by Chemical Vapor Deposition

Figure 4.1a,b shows optical images of monolayer MoS_2 grown on a Si/SiO_2 substrate. Figure 4.1a shows an optical image of a typical sample. Isolated islands (violet triangles) have edge lengths ranging from 30 to 80 µm. On the right (nearest to the solid-state precursors during growth), the islands merge into a continuous film. Although non-uniformity in nucleation density and crystal size is a limitation of this growth technique, each growth contains a $\sim$1×15 mm region where hundreds of similar, isolated islands grow. Across different growths, the average size of islands varies between 20 and 100 µm, with individual triangles up to 150 µm (Supplementary Fig. S2). Most islands are uniform monolayers, except for small bilayer or multilayer patches (visible in the center of Fig. 4.1b).

Photoluminescence spectroscopy can be used to infer the quality and thickness of these triangles. Figure 4.1c shows photoluminescence spectra from monolayer and bilayer MoS_2. The photoluminescence peaks at 1.84 and 1.95 eV respectively match the A and B direct-gap optical transitions16. The integrated intensity of the bilayer peak is much weaker ($\sim$7%) than the monolayer peak, reflecting the expected evolution from an indirect-gap to a direct-gap semiconductor. Surprisingly, the measured range of peak widths of our CVD monolayer MoS_2 (50–60 meV) is similar to that observed for freely suspended samples of exfoliated MoS_2 (also 50–60 meV) and is much narrower than that of MoS_2 exfoliated onto SiO_2 (100–150 meV; [79]). These results suggest that the CVD-grown samples are either of higher quality or are in a cleaner electrostatic environment than exfoliated samples.

4.3. Transmission Electron Microscopy Imaging

To characterize the crystal structure of these islands, a combination of TEM, electron diffraction techniques and atomic resolution STEM were used. Figure 4.1d shows an image of the atomic structure of CVD MoS_2 monolayers taken by aberration-corrected annular dark-field scanning transmission electron microscopy (ADF-STEM). In ADF-STEM, a 60 keV,

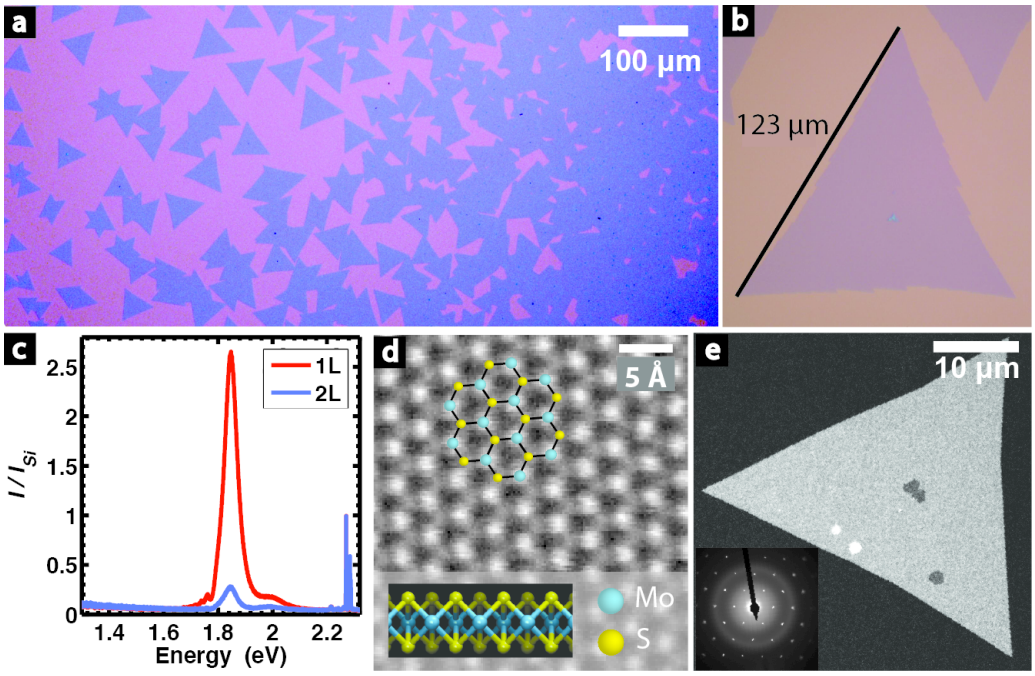

FIGURE 4.1. Large-grain MoS_2 growth. a, Optical reflection image of a CVD growth of a typical large-grain MoS_2 on a SiO_2 (285 nm)/Si substrate. The image contrast has been increased for visibility; magenta is the bare substrate, and violet represents monolayer MoS_2. b, Optical image of a monolayer MoS_2 triangle. The triangle is 123 µm from tip to tip. c, Photoluminescence spectra from monolayer (red) and bilayer (blue) MoS_2. Peak height is normalized to the silicon Raman peak. The narrow spikes at high energy are the Raman transitions. d, High-resolution ADF-STEM image of freely suspended monolayer MoS_2 on a TEM grid. The bright spots are molybdenum atoms; the grey spots are two stacked sulfur atoms. The lattice is composed of hexagonal rings alternating molybdenum and sulfur sites; top view and side views of the structure are overlaid. e, DF-TEM image of a large triangle with the diffraction pattern inset. Together, the diffraction pattern and the DF-TEM image show that the triangle is a continuous single crystal. The ∼2–4 µm brighter and darker areas are rotationally aligned bilayers of MoS_2. Similar variations in contrast have been observed in bilayer graphene, where they reflect differences in stacking order [8]. Reproduced from [112].

ångstrom-scale electron beam scans over the sample, and an image is formed by collecting the medium- to high-angle scattered electrons. The contrast of ADF-STEM images scales roughly as the square of the atomic number Z [54]. Thus, the brightest spots in Fig. 4.1d are the molybdenum atoms and the dimmer spots are the two stacked sulfur atoms. The

hexagonal lattice is clearly visible, as indicated by the top- and side-view schematics in Fig. 4.1d. No point defects, atomic substitutions or voids were initially observed within single crystals.

Selected-area electron diffraction and dark-field TEM (DF-TEM) were used to characterize the large-scale crystal structure of the islands. Figure 4.1e, inset shows a selected-area electron diffraction pattern of a triangular island roughly 45 µm across. The six-fold symmetry in the position of the diffraction spots demonstrates that the triangle contains no rotational boundaries, to within a measurement accuracy of 0.5 degrees. Figure 4.1e shows the corresponding DF-TEM image: by using an aperture to select a narrow range of diffracted beams, DF-TEM filters images by crystallographic orientation [41, 42, 8, 33], and shows single crystals such as Fig. 4.1e in a single image. Similar analyses of dozens of triangles show that triangular-shaped islands are predominantly single crystals. Under continued growth, these islands merge together to form aggregates or continuous sheets (Fig. 4.1a).

The large-grain, highly crystalline MoS_2 monolayers, with optical properties equivalent or superior to exfoliated samples, enable new experiments studying the growth, structure and properties of MoS_2 crystals and grain boundaries. Electron diffraction techniques are used to uniquely identify the crystal structure and edge orientation of MoS_2 triangles. Figure 4.2a,b shows the bright-field image and diffraction pattern of a single-crystal triangle. As seen in the schematic in Fig. 4.2a, the lattice of monolayer MoS_2 is divided into molybdenum and sulfur sublattices, which reduces the hexagonal lattice from six-fold to three-fold symmetry. As a result, the six $[\bar{1}100]$ diffraction spots are broken into two families: ka = $\{(\bar{1}100)$, $(10\bar{1}0)$, $(0\bar{1}10)\}$ and $\overrightarrow{k_b} = -\overrightarrow{k_a}$ (Fig. 4.2b; [7]). Experimentally, the ka spots are higher in intensity ($\sim$10% for an 80 kV electron beam) and point towards the molybdenum sublattice, as indicated by the arrows in Fig. 4.2a,b.

The aforementioned intensity asymmetry is also observed in DF-TEM. Figure 4.2d shows the bright-field image and diffraction pattern of two triangles. An aperture positioned at the magenta circle on the inset in Fig. 4.2d forms the dark-field image in Fig. 4.2e. As the

triangles are rotated 180◦ from one another, the aperture simultaneously collects the bright ka spot for the right triangle and the darker kb spot for the left triangle. This produces a corresponding contrast difference between the islands. Thus, the diffraction pattern or DF-TEM can be used to uniquely identify the lattice orientation of MoS_2 crystals.

Figure 4.2 also shows the dominant morphologies of MoS_2 triangles: molybdenum zigzag (Mo-z-z) in Fig. 4.2a and sulphur zigzag (S-z-z) in Fig. 4.2d [10, 57]. These two edge orientations are commonly observed in MoS_2 nanocrystals [57], and they are the two most energetically stable edge orientations [10]. It is consistently observed that Mo-z-z triangles have sharper, straighter edges than S-z-z triangles. This morphological difference allows easy identification of the crystal orientation in optical images.

In addition to single-crystal triangles, the CVD process produces polycrystalline aggregates that can be characterized by DF-TEM. Figure 4.3a shows two S-z-z triangles intersecting at an angle of $40^{\circ} \pm 0.5^{\circ}$. Figure 4.3b shows a corresponding composite DF-TEM image of the crystal structure. The composite image is constructed by overlaying color-coded DF-TEM images [41] acquired from the crystallographic orientations shown in the diffraction pattern of Fig. 4.3a. The intersection of the grains forms an abrupt, faceted tilt boundary. Low-quality growths can produce the types of film in Fig. 4.3c, which shows small, misshapen, crystals. The corresponding diffraction pattern and dark-field overlay in Fig. 3d shows that the disordered crystals are randomly oriented polycrystalline aggregates. As indicated by the arrows in Fig. 4.3c, adjacent MoS_2 grains sometimes overlap to form rotationally misaligned bilayer regions. Similar combinations of abrupt and overlapped crystal interfaces have been seen in CVD-grown graphene [41, 111, 96]. Unlike in graphene, the grain boundaries in MoS_2 tend to be strongly faceted on the micrometer scale. These facets may originate from the relative surface energy of different edge configurations [38], which will be more directionally dependent in MoS_2 than in homoelemental structures. Similar phenomena probably underlie the differences in edge roughness seen in Mo-z-z versus S-z-z triangles and the faceting at the edges of large crystals such as in Fig. 4.1b.

In addition to tilt boundaries, mirror twin boundaries are commonly observed in this synthesis process. In monolayer MoS_2, mirror twins are the intersections of two MoS_2 crystals with a relative in-plane rotation of 180^o that effectively swaps the positions of Mo and S lattice sites. Figure 3e shows the bright-field image of two triangles meeting at 180^o, and Fig. 4.3f shows the corresponding DF-TEM image. The mirror twin appears clearly as an intensity change in DF-TEM images, through the same diffraction asymmetry seen in Fig. 4.2e. Unlike tilt boundaries, mirror twin boundaries such as in Fig. 4.3e,f grow within nucleation islands. Figure 4.3g,h shows another commonly observed shape that contains mirror twin boundaries: a symmetric, six-pointed star containing cyclic twins that resemble other inorganic and geological crystal growths [129].

ADF-STEM can also be used to examine the structure of the 1D grain boundaries in polycrystalline samples. Figure 4.4a,b show a mirror twin boundary in a 6-pointed star. Whereas the grain boundary follows the zig-zag direction on the micrometer scale, it exhibits faceting of $\pm 20^o$ relative to this direction on the nanometer scale. This nanoscale faceting is surprising because it avoids the highly symmetric zigzag boundary structure that would correspond to the microscale alignment seen in Fig. 4.3h. Figure 4.4b shows the atomic structure of the grain boundary. The overlaid purple and green polygons show that the boundary is formed primarily from 4- and 8-membered rings, with a recurring periodic 8-4-4 ring motif.

Using STEM, other reports have revealed that tilt boundaries are composed of 5-7 rings [87]. These results are consistent with theory calculations that predict that in MoS_2, either odd- or even-membered rings can form grain boundaries depending on the tilt angle and stoichiometry, among several factors [133]. For comparison, graphene's tilt boundaries are most commonly formed by 5- and 7-membered rings [41, 47], whereas twin boundaries have been observed with 8-5-5 motifs [55]. The data also suggest that a priori simulation of boundary structures may be challenging: for example, the 8-4-4 motif does not match the theoretically predicted structure in [133], mostly owing to its surprising faceted structure.

In the observed 8-4-4 motif, neighbouring 4-rings meet at a sulfur site, which appears to have four nearest neighbours rather than the usual three. This change in coordination requires either the S atoms to have dangling bonds, or the Mo atoms to change their oxidation state. Using first-principles density functional theory [29] (DFT), it was found that after relaxation, the 8-4-4 boundary structure is at a local energetic minimum (Fig. 4.4c).

Figure 4.4d shows the DFT-calculated density of states (DOS) of defect-free monolayer MoS_2 (black curve). The light green band indicates the bandgap of pristine MoS_2. When a grain boundary is implanted into the MoS_2, the DOS develops mid-gap states (pristine + GB, red dashed curve) that appear mainly in the projected DOS of the atoms in the boundary (GB alone, filled blue curve). Figure 4.4e shows a spatial plot of the local DOS of pristine + GB in the plane of the Mo atoms, integrated in the energy range of the pristine bandgap; the mid-gap states are spatially localized at the boundary. These localized mid-gap states, typical of defects in semiconductors, are important because they can affect the optical and transport properties of the material [55, 91].

4.4. Photoluminescence Spectroscopy

Using the understanding of the grain structure developed above, the systematic examination of the effects of individual grain boundaries on the optical and electronic properties of MoS_2 can be pursued. The optical emission properties of MoS_2 can be mapped using photoluminescence spectroscopy by stepping a focused excitation laser over the sample and acquiring a spectrum at each point. These measurements were performed in a Renishaw inVia microscope using a 532 nm excitation laser and 600 l/mm diffraction grating. Figure 4.5a,e shows optical images of a mirror twin island (Fig. 4.5a) and a tilt boundary island (Fig. 4.5e). Figure 4.5b–d,f–h shows corresponding maps of integrated photoluminescence intensity, peak position and peak width. Away from the boundaries, both islands show similar emission intensities, peak positions (1.84 eV) and peak widths (57 meV in the mirror sample and 60 meV in the tilt sample, reflecting typical sample-to-sample variation). At

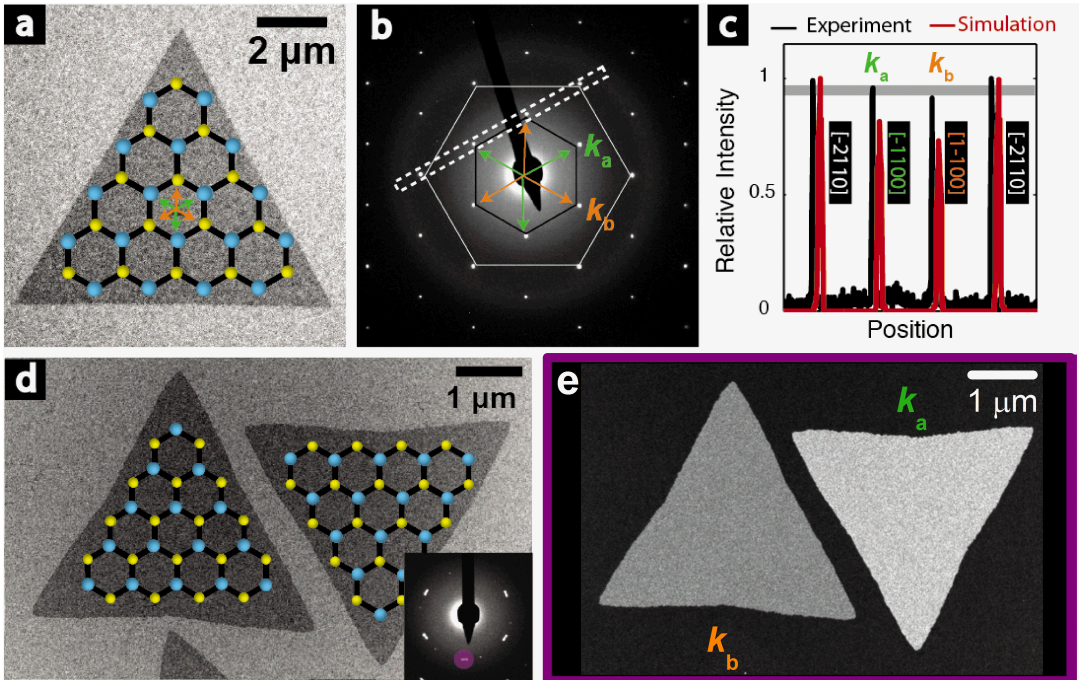

FIGURE 4.2. Diffraction imaging of crystal orientation and edge terminations. a, Bright-field image of a single-crystal triangle with a Mo-zigzag edge orientation. b, Diffraction pattern from a. The asymmetry of the Mo and S sublattices separates the [¯1100] diffraction spots into two families: ka = {(¯1100),(10¯10),(0¯110)} and kb = −ka. c, A line profile through experimentally measured diffraction spots (black) and Bloch-wave simulations (red). The higher intensity ka spots point towards the Mo sublattice, as indicated by the arrows in a,b. Both curves were normalized to the height of the [2110 ¯] peaks, and the red curve was offset horizontally for visibility. d, Bright-field TEM image of two triangles with S-zigzag edge orientations. The curved appearance of the crystal edges contrasts with the sharper crystal edges of the Mo-zigzag edges in a. The inset diffraction pattern shows the location of the aperture used to form the image in e. e, Dark-field image of the region in d. As the triangles are rotated 180◦ from one another, the aperture simultaneously collects the brighter ka spot for the right triangle and the darker kb spot for the left triangle. This produces a corresponding contrast difference between the two islands that allows us to uniquely infer crystallographic orientation from dark-field images. To improve visibility, the bottom of the intensity range has been clipped in this image. Reproduced from [112].

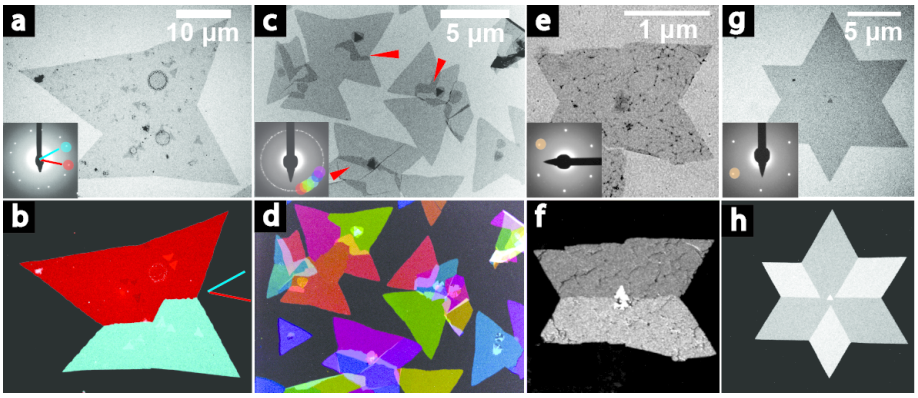

FIGURE 4.3. Tilt and mirror twin grain structures. a, Bright-field TEM image of two triangles that have grown together. Inset diffraction pattern shows the two crystal orientations are 40^{o} $\pm 0.5^{o}$ apart (measured between the red and cyan lines, which are at equivalent spots in the diffraction pattern). b, Color-coded overlay of DF-TEM images corresponding with the two red- and cyan-circled spots in a shows a tilt grain boundary as a faceted line connecting the two triangles. c, Bright-field image of a region containing irregularly shaped MoS_2 islands, with diffraction pattern inset. Red arrows indicate regions where adjacent grains overlap, forming rotationally misaligned bilayers. d, Colored DF-TEM overlay shows that the irregular shapes are polycrystalline aggregates. The crystals are connected both by faceted, abrupt grain boundaries, and $\sim$1 µm overlapped bilayers. e, Bright-field image of a mirror twin composed of 180^{o} -rotated triangles, with diffraction pattern inset. f, Dark-field image corresponding with the orange circle in e shows the two triangles have different diffraction intensity, similar to the 180^{o} -rotated triangles in Fig. 2d,e. This intensity change indicates the presence of a mirror twin boundary between the darker and lighter regions. The small triangle in the centre is multilayer MoS_2. g, Bright-field image of a 6-pointed star, with inset diffraction pattern. h, DF-TEM image corresponding with the orange circle in g shows that the star contains several rotationally symmetric mirror twins, forming a cyclic twin. Reproduced from [112].

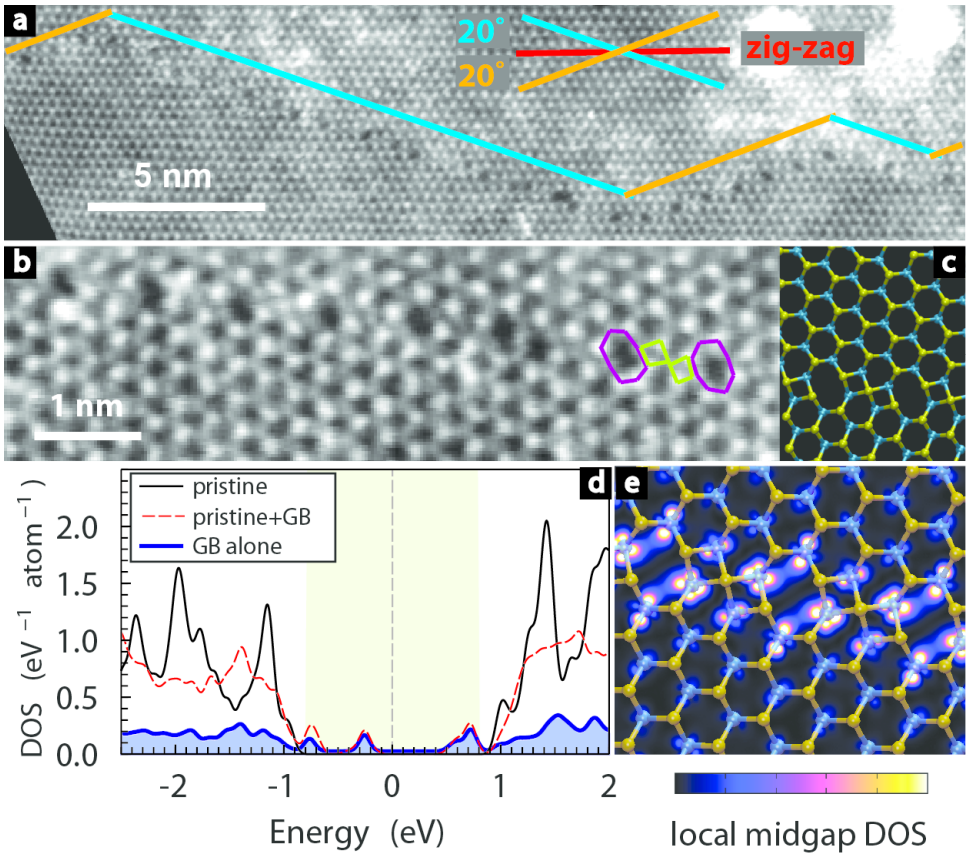

FIGURE 4.4. Grain boundary atomic structure. a, High-resolution ADF-STEM image of a mirror twin boundary. The boundary is visible just below the annotated line. The annotation indicates the nanoscale faceting of the boundary at $\pm 20^{o}$ off of the zigzag direction. b, Zoomed-in image of the grain boundary shows a periodic line of 8-4-4 ring defects. c, An atomistic model of the experimental structure shown in b. Energy minimization with DFT confirms that this boundary is locally stable. d, The total DOS of pristine MoS_2 (black), the total DOS of MoS_2 with the grain boundary (red dashed) and the projected DOS of the atoms along the grain boundary (blue filled). The dashed grey line denotes the Fermi energy of pristine MoS2, and the light green shaded area indicates the pristine bandgap. All states have been given a Gaussian broadening of 0.07 eV. e, A 2D spatial plot of the local mid-gap DOS (integrated in the plane of the Mo over a 1.7 eV range about the Fermi energy of the pristine MoS_2). The colour scale of the density is 0–0.05 states per bohr^3. Reproduced from [112].

the grain boundaries, the islands show strong photoluminescence modifications: the mirror boundary is a clearly visible straight line with 50% quenching of intensity (Fig. 4.5b), an 8 meV upshift in peak energy (Fig. 4.5c) and a 5 meV peak-broadening (Fig. 4.5d). The tilt boundary, which has a faceted structure similar to Fig. 4.3b, shows a surprising 100% enhancement in emission strength, 26 meV upshift and 5 meV broadening. The width of the signal change around the tilt boundary is also larger than around mirror boundaries.

The data demonstrate that photoluminescence is strongly affected by the presence of grain boundaries and that these changes depend on the grain boundary angle. Several factors may contribute. In the simplest theory, photoluminescence quenching arises from defects in semiconductors, such as mid-gap states at the boundaries, which can act as centers for non-radiative recombination [90]. This would, however, be surprising because the midgap states are localized to the 1D boundary, which is much smaller than the excitation laser spot. Two further aspects of the grain boundaries probably play a role in modulating photoluminescence: doping and strain. First, local changes in doping may occur at grain boundaries. For example, the observed 8-4-4 defects in the mirror boundary are molybdenum rich, which would n-dope the boundary, whereas 5–7 defects observed at a tilt boundary are sulfur-rich [87], which would p-dope the boundary. Previous investigations have shown that photoluminescence is strongly affected by charge density, with increased/decreased electron density causing photoluminescence quenching/enhancement [82]. The influence of charge is thus consistent with the observed trends in the strength of the photoluminescence at these different types of boundary. Other sources of doping can include spatial differences in growth kinetics or the preferential attachment of adsorbates at boundaries. Second, strain around the boundaries may modify the bandgap [102] or alter electrostatic interactions with the growth substrate.

4.5. Electrical Transport Measurements

An important question for device applications is whether grain boundaries disrupt or modify electrical transport. Field-effect transistors (FETs) were fabricated from islands containing a single grain boundary (Fig. 4.6a and Fig. 4.6c, inset). The FET channels followed three different configurations: within a grain (pristine), across the grain boundary (perpendicular) and along the grain boundary (parallel). Figure 4.6a,b shows plots of conductance versus gate voltage (transfer curves) for four representative devices fabricated on mirror twin islands: two pristine devices (black and magenta), one parallel device (orange curve) and one perpendicular device (cyan curve).

4.5.1. Pristine Devices. It is important to first gauge the variability in device-to-device performance, which will be a convolution of crystal quality, fabrication process, and contact resistance. In devices from different growths, room-temperature, field-effect mobilities ranged from 1 to 8 cm^2V^{-1} s^{-1}, and typical on/off ratios ranged between 10^5 and 10^7. Multiple devices fabricated within each single crystal yielded mobilities that were identical to within the measurement error. Specifically, the pristine devices in 4.6a,b (black and magenta curves) show n-type behaviour with mobilities of 3–4 cm^2V^{-1} s^{-1}. These ranges of values are comparable to those reported for back-gated FETs fabricated with mechanically exfoliated MoS_2 on SiO_2 (refs [95, 5, 56, 94]; in the absence of high-K dielectrics) and equivalent to the best reported values for monolayer CVD MoS_2 [66, 128]. Mobilities are most probably limited by substrate effects and the local electrostatic environment[16, 125] in addition to MoS_2 optical phonons.

4.5.2. Twin Boundary Devices. In the mirror twin device shown in Fig. 4.6a,b, the perpendicular device (cyan curve) shows nearly identical performance to the pristine devices (magenta and black curves), indicating that the mirror twin boundary has little effect on channel conductivity. However, the electrical characteristics of the parallel devices differed measurably from the pristine devices. Although the transfer curves of the parallel device

in Fig. 4.6a,b (orange curves) are qualitatively similar to that of the pristine devices, they have a 25% larger on-state conductivity and 60% larger off-state conductivity. This change is only slightly larger than the device-to-device variation, but was consistent across four parallel devices measured on mirror twins (particularly in the off state). The data impose a rough upper limit for conductivity along the one-dimensional grain boundary of 1.5 μS-μm in the on-state (Fig. 5j at Vg = +70 V) and 120 pS-μm in the off state (Fig. 5j at Vg = −70 V). These values can be compared to overall sheet conductivity for pristine devices of 2.2 μS/square in the on state and 56 pS/square in the off state. This analysis indicates that the few-atom-wide twin boundaries, although still semiconducting, have similar conductivity of up to a 1-μm-wide strip of pristine material. This result is consistent with the mid-gap states predicted in the material. The full effect of mid-gap states, however, is probably limited by the disorder in the grain boundary, which will prevent a continuum of states.

4.5.3. Tilt Boundary Devices. In contrast to the measurements of the mirror twin, FET devices of tilt boundaries show a decrease in conductance in both the parallel and perpendicular configurations. On one tilt boundary, shown in 4.6c,d, the on-state boundary conductance of both parallel and perpendicular devices decreases by 30% compared with pristine crystals. However, measuring six angle devices yielded no consistent change in conductance, decreasing by 5–80% compared with pristine. This variability is unsurprising: in graphene, electrical measurements are highly dependent on the structure of the boundary [111]. It is expected that these variations are wider and more complex in semiconducting MoS_2, where the electronic structure of the boundary should depend on the tilt angle and atomic structure [133]. Significantly, in all mirror twin and tilt boundaries measured, the change in conductance from any single grain boundary is only slightly more than the device-to-device variation—an important conclusion for the applicability of MoS_2-based electronics.

4.6. Conclusion

Monolayers of large-area, highly crystalline MoS_2 were synthesized on insulating surfaces and the crystal edges, grain structure and grain boundaries were imaged with electron microscopy. The location of individual grain boundaries were identified on the surface and the optical and electrical properties were systematically compared and related back to electronic structure calculations. In particular, the repeatability of the mirror twin was used to correlate measurements of the structure, photoluminescence and electronic transport of a single grain boundary structure. In tilt boundaries, photoluminescence and electrical transport measurements vary markedly for different boundaries. Controlling grain boundaries will be essential for optimizing MoS_2 electronic and photovoltaic devices, where defects in large-area heterostructures can lead to interlayer leakage or unwanted exciton recombination. MoS_2 was just the first member of a large family of layered transition metal dichalcogenides to be synthesized as a monolayer [32]. The above techniques are crucial for exploring synthesis strategies to optimize the grain properties, and provide a template for studies of the microscopic and macroscopic impact of grain structure on other monolayer membranes. These results are thus a significant step forward in realizing the ultimate promise of atomic membranes in electronic, mechanical and energy-harvesting devices.

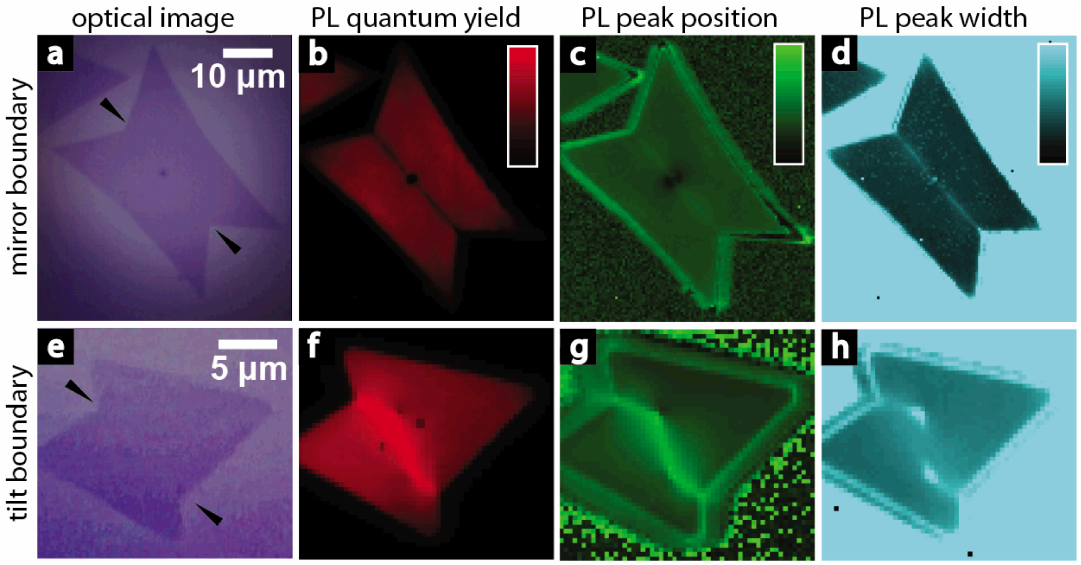

FIGURE 4.5. Optical properties of mirror and tilt boundaries. a–d, Optical measurements of an island containing a mirror twin boundary. e–h, Corresponding measurements for an island containing a tilt boundary. a,e are optical images; b–d and f–h are colour plots of photoluminescence. In b,f, red is the relative quantum yield, with colour scale 0–1100 a.u. We see 50% quenching at the mirror twin boundary and a 100% enhancement at the tilt boundary. In c,g, green is the peak position, with colour scale 1.82–1.87 eV. There is an upshift of 8 meV at the mirror twin boundary, and a much stronger 26 meV upshift in the tilt boundary. In d,h, cyan is the peak width with colour scale of 53–65 meV. The peak broadens from 55 to 62 meV at the boundary in both samples. Reproduced from [112].

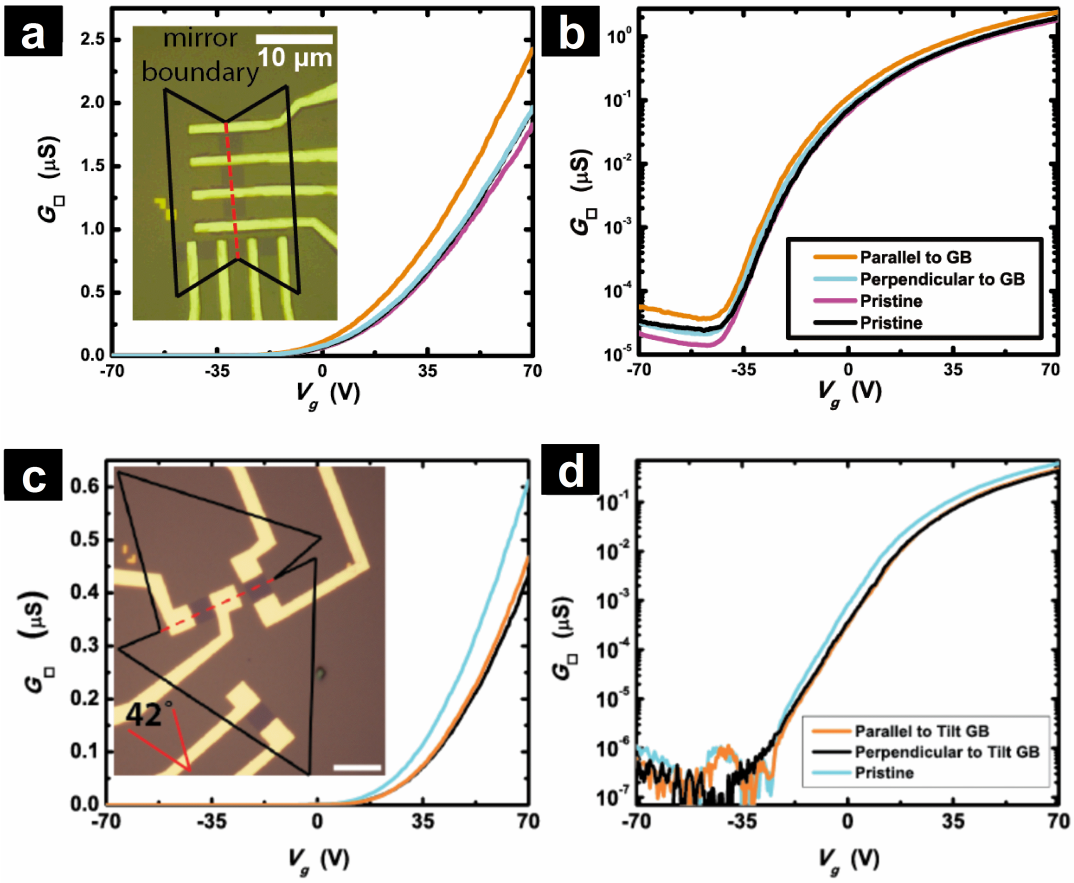

FIGURE 4.6. Linear and logarithmic electrical transport transfer curves of FETs fabricated from a mirror twin MoS_2 island and tilt (42 deg) boundary island shown in the insets of a and b, respectively. The curves correspond with pristine regions (magenta and black), and regions containing a grain boundary running perpendicular (cyan) and parallel (orange) to the flow of electrons. All data were measured at room temperature, using the Si growth substrate as a back-gate and a source–drain bias of 500 mV. Reproduced from [112].

CHAPTER 5

Rhenium Disulfide: Studies in Anisotropic TMDCs

This chapter was adapted from two of our publications. The first was adapted with permission from D. A. Chenet et al., "In-Plane Anisotropy in Mono- and Few-Layer ReS_2 Probed by Raman Spectroscopy and Scanning Transmission Electron Microscopy", Nano Letters, 15 (9), 5667-5672. Copyright (2015) American Chemical Society. The second was partially adapted with permission from O. B. Aslan, D. A. Chenet et al., "Linearly Polarized Excitons in Single- and Few-Layer ReS_2 Crystals", ACS Photonics, 3 (1), 96-101. Copyright (2015) American Chemical Society.

5.1. Background

Rhenium disulfide (ReS_2) is a semiconducting transition metal dichalcogenide (TMDC) with an optical bandgap around 1.4 eV in bulk crystals synthesized by the vapor transport method [110, 34]. The layered TMDCs, including MoS_2, $MoSe_2$, WS_2, and WSe_2, have generated significant interest in the research community as stable direct-gap semiconductors in the monolayer limit with properties tunable by interlayer coupling [79, 59, 113], as well as potential for electronic, piezotronic, and optoelectronic applications [14, 80, 62, 121, 106, 97, 45]. ReS_2, as a thin film material, has only recently attracted attention, with reports of the photoluminescence, Raman scattering response, and transconductive properties of ReS_2 which have been measured in the few-layer limit [110, 15]. These previous investigations did not identify significant variation in the vibrational, optical, and electrical properties of ReS_2 crystals as a function of layer thickness, suggesting that the interlayer coupling is weaker in this material than in the more widely studied TMDC crystals. While these studies were crucial first steps in the thin-film characterization of this material, an important aspect remains unaddressed:

the role of in-plane anisotropy in single- and few-layer crystals. Strong anisotropy of the optical and electrical properties of ReS_2 has been established for bulk crystals [71, 26, 36] and is also expected in thin layers. Additionally, the Raman scattering response, while not yet directly characterized, is also expected to be anisotropic based upon studies performed previously on structurally similar $ReSe_2$ [118] and thus to provide a simple optical means of establishing the crystallographic orientation of single- and few-layer samples. This work presents a detailed investigation of the Raman scattering in single- to few-layer ReS_2. It demonstrates that, like the previously measured bulk optical and electrical properties, the Raman scattering response is also anisotropic. It is also shown that the anisotropic angle- and polarization-resolved Raman spectra of ReS_2 provide a method for the determination of crystallographic orientation by a purely optical technique, as confirmed using scanning transmission electron microscopy (STEM) to image the crystal lattice. Analysis of the difference in frequency between appropriate Raman modes is also found to provide a means of determining the thickness of a given sample.

5.2. Structure

In contrast to the more studied group VI metal dichalcogenides like MoS_2 and WSe_2, ReS_2 monolayers exhibit a distorted 1T structure as the stable phase, as shown in Figure 5.1a [117, 86]. Previous studies of bulk ReS_2 have noted that, due to the extra valence electron on the group VII rhenium atoms, ReS_2 exhibits both metal-chalcogen and metal-metal bonds. The metal-metal bonds are responsible for creating a superlattice structure of rhenium chains, indicated by a black double arrow in Figure5.1a. These chains distort the monolayer crystal from the more symmetric 1T structure [34, 22, 24]. Experimentally, crystals synthesized by vapor transport cleave with well-defined edges parallel to the rhenium chains, typically denoted as the b-axis, providing a rapid method of crystal orientation identification convenient for studying the anisotropic optical and electrical properties [36].

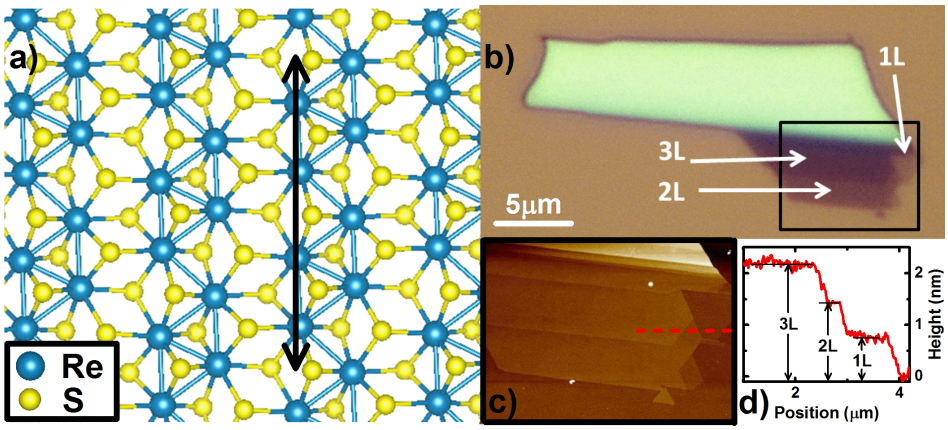

FIGURE 5.1. Crystal structure and an example of an exfoliated ReS_2 flake. (a) Ball-and-stick model of ReS_2 (yellow, S; teal, Re) monolayer with direction of the Re chains represented by the black double arrow. (b) Optical micrograph of an exfoliated sample. (c) Atomic force microscopy (AFM) image of the sample indicated in the box in the optical micrograph. (d) The AFM scan along the dotted red line in (c). Reproduced from [12].

While exfoliated mono- to few-layer samples that are attached to bulk crystals with well-defined edges can be found, there is often ambiguity as to whether thinner samples also cleave along the b-axis, as well as which of the cleaved edges follows the b-axis. Moreover, recent progress and the technological demand for producing large-scale samples of TMDC thin films by chemical vapor deposition [112, 39] necessitate the development of non-destructive techniques for determining crystal orientation in thin film materials that are independent of the preparation technique [118, 122, 69].

5.3. Raman Polarization

For this study, bulk ReS_2 crystals (source: HQ Graphene) were mechanically-exfoliated onto silicon dioxide (285 nm) on silicon substrates. Figure 5.1b shows an optical micrograph of a single flake that contains regions of monolayer (1L), bilayer (2L), and trilayer (3L) attached to a thicker bulk-like flake. Atomic force microscopy imaging, depicted in Figure 5.1c and Figure 5.1d, confirms a thickness of ~0.7 nm per layer [110].

The anisotropic behavior of thin ReS_2 can be probed using angle-resolved polarized Raman spectroscopy, which has been previously used in a wide variety of applications including studying strain-induced changes in the electronic structure of graphene [40], as well as determining the orientation of $ReSe_2$ [118] and black phosphorus crystals [122, 119]. The Raman spectra is measured in a backscattering geometry using a 532-nm laser with a fixed linear polarization. The sample is rotated to an angle ϑ between the incident polarization and the direction normal to the cleavage plane (depicted by a white dashed line in all subsequent figures). The scattered light is measured by a spectrometer with a 2400 l/mm grating, using a linear polarizer to independently measure components parallel and perpendicular (cross) to the incident laser polarization. The spectra for unpolarized detection can also be studied by summing the parallel and perpendicular intensities after correcting for the relative collection efficiency. This provides Raman spectra equivalent to those that would be measured with an ideal, polarization-independent detection system.

Figure 5.2a shows the unpolarized Raman spectrum for a ReS_2 monolayer. At least 16 Raman-active vibrational modes can be identified. A previous report on the $ReSe_2$ system, which possesses the same distorted crystal structure, predicted 18 Raman-active vibrational modes [118]. For the present study, attention is restricted to the range of Raman shifts between 120 cm-1 and 240 cm-1, since the strongest modes occur in this frequency range (Figure 5.2b). Figure 5.2c depicts the evolution of the Raman spectrum as the sample is rotated about the surface normal. The intensity of each peak varies strongly with angle, while the peak positions are unchanged. Before examining the orientation dependence more closely, it is worthwhile to study the layer dependence of the unpolarized Raman spectra (Figure 5.3).

5.3.1. Layer Dependence. Figure 5.3a is a micrograph of a sample containing regions that are 1L, 2L, 3L, and 4L thick. A few of the layers cleaved with well-defined edges, as highlighted with black dashed lines. Figure 5.3b shows the Raman spectra for each region at

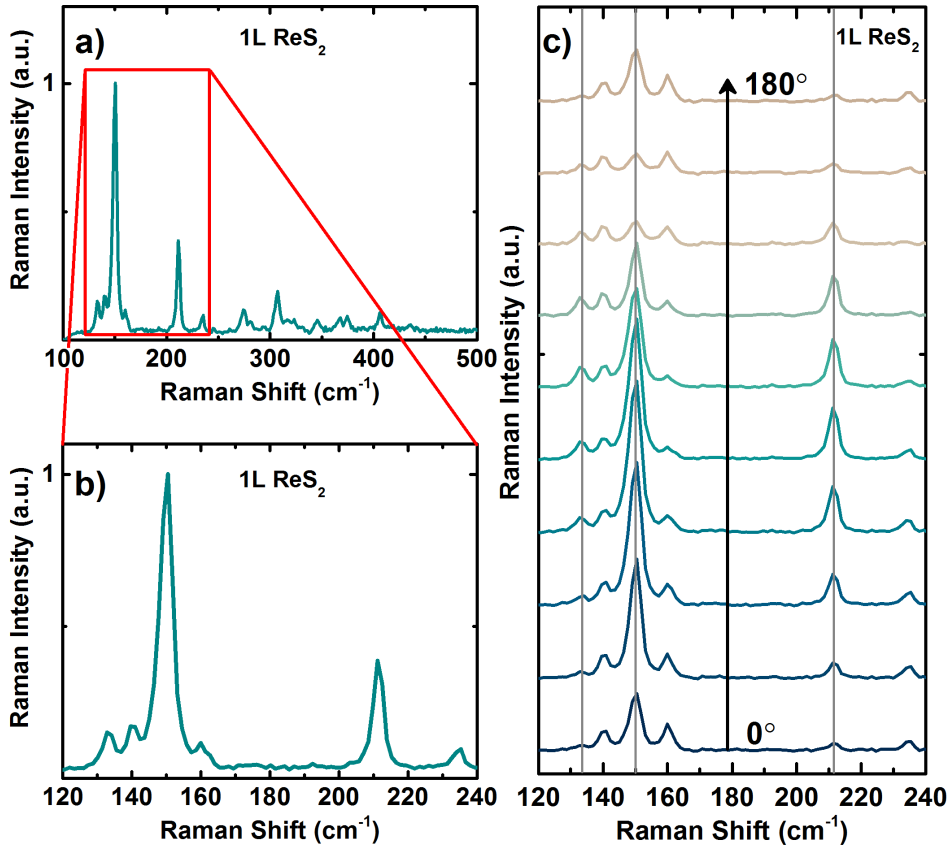

FIGURE 5.2. Raman spectra for monolayer ReS_2. Full (a) and detailed (b) view of the monolayer ReS_2 Raman spectrum. (c) Unpolarized Raman spectra as a function of sample orientation angle. The spectra taken every 20° from 0° to 180° by rotating sample about its surface normal are presented with a vertical offset and with relative intensities preserved. Reproduced from [12].

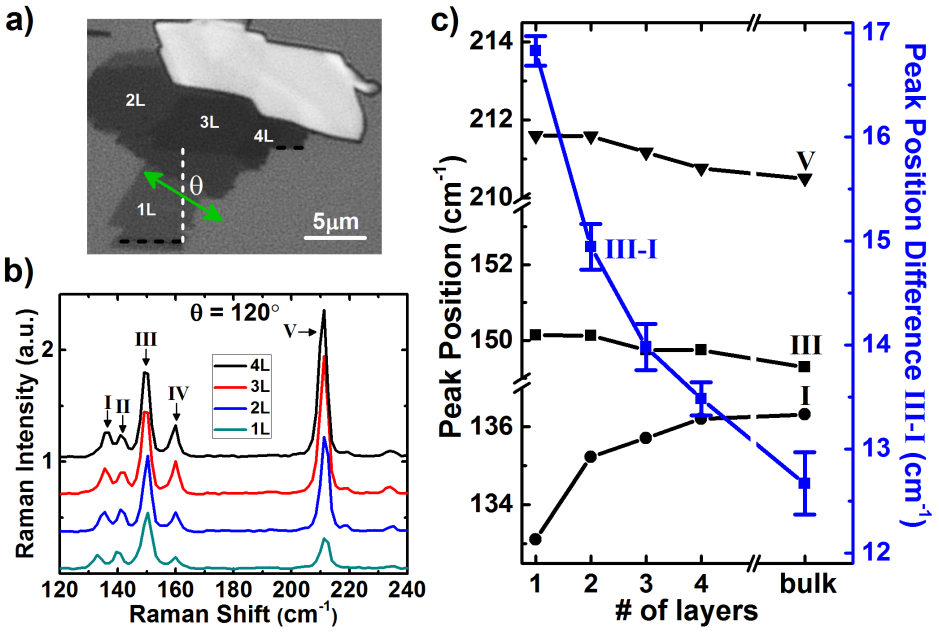

FIGURE 5.3. Raman spectra of ReS_2 samples as a function of layer thickness. (a) Optical micrograph of 1L, 2L, 3L, and 4L samples. The dashed black lines indicate the well-defined edges as cleaved. The green double arrow represents the polarization of the 532 nm incident laser. (b) Stacked plot of Raman spectra in 1L, 2L, 3L, and 4L ReS_2 taken with sample at an orientation of $\vartheta = 120°$. (c) Frequencies for modes I, III, and V, labeled in (b), as a function of thickness (1L, 2L, 3L, 4L, and bulk) on the left vertical axis with the frequency difference between modes I and III on the right vertical. Reproduced from [12].

a fixed orientation ($\vartheta = 120^{o}$). This orientation is chosen because all modes of interest are sufficiently strong for further analysis. For simplicity, the modes are labeled from lowest to highest wavenumber with Roman numerals I through V, with approximate peak positions of 135 cm^{-1}, 141 cm^{-1}, 150 cm^{-1}, 160 cm^{-1}, and 211 cm^{-1} This study reveals that it is in fact possible to quantify the number of ReS_2 layers by examining the Raman peak positions, as has been shown for other 2D materials [59]. Figure 5.3c displays the peak positions of Raman modes I, III, and V as a function of thickness. The positions of modes III and V change only marginally from one to four layers, as does mode IV (not shown). The position of mode I, on the other hand, varies from 133.1 $\pm$ 0.1 cm^{-1} in the 1L to 136.2 $\pm$ 0.2 cm^{-1} in the 4L. The weaker mode II shows a similar thickness-dependent tuning. The III-I frequency

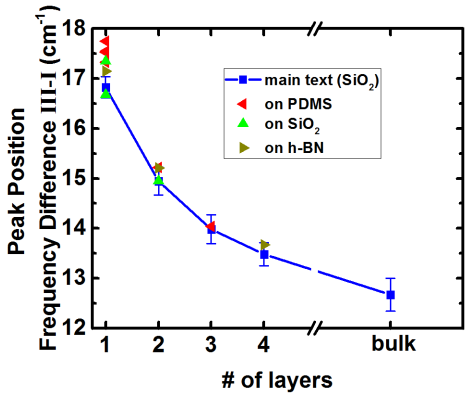

FIGURE 5.4. Substrate dependence on frequency difference betweenmodes III and I. Reproduced from [12].

difference is 16.8 ± 0.2 cm^{-1}, 14.9 ± 0.3 cm^{-1}, 14.0 ± 0.3 cm^{-1}, and 13.5 ± 0.2 cm^{-1} for monolayer, bilayer, trilayer, and tetralayer, respectively and converges to 12.7 ± 0.3 cm^{-1} in the bulk. (Note: The error bars derive from the difficulty of fitting overlapping Lorentzians.) This result provides a method for identifying thickness of samples in the few-layer regime like the technique used for MoS_2 [59]. Since the peak positions do not shift significantly with polarization angle, these results are robust enough to allow comparison between different samples. Crucially, this analysis requires using an orientation where all of the relevant peaks are sufficiently strong. This can be achieved simply by rotating the sample. This experiment was performed on numerous samples on different substrates and the behavior is consistent (see Figure 5.4).

Figure 5.5 depicts the orientation-dependent polarization response of mode V in the 4L region with cross-polarized (blue) and parallel-polarized (red) collection, as well as unpolarized (black) collection. The cross- and parallel-polarized spectra yield 4-lobed and 2-lobed shapes, respectively. With this data, it is possible to gain insight into the character of the Raman tensor 118. For the purposes of developing a convenient optical method to determine crystallographic orientation, focused is directed towards the parallel polarization data for which the Raman response is significantly stronger and, thus, easier to fit.

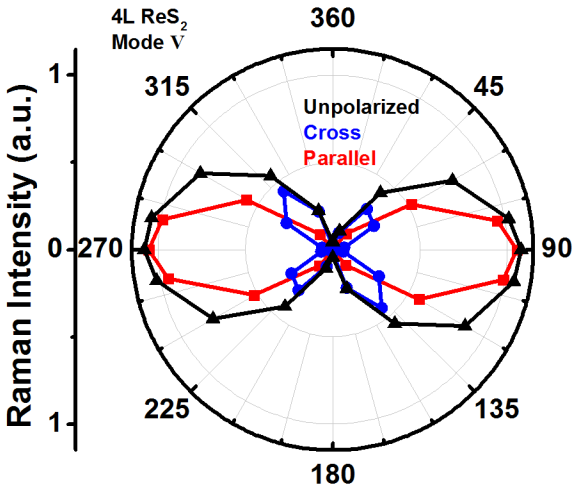

FIGURE 5.5. Raman intensity of mode V in the 4L region with unpolarized (black), cross-polarized (blue), and parallel-polarized (red) collection. Reproduced from [12].

In order to fit the angle- and polarization-resolved Raman intensities, we must return to Equation 3.12 (restated here for convenience):

$$I \propto |\hat{e}_i \cdot \widetilde{R} \cdot \hat{e}_s|^2$$

, where I is the scattered intensity, $\widetilde{R}$ is the Raman tensor for a given mode, and $\hat{e}_i$ and $\hat{e}_s$are the unit vector representations of the incident and scatter light polarizations, respectively. With the incident light wavevector perpendicular to the layer plane, the relevant part of the Raman tensor has the general form:

$$\widetilde{R} = \begin{bmatrix} a & b \\ b & c \end{bmatrix} \tag{5.29}$$

and can be transformed from a rotated coordinate frame (mismatch between crystal axes and laboratory frame) using rotation matrices $\widetilde{Q}$ and $\widetilde{Q}^T$:

$$\widetilde{Q} = \begin{bmatrix} \cos\theta & \sin\theta \\ -\sin\theta & \cos\theta \end{bmatrix}$$

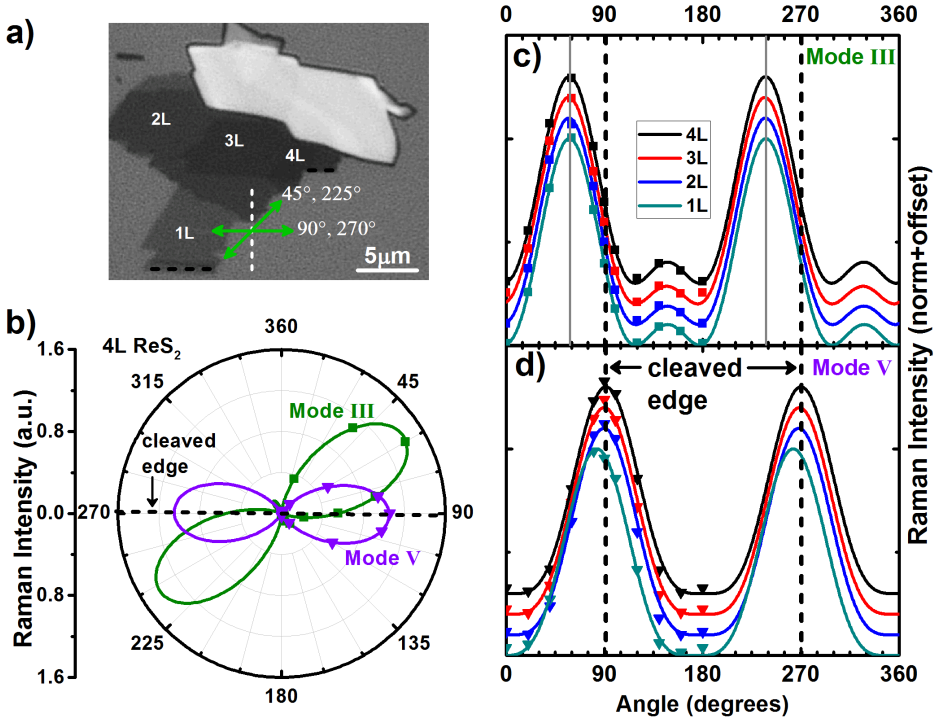

FIGURE 5.6. Angle-resolved Raman response with parallel-polarized collection for modes III and V, centered at ~150 cm^{-1} and 211 cm^{-1}, respectively. (a) Optical micrograph of an exfoliated ReS_2 sample. The white dashed line represents the reference sample orientation. (b) Angle-resolved Raman intensities of modes III (green squares) and V (purple triangles) in a 4L sample of ReS_2 presented in a polar plot. (c) Variation with sample orientation of the intensity of mode III for samples of 1L-4L thickness. The data for each layer thickness are normalized and offset in the plot. The grey solid lines represent the angle of maximum intensity. (d) As in (c) for mode V. Reproduced from [12].

$$\widetilde{Q}^T = \begin{bmatrix} \cos\theta & -\sin\theta \\ \sin\theta & \cos\theta \end{bmatrix} \tag{5.30}$$

. After performing the transformation of the Raman tensor, we obtain the following equation that we use to fit the Raman intensities with scattered polarization parallel to the excitation polarization:

$$I_{\parallel} \propto |a\sin^2\theta + 2b\sin\theta\cos\theta + d\cos^2\theta|^2 \tag{5.31}$$

.

Figure 5.6 presents the parallel polarization Raman response of modes III (green) and V (violet). Figure 5.6b is a polar plot of the intensity of modes III and V for the 4L region. Mode III exhibits a maximum intensity at an angle of ~58°. Mode V exhibits a maximum intensity at an angle of ~91°, which also happens to be parallel to one of the edges of the exfoliated flake. These two modes were previously calculated in the literature by DFT simulations. Mode III was shown to consist of mostly in-plane vibrations and mode V was shown to contain out-of-plane vibrations of the sulfur atoms along with in-plane vibrations of the rhenium atoms in the direction of the b-axis [110]. It is hypothesize that the angle of maximum intensity for mode V should be in the direction of the b-axis. Next, the consistency of the Raman polarization dependence of each mode as a function of layer thickness is examined. Figure 5.6c depicts the polarization dependence of mode III in the 1L, 2L, 3L, and 4L regions. This mode polarization behavior is unchanged for all 4 different thicknesses, with maximum intensity located at ~58°. Figure 5.6d shows the thickness dependence of mode V. In contrast to mode III, the polarization of mode V varies slightly with thickness, with maximum intensity for this mode at 83° for 1L, 90° for 2L, and 91° for 3L and 4L. This variation may be due to interlayer coupling, substrate interactions or strain induced from the mechanical exfoliation process, the effects of which are expected to diminish in each subsequent layer. It could also be due to the fact that the excitation photons

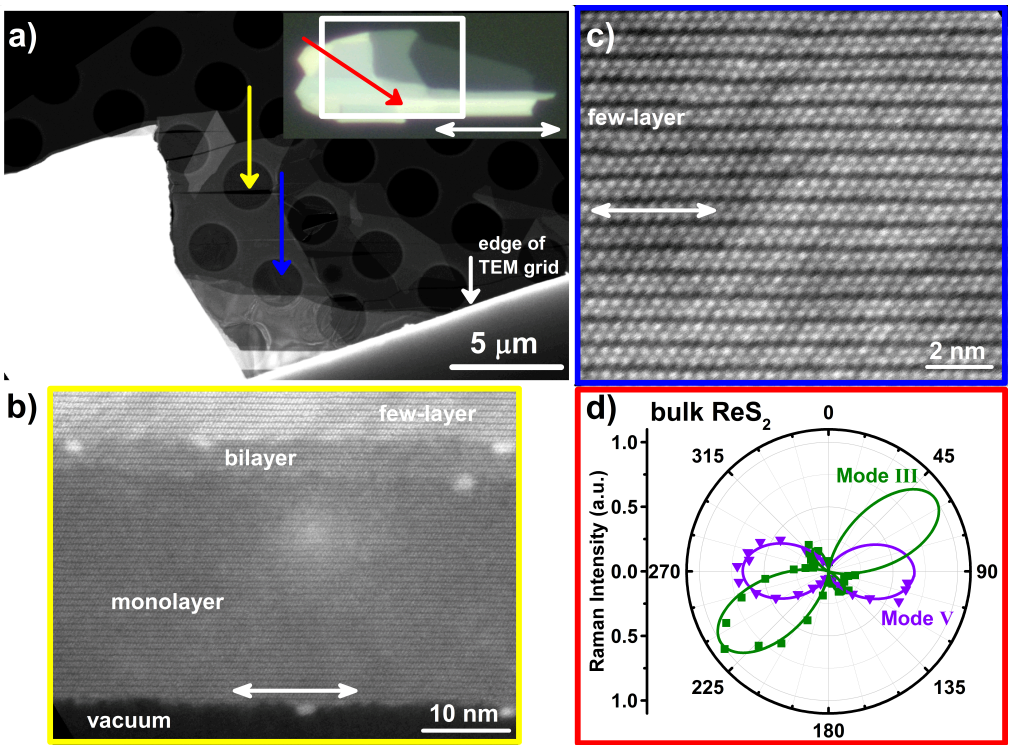

FIGURE 5.7. Annular dark-field scanning transmission electron microscopy (ADF-STEM) of bulk to monolayer ReS_2. (a) Low magnification ADF-STEM image of ReS_2 sample on a Quantifoil TEM grid. Inset: optical micrograph of sample on PDMS before transfer. (b) Medium magnification ADF-STEM image of suspended ReS_2 where the sample tore during the transfer process. (c) High magnification ADF-STEM image of a few-layer region. (d) Polarization- and orientation-resolved Raman spectra of bulk region. White double arrows depict direction of rhenium chains in (a)-(c). Reproduced from [12].

are above the bandgap and the Raman scattering contains interactions with the electronic structure, which is also expected to anisotropic. The variation in mode V with layer thickness is not reflected in the behavior of mode III, suggesting that mode III is less sensitive to the cause of this variation. Nonetheless, it is clear that mode V displays a maximum intensity when the excitation is roughly parallel to one of the edges of the cleaved crystal. Consistent behavior has been observed on $>$ 20 samples on different substrates including at least 4 of monolayer, bilayer, and trilayer thickness.

5.3.2. Raman Correlated with Transmission Electron Microscopy. Figure 5.7 demonstrates the use of annular dark-field scanning transmission electron microscopy (ADF-STEM) to image the crystal lattice and confirm that the Raman spectra can be used to determine the crystal orientation. Figure 5.7a shows the low-magnification ADF-STEM image of a ReS_2 sample that was transferred onto a Quantifoil TEM grid. The sample contains regions ranging from bulk to monolayer, with some regions that are completely suspended. During the transfer process, some regions tore with well-defined edges, such as the one marked by the yellow arrow. Figure 5.7b shows a higher magnification image of this region and confirms that the b-axis (rhenium chains) runs parallel to the cleaved edge. Figure 5.7c presents a higher magnification ADF-STEM image taken from the few-layer region marked by the blue arrow. The bright spots represent the rhenium atoms and the rhenium chains, which run in a direction ~90° measured clockwise from the vertical, are easily visible. Figure 5.7d depicts the parallel polarization response of the Raman spectra for modes III (green) and V (violet) taken on the bulk region of the sample, as denoted by the red arrow in Figure 6a. Mode III is a maximum at an angle of ~55° measured clockwise from the vertical and is denoted by the green line in Figure 5.7c. Mode V is a maximum at an angle of ~91° degrees, which corresponds to the direction parallel to the rhenium chains.

5.3.3. Reflection Contrast and Photoluminescence. Next we use reflection contrast and photoluminescence spectroscopy to explore the anisotropic optical response of ReS_2. Using methods described above, we first determine the orientation of the b-axis. We then perform reflection contrast measurements of samples exfoliated onto transparent polydimethylsiloxane (PDMS) substrates. Samples were illuminated with a tungsten lamp through a linear polarizer in conjunction with a beamsplitter and the reflected signal was collected with a liquid nitrogen cooled CCD array. Differential reflectance was measured between the sample and the substrate. Figure 5.8a shows the reflection contrast spectra as a function of polarization of incident light. Direct transitions 1 and 2 are labeled with black

and red arrows, respectively. It can clearly be seen in Figure 5.8b that, by fitting the spectral weights of the two optical transitions, excitons 1 and 2 have a polarization dependence and neither are parallel (or perpendicular) to the b-axis, which is labeled with a blue line in Figure 5.8b.

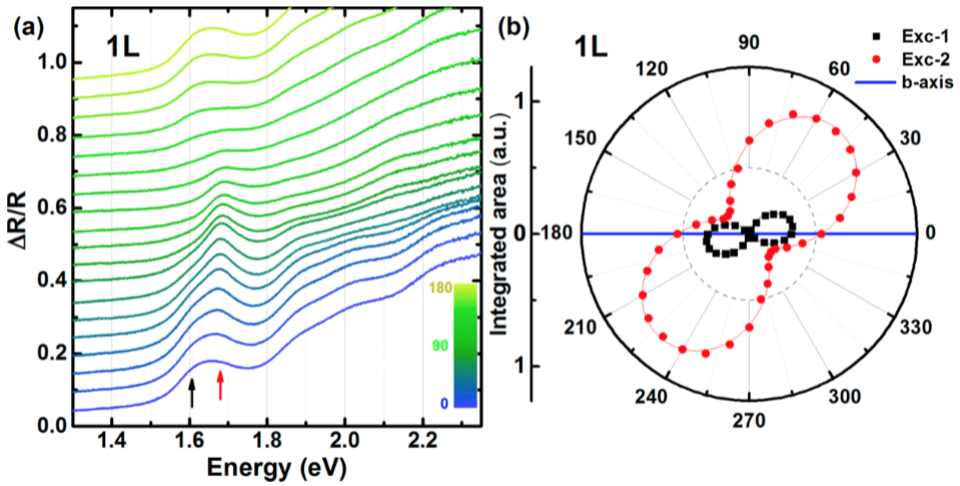

FIGURE 5.8. Anisotropic optical response of 1L ReS_2. a) Reflection contrast measurements as a function of polarization angle with respect to the sample orientation. Optical transitions are labeled with black (exciton 1) and red (exciton 2) arrows. b) Integrated areas of excitonic transitions 1 and 2. Blue line represents the orientation of the b-axis (cleaved edge). Reproduced from [2].

We next measure the anisotropic photoluminescence of a 3L sample using a Renishaw InVia microscope with a linearly-polarized 532 nm laser and a spectrometer equipped with a 600 l/mm grating. We use a polarization filter in front of the spectrometer and rotate the sample for each spectra. Figure 5.9a shows the corresponding reflection contrast spectra and Figure 5.9b shows the PL response. It can be seen that the polarized PL emission follows the polarized absorption. The exact origin of this anisotropy is still unknown; however, our results agree with previous measurements performed on bulk samples [71].

5.3.4. Raman Correlated with DC Electric Transport Measurements. In order to determine whether the electrical conductivity of monolayer ReS_2 exhibits anisotropic

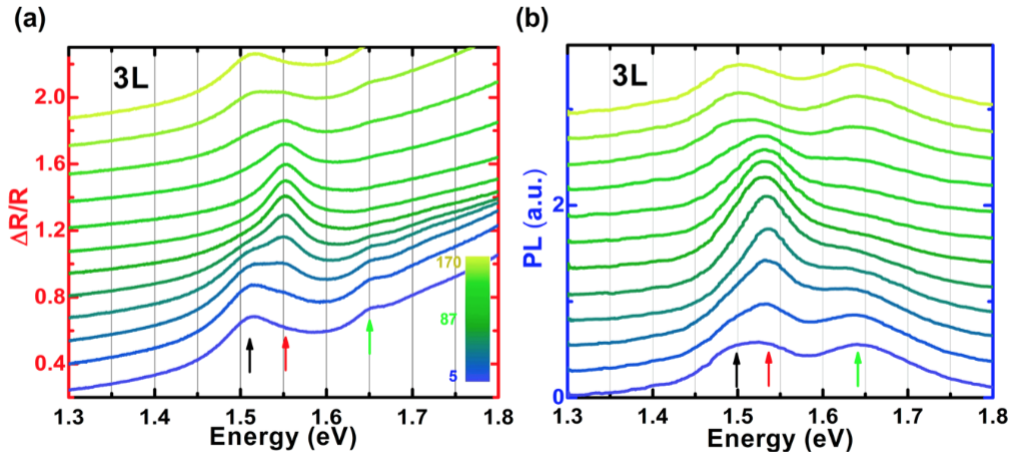

FIGURE 5.9. Anisotropic optical response of 3L ReS_2. a) Reflection contrast measurements as a function of polarization angle with respect to the sample orientation. Optical transitions are labeled with black (exciton 1), red (exciton 2), and green (exciton 3) arrows. b) Photoluminescence spectra as a function of emission polarization. Reproduced from [2].

behavior that can be predicted by the Raman spectra, we compare the Raman data with electrical transport measurements of monolayer ReS_2 field-effect transistors (FETs). Figures 5.10a shows an array of FETs built on a single monolayer ReS_2 flake that has been etched into channels set at different angles with respect to the crystal axis. The array contains 15 FETs at a spacing of 22.5°. Before fabrication, the orientation of the monolayer was first determined optically and with angle-resolved polarized Raman spectroscopy. The monolayer was then transferred onto a flake of hexagonal boron nitride and patterned into devices using electron beam lithography and O_2 plasma etching. Figure 5.10b is a schematic cross-section of two devices. All devices have identical 1 μm x 1 μm square channels with identical contact areas, a common source electrode, and a global silicon back gate. Figure 5.10c shows a transfer curve of a single FET. The measurements were performed in a vacuum probe station, at room temperature with a drain voltage of 500 mV. The curve shows n-type behavior with 2-terminal field-effect mobility of 4.34 cm^2/V-s and an on/off ratio greater than 10^6. Additionally, the device exhibits very little hysteresis. All of the devices exhibit similar Ohmic contacts, negligible hysteresis, field-effect mobilities in the range of 2.73-4.73 cm^2/V-s, and on/off

ratios exceeding 10^5. Next, we compare the electrical transport properties as a function of angle. Figure 5.10d shows the on-state conductance (at V_{bg} = 40 V) and 2-terminal field-effect mobility as a function of angle. It can be clearly seen that both the conductance and mobility vary strongly with orientation of the channel: the on-state conductance varies from 1.26 μS to 2.67 μS, while the mobility varies from 2.73 cm^2/V-s to 4.73 cm^2/V-s. Both are highest in the direction parallel to the cleaved edge of the crystal (vertical dashed black lines) and peak intensity of Raman mode V (vertical purple lines), and both are lowest perpendicular to this axis. This result is consistent with what has been observed previously in bulk n-type ReS_2 crystals and suggests that mode V can be used to predict the direction of the b-axis, which is the direction of highest electrical conductivity [36]. However, it must be acknowledged that large contact resistances make an accurate quantification of the anistropy impossible. Four-terminal resistivity measurements are necessary to further characterize this property. Nonetheless, the behavior can be confirmed over several sets of devices.

5.3.5. Conclusion. These results confirm the utility of angle-resolved polarized Raman spectroscopy in determining the crystal orientation in layered TMDCs possessing the distorted 1T structure. These observations and conclusions are supported by atomic-scale imaging with ADF-STEM and further correlated with optical spectroscopy and DC electrical transport measurements. It will prove invaluable in the future study of the anisotropic optical and electrical properties in thin film ReS_2. ReS_2, however, is only just one of the TMDCs exhibiting the distorted 1T phase to be explored in the few-layer limit and lessons learned here should serve to inform future experiments in similar material systems.

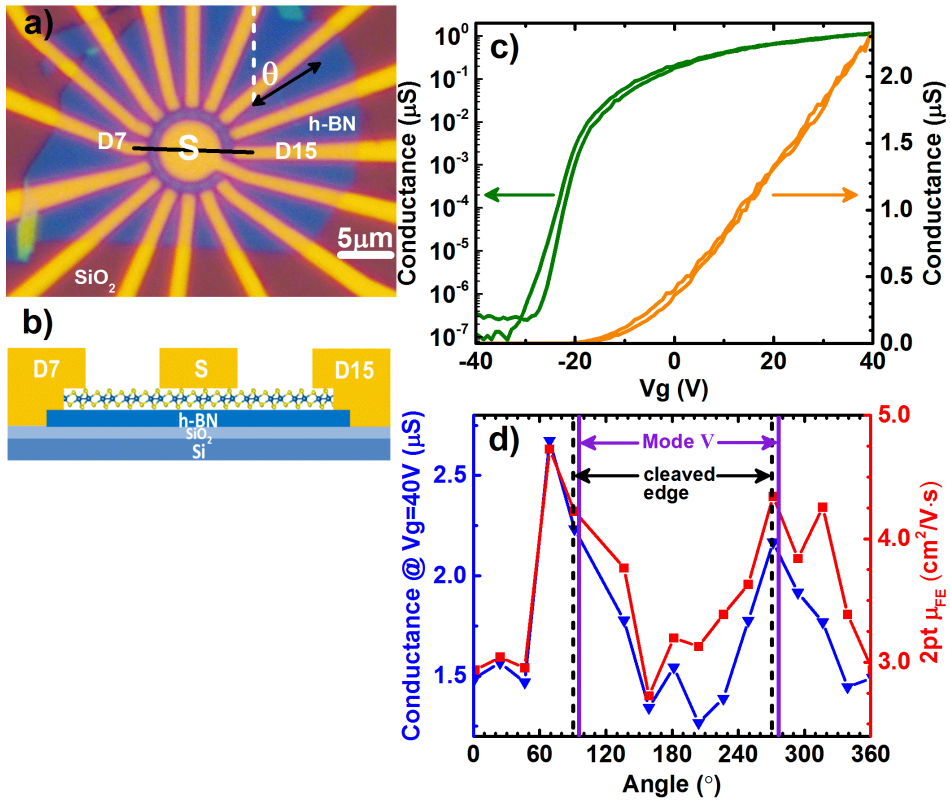

FIGURE 5.10. Angle-dependent electrical transport in monolayer ReS_2 transistors. (a) Optical micrograph of an array of 15 transistors fabricated in monolayer ReS_2 on h-BN/SiO_2/Si substrate. (b) Schematic representation of the cross-section for 2 transistors, with the section cut represented by the black line in (a). (c) Transfer curve for the device labeled "D7" in (a), with the conductance plotted on logarithmic (green) and linear (orange) scales on the left and right y-axes, respectively. (d) Conductance (blue) and 2-terminal field-effect mobility (red) for each device in (a) as a function of the angle between the device channel and the vertical. Reproduced from [12].

CHAPTER 6

Transition Metal Dichalcogenides Alloys

6.1. Background

The discovery of the indirect to direct bandgap transition in the Group VI transition metal dichalcogenides (TMDCs), namely MoS_2, WS_2, $MoSe_2$, WSe_2, has brought these materials to the forefront of 2D material research in the past several years. No longer dominated by graphene, the field has opened up to explore the semiconducting properties of these TMDCs for digital logic [74, 63, 95], valleytronic [45, 48, 65, 80, 106, 120, 127], and piezotronic applications [20, 121, 131], as well as studies in fundamental physics [103, 105]. In addition to the efforts towards synthesizing and characterizing the high-quality, pure versions of these materials, there has recently been considerable effort extended towards the synthesis of heterostructures and alloys. Recent reports on alloys of $Mo_{1-x}W_xS_2$ [52] and $MoS_{2(1-x)}Se_2$ [25, 50, 67] have demonstrated continuous optical bandgap tuning throughout the range enveloped by the pure compounds at x=0 and x=1. These fundamental studies were essential to the continued engineering of 2D semiconductor material systems. However, to this point, there are two very important Group VI TMDCs that have remained unexplored: $MoTe_2$ and WTe_2.

$MoTe_2$, in it's most commonly studied α-phase (2H), is a low bandgap (1.0 eV in the bulk; 1.1 eV in the monolayer) semiconductor. However, $MoTe_2$ is markedly different from its more widely studied counterparts in that it possesses a high temperature β-phase (1T') that is also metastable at room temperature [46].

β-$MoTe_2$ is a semimetal and is typically synthesized by similar chemical vapor transport techniques as the α-phase except that it is quenched at high-temperature, before it reaches

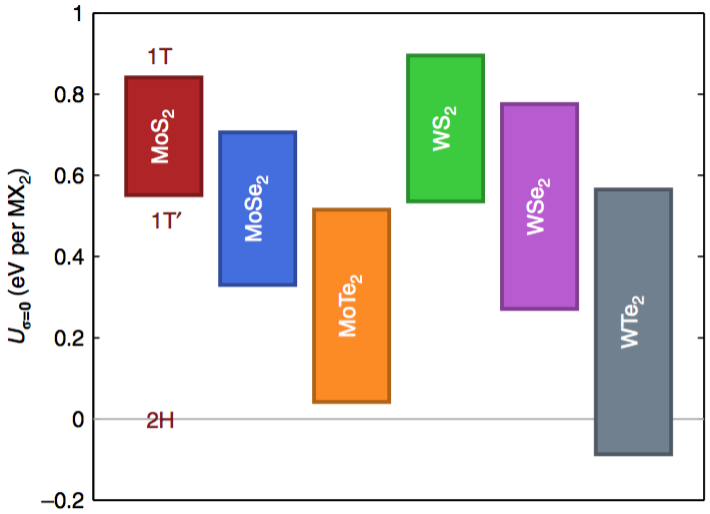

FIGURE 6.1. Energy difference between the 2H, 1T, and 1T' phases in Group VI TMDCs. Reproduced from [21].

the phase transition temperature. β-$MoTe_2$ has recently been gaining considerable attention due to its potential as another candidate, in addition to semimetal WTe_2 (1T"), for studying Weyl fermion physics [105, 103].

In addition to the study of fundamental physics in condensed matter, there are potential technological implications for a material system with a semiconductor/semimetallic phase transition. Duerloo et al. reported that, through density functional theory calculations, it is expected that the transition from α-phase to β-phase could occur at room temperature with the application of approximately 0.5-1.5% strain [21].

Unfortunately, these levels of strain are slightly higher than required to have a broad technological relevance. However, in follow-up publications, they predicted that alloying $MoTe_2$ with a small fraction W would allow the tuning of properties from pure $MoTe_2$, a material with a phase transition temperature of 920^{o}C, to pure WTe_2, a material whose only known stable phase is a semimetallic 1T" phase, potentially with a composition inbetween that possesses a phase transition that occurs near room temperature [19]. This phase transition could then, theoretically, be driven by strain, heating/cooling, or charge density [68]. A material with such properties would possess potential in applications such as non-volatile

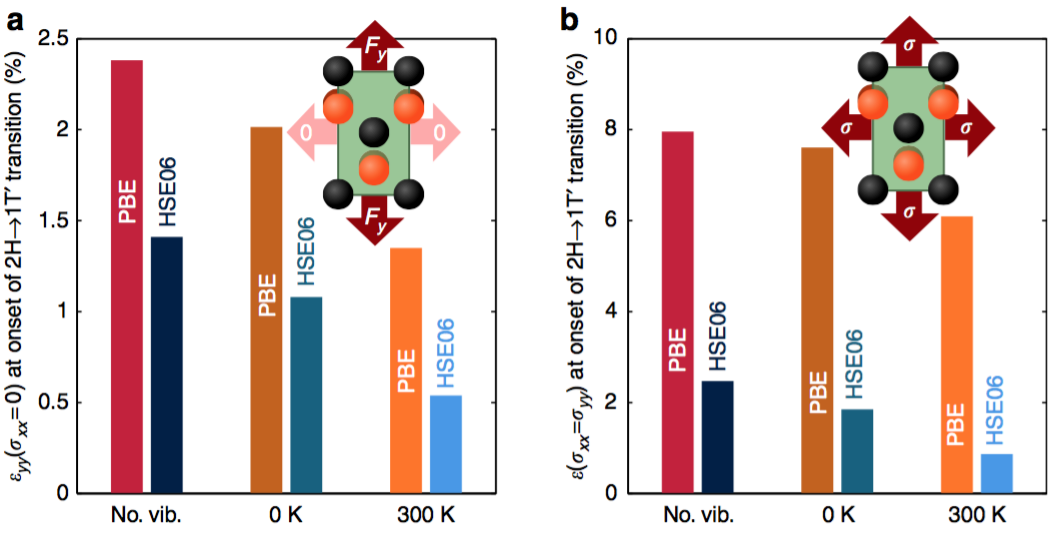

FIGURE 6.2. Strain required to create 2H–>1T' phase transition in $MoTe_2$. Reproduced from [21].

phase change memory, strain sensors, and optical modulators.

6.2. Composition and Structure Characterization

In order to study the crystal structure as a function of composition, we synthesize bulk crystals with varying molybdenum to tungsten ratios using the chemical vapor transport method. We then employ several different characterization techniques to both confirm our ability to drive a phase change by composition as well as study the properties of the separate phases. The characterization techniques include electron dispersive x-ray spectroscopy (EDX), Raman spectroscopy, and DC electrical transport measurements.

The first observations that can be made of the bulk crystals can be done on the macroscopic scale. Bulk crystals that were very high in tungsten content possessed a needle-like morphology (see Figure 6.4: left), whereas crystals with low tungsten content had a less-defined prismatic morphology (see Figure 6.4: right). These are early indications of structure as 1T' and 1T" crystals are known to exhibit highly anisotropic, and often needle-like, morphologies. Occasionally, crystals presumed to be 2H in appearance had regions with needle-like protrusions, suggesting a mixture of crystal phases in a single growth, potentially

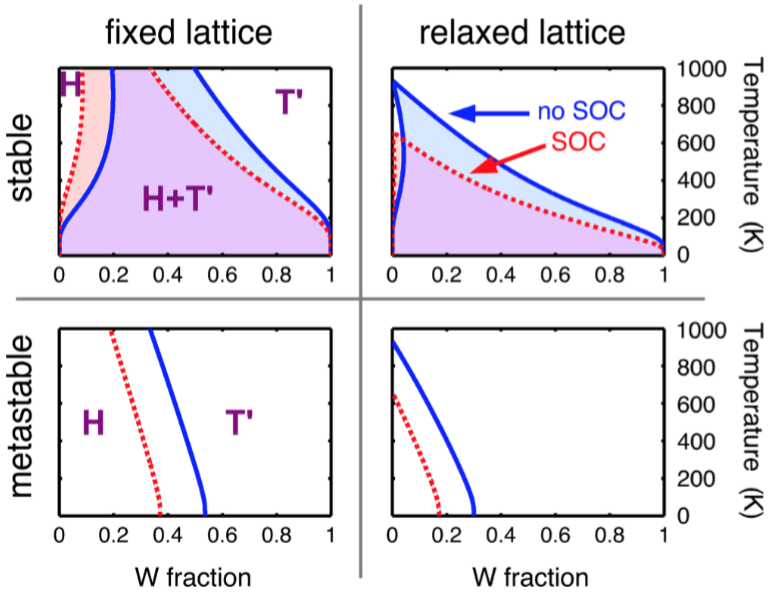

FIGURE 6.3. Theoretical phase diagram for $Mo_{1-x}W_xTe_2$ alloy. Reproduced from [19].

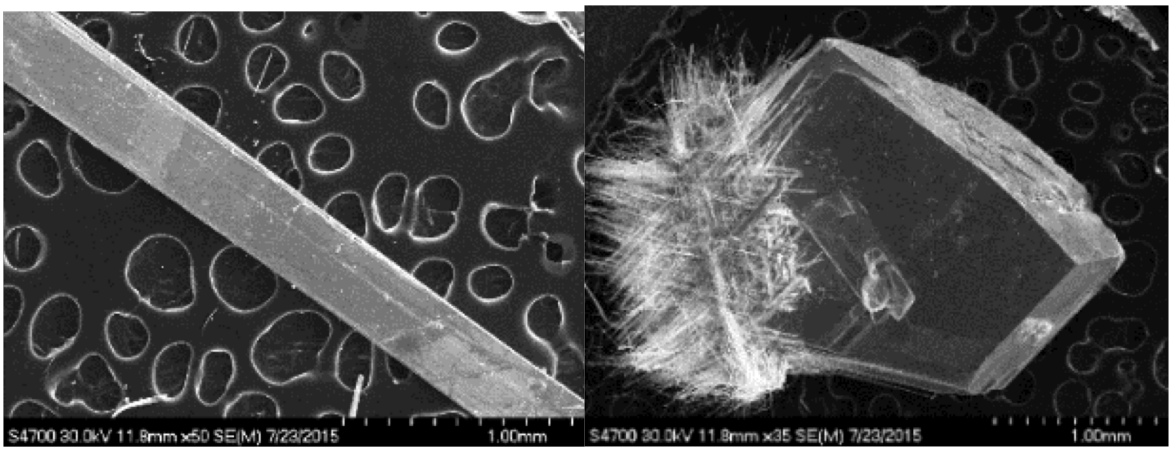

FIGURE 6.4. Scanning electron micrograph of bulk 1T" and 2H $Mo_{1-x}W_xTe_2$ alloy crystals.

due to a temperature and/or kinetics gradient during the growth process. In general, these crystals were excluded from the exfoliation process as it would add confusion to the analysis.

The compositions of these bulk crystals were studied by EDX. The calibration of the EDX was confirmed using pure WTe_2 and α-$MoTe_2$ grown by flux growth and yielded transition metal:chalcogen ratios of 1:2. Alloys with tungsten content as high as x=0.27 were

characterized in this study.

6.3. Raman Characterization

In order to further confirm the structure of each alloy, we performed Raman spectroscopy on the bulk crystals. The reduction of symmetry associated with a transition from the 2H to either the monoclinic 1T' or orthorhombic 1T" phase is expected to produce an observable shift in the Raman spectra due to the selection rules for the 2H (D_{6h} in bulk), 1T' (C_{2h}), and 1T" (C_{2v}) point group symmetries [46, 53]. For this study, we focus on thicker samples (N>10) in order to minimize effects due to frequency shifts associated with changes in the number of layers as well the tendencies of thinner samples to degrade quicker, as per several reports.

The Raman spectra of 2H $MoTe_2$ has been well-studied in previous works and is expected to produce strong first-order Raman scattering at 170 cm^{-1} and 235 cm^{-1} associated with the A_{1g} and E_{2g} modes in the bulk [27, 98, 123]. More recently, there have been a few reports on the Raman scattering in β-$MoTe_2$ and WTe_2. To illustrate the differences of the Raman spectra of the 3 pure materials, we plot them together in Figure 6.5(left). We highlight 3 of the Raman-active modes that are unique to each pure crystal with green (WTe_2), black (α-$MoTe_2$), and red (β-$MoTe_2$) dashed lines. These correspond to A_1^2 (green), E_{2g} (black), and A_g (red) modes in WTe_2, α-$MoTe_2$, and β-$MoTe_2$, respectively [46, 53, 43]. It is important to note that Raman scattering in both β-$MoTe_2$ and WTe_2 are sensitive to both the polarizations of the incident and scattered light [53]. Therefore, in order to elucidate the perceived emergence or disappearance of a particular peak, we plot in Figure 6.5 (right) the Raman spectra of β-$MoTe_2$ as a function of sample orientation while collecting the scattered light with polarization parallel to the incident light in the backscattering geometry.

Next we examine the Raman spectra of the alloyed materials in Figures 6.6. Figure 6.6 (left) shows the Raman spectra of several alloys whose compositions were measured using EDX prior to exfoliation. The compounds range from x=0 (top) to x=1 (bottom). The

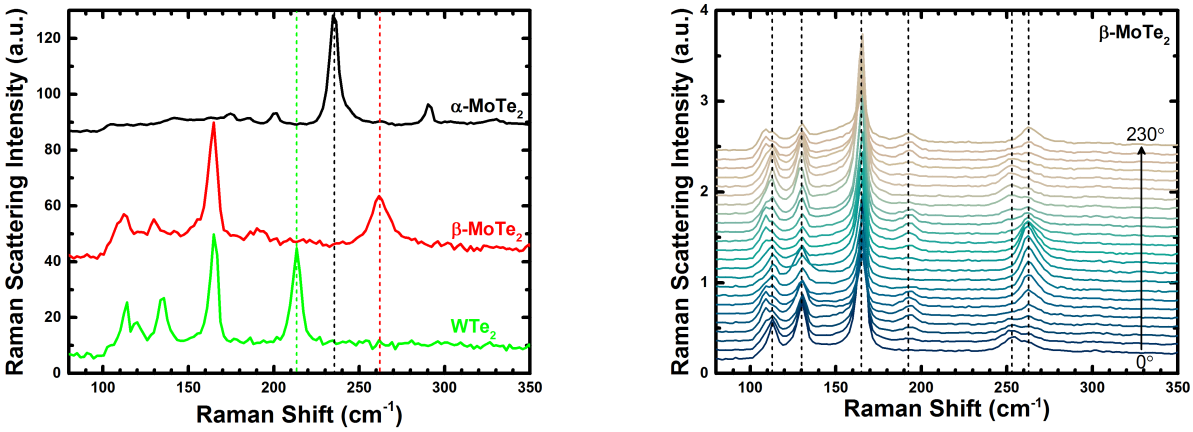

FIGURE 6.5. Raman spectra of WTe_2, β-$MoTe_2$, and α-$MoTe_2$ (left) and polarization-resolved spectra of β-$MoTe_2$ (right). Vertical dashed lines are guides to the eye.

spectra indicate that there is a transition from 2H to 1T" at a composition of approximately x=0.09. Additionally, we note that, at high tungsten concentration, the A_1 peak that is typically associated with WTe_2 begins to emerge (green dashed line). We also note that the lower frequency modes in the 100-170 cm^{-1} range gradually blue shift towards the positions normally found in WTe_2, likely indicative of the increased force constant associated with the transition metal-chalcogen bond. In order to rule out that this blue-shifting of the lower frequency modes is a mere coincidence, we perform layer dependent Raman on an alloy with x=0.12 (see Figure 6.6: right). We do not observe significant frequencies shifts in these lower frequency modes as a function of thickness. We do, however, observe a variation in the intensities of these modes with thickness. The cause of this warrants further study but it is likely due to degradation/oxidation of the thinnest layers [60].

6.4. Electrical Transport

Next, we sudy the electrical properties associated with the two different crystal structures exhibited by these alloys. Four-terminal resistivity measurements were performed on few-layer alloyed crystals of several different compositions. Devices were fabricated quickly,

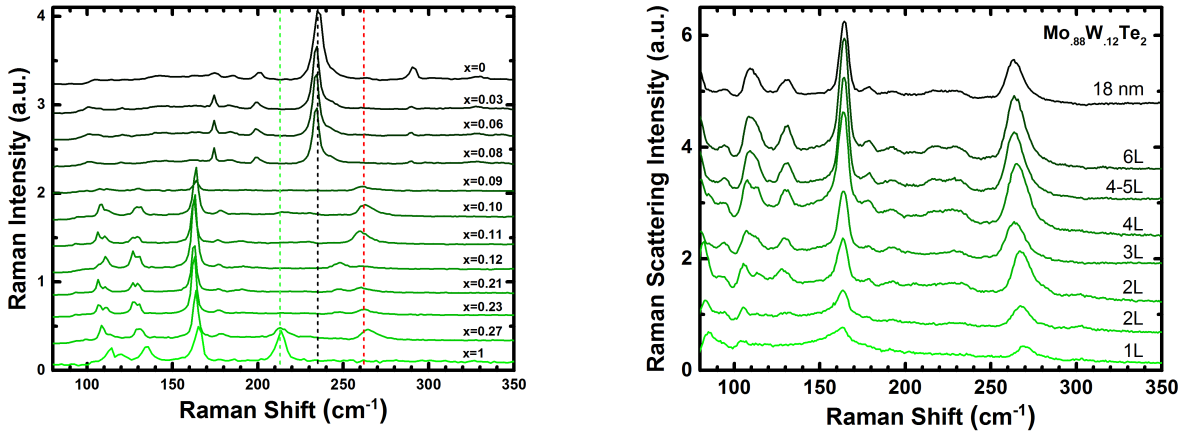

FIGURE 6.6. Raman scattering response of bulk $Mo_{1-x}W_xTe_2$ alloys as a function of composition (left) and Raman scattering response of $Mo_{.88}W_{.12}Te_2$ as a function of thickness (right).

minimizing exposure to ambient environment, and measured in a vacuum probe station using a semiconductor paramater analyzer. All devices exfoliated from crystals with low tungsten concentration showing 2H Raman scattering exhibited semiconducting behavior with on/off ratios at room temperature in the 10^3-10^5 range (see Figure 6.7a). Devices with high tungsten concentration exhibited no gate dependence (see cyan curve in Figure 6.7a). In Figure 6.7b, we plot the resistances at zero gate bias. Devices in the red region exhibited resistances on the order of 1 GΩ and all crystals in this composition range exhibited 2H Raman scattering. Devices in the purple compositional region came from batches that contained both 1T" and 2H crystals, although the flakes themselves were 2H and had resistances in the GΩ range. All devices measured in the blue region were 1T", exhibited no gate dependence, and had resistances on the order of 100 Ω. Clearly, as expected, there is a stark contrast between the electrical properties of 2H and 1T".

6.5. Raman Evolution with Joule Heating

We also develop a technique to study the phase transition in $Mo_{1-x}W_xTe_2$ alloys as a function of temperature using graphene/hexagonal boron nitride heterostructures. Fig-

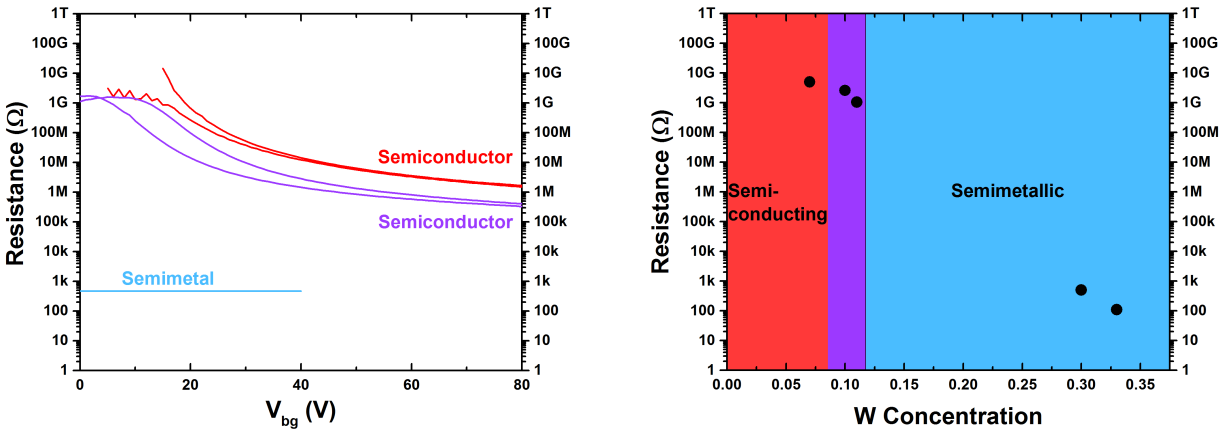

FIGURE 6.7. a) Transfer curve of transistors fabricated from few-layer $Mo_{1-x}W_xTe_2$ alloys. Red and purple curves are alloys that exhibited 2H Raman scattering. Cyan is a 1T" device that exhibited negligible gate dependence. b) Channel resistances as a function of molybdenum concentration were measured at $V_{bg} = 0$ V. The red shaded region represents stoichiometries confirmed by EDX that exhibited 2H Raman scattering. The purple region represents stoichiometries measured in EDX where we observe crystals with either 2H or 1T" Raman scattering. The blue region contained crystals where we only observe 1T" Raman scattering and semi-metallic electrical properties.

ures 6.8a and b show a cross-section schematic and optical image of an example device, respectively. We use dry transfer techniques to create an encapsulated device where we can use Joule heating through the graphene to raise the temperature of the $Mo_{1-x}W_xTe_2$ alloy. However, in the data to follow, we first attempt the phase change on pure α-$MoTe_2$. The graphene provides a semi-transparent heater through which we can still perform Raman spectroscopy. Moreover, it allows us to avoid potential alloying since typical refractory metals, such as molybdenum, tungsten, and tantalum, have a phase diagram with tellurium, whereas carbon does not. The heterostructure also allows us to avoid potential oxidation of the tellurium, after which all phase transitions would be irreversible.

Figure 6.8c shows the current vs. voltage curve for the graphene device on the left y-axis and electrical power vs. voltage on the right y-axis. The device exhibits ohmic behavior until the power generation reaches approximately 25 mW; at which point the conductivity

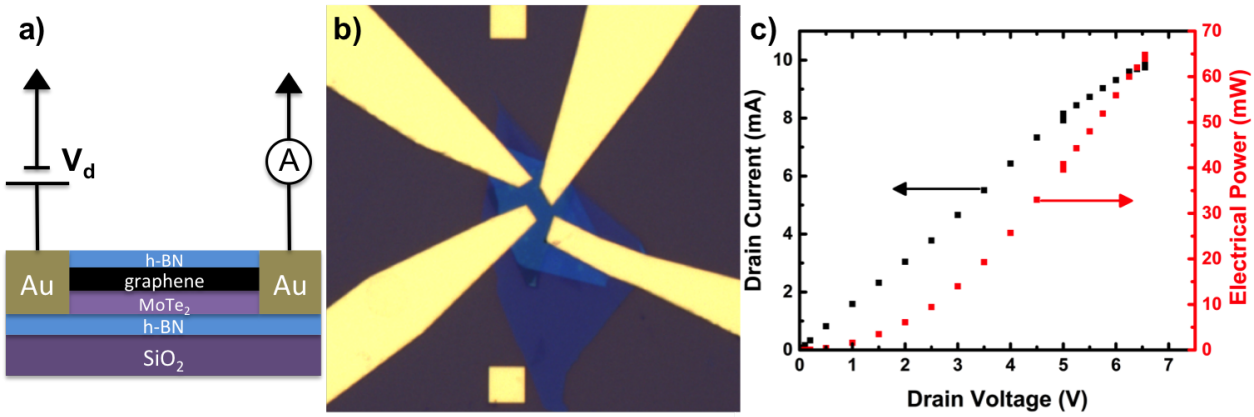

FIGURE 6.8. (a) Device schematic, (b) optical micrograph, and (c) I-V, P-V of graphene device.

of the graphene begins to decrease via a self-heating effect due to increased electron-phonon scattering. Figure 6.9 shows the Raman spectra of the $MoTe_2$, fitted peak positions of the E^1_{2g} mode in $MoTe_2$ and G peak in graphene, and the estimated temperature of both lattices as a function of power. The temperature is estimated based upon a linear coefficient relating phonon softening to $\triangle T$ that was calculated in a preliminary experiment. Raman spectra were taken at each applied power (voltage) with 1 min accumulation times after a 2 min settling time. Laser powers were kept below 200 μW in order to avoid heating induced by the laser.

Figure 6.9b shows that, over the range of the experiment, the graphene G peak shifts by almost 12 cm^{-1}. At approximately 45 mW of applied power, the G peak is no longer discernible due to the blackbody radiation overwhelming the detector in the range of the G peak. However, we still collect the $MoTe_2$ spectra. Figure 6.10 shows the $MoTe_2$ Raman spectra over the total range of applied powers from lowest (bottom) to highest (top). As the power is increase, we observe significant phonon softening in the in-plane E_{2g} mode. At an applied power of approximately 20 mW, the $MoTe_2$ is at an estimated 250^{o}C and the B_{2g} mode begins to split. This mode is Raman silent in monolayer and bulk and is only present in few-layer. The splitting and eventual disappearance of this mode may be indicative of the

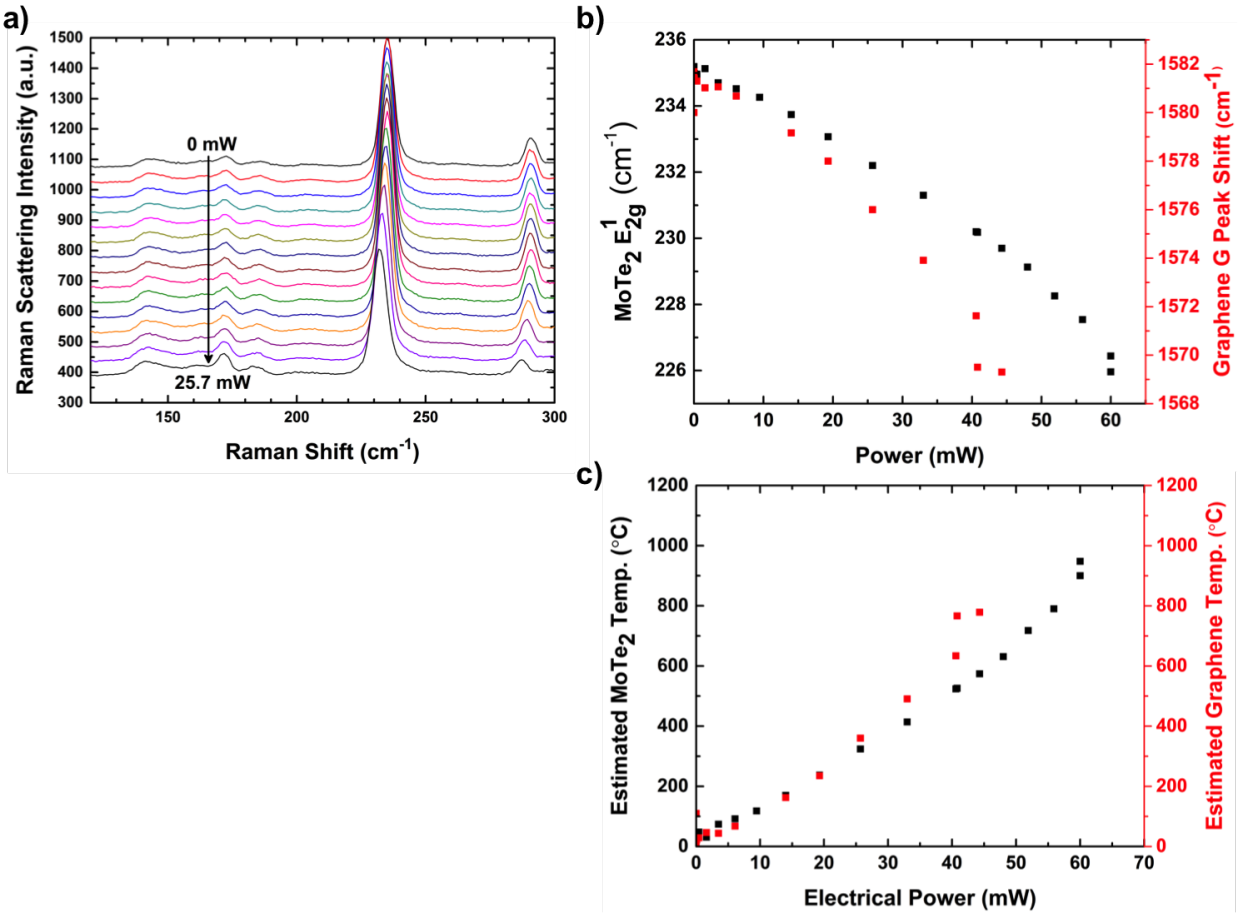

FIGURE 6.9. (a) $MoTe_2$ Raman spectra as a function of electrical power in the low power regime. (b) E_{2g} and G peak shifts of $MoTe_2$ and graphene, respectively, as a function of power. (c) Estimated temperature of $MoTe_2$ and graphene.

loss of interlayer registry in the few-layer $MoTe_2$. At 60 mW, the doubly-degenerate, in-plane E_{2g} mode splits into two weak and broad peaks. Two strong peaks at approximately 131 cm^{-1} and 151 cm^{-1} begin to merge at this high temperature phase. Their origin is, at this point, unknown; however, they appear to be related to the peak that is initially present at approximately 141 cm^{-1}. This mode was identified as a double resonance mode by Guo *et al.* in which they attributed it to a difference combination mode involving the E^1_{2g} and longitudinal acoustic (LA) modes at the M points [31]. Given that this mode follows the splitting of the E^1_{2g} mode, their assignment is likely correct.

In Figure 6.11, we plot the Raman spectra during the cooling process. Initally, it appears, from the high temperature Raman, that the material is being irreversibly broken down. However, upon slow cooling, the E_{2g} and B_{2g} modes re-emerge. It is possible that the observed peak splitting is indicative of an incomplete phase conversion; however, it is possible that it is mostly a signature of large in-plane strains due to different thermal expansion/contraction. However, given it's sudden appearance, further study is warranted.

6.6. Conclusions and Future Work

We successfully observed the phase change in $Mo_{1-x}W_xTe_2$ alloys driven by composition. We identified a narrow compositional range defining the phase boundary for as-grown crystals. Further, we characterized the optical and electrical properties of the different crystal stuctures exhibited by these alloys. Finally, we developed a device architecture to further study the phase dynamics in these materials. While we did not observe the phase change, it may be due to the kinetics associated with a phase change of pure α-$MoTe_2$. Typically, in bulk crystal growth, the relaxation from the high temperature phase β-$MoTe_2$ to α-$MoTe_2$ requires slow cooling over the course of tens to hundreds of hours. Additional experiments will be performed on the alloys as well as on β-$MoTe_2$, which should require a lower temperature to drive the phase transition.

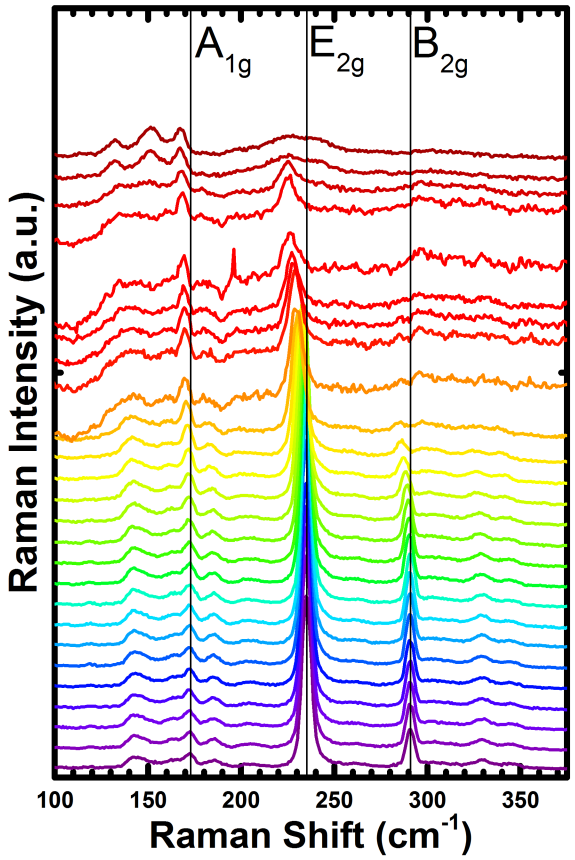

FIGURE 6.10. $MoTe_2$ Raman spectra throughout entire power range.

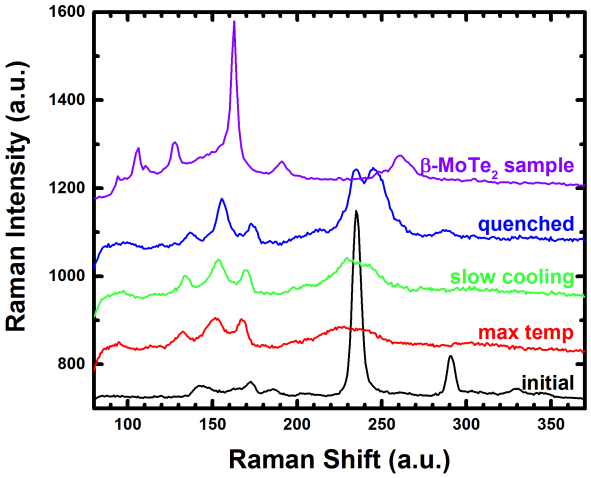

FIGURE 6.11. $MoTe_2$ Raman spectra in the initial (black), max-temperature (red), slow-cooled (green), and quenched (blue) states. β-$MoTe_2$ Raman spectra is plotted in purple.

CHAPTER 7

2D Semiconductor Optoelectronics

7.1. Background

Layered semiconductors, such as MoS_2, WS_2, and WSe_2, exhibit strong absorption over a broad spectrum and, thus, possess interesting potential in optoelectronic applications [70]. Many devices have been demonstrated with a photoresponse that is tunable by using a gate electrode to locally modulate the chemical potential in the active region of *in-plane* p-i-n diodes, Schottky diodes, and phototransistors [124, 130, 4, 93, 97, Fontana et al., 85]. Recently, there have also been reports of optoelectronic devices that exploit the *out-of-plane* transport properties in graphene/TMDC/graphene vertical heterostructures [83, 126, 6, 84]. These devices also require a gate electrode; however, in these cases, the gate electrode functions to modulate the chemical potential of one of the graphene electrodes in order to create a built-in field.

7.2. $MoTe_2$ Optoelectronics

Molybdenum ditelluride ($MoTe_2$) is a small (optical) bandgap (1.0 eV in the bulk; 1.1 eV in the monolayer) layered semiconductor [98]. It possesses similar properties to the other Group VI TMDCs, such as MoS_2, WSe_2, WS_2, and $MoSe_2$; namely large exciton and trion binding energies, large spin-orbit coupling, and an indirect to direct bandgap crossover when approaching the monolayer limit [99]. There are, however, two significant distinctions. The first is that it possesses a smaller bandgap, which expands the operable wavelength range. The second is that this material exhibits environmental stability issues; there have been several works demonstrating rapid degradation in air [11]. This unfortunate fact should not, however, preclude it from being thoroughly evaluated from an applications perspective.

Several recent works have demonstrated that encapsulation enables the preservation of other air-sensitive layered materials and surface passivation is an engineering challenge that has been solved in multiple material systems.

In addition to an optical bandgap that allows absorption throughout the entire visible spectrum and into the near infrared, $MoTe_2$ is expected to possess moderately high carrier mobilities as compared to its other Group VI TMDC counterparts. The electronic properties coupled with its low dimensionality, which is expected to lend itself to high mechanical flexibility, could enable its use in potentially flexible optoelectronic applications. Moreover, the synthesis and transfer processes that are distinct to 2D materials and have been developed in several other systems allows for the integration onto arbitrary substrates and into standard CMOS processes. In order to better study the potential of $MoTe_2$, we study both in-plane and out-of-plane heterostructures using hexagonal boron nitride (h-BN) as a dielectric and encapsulant and graphene as both the anode and cathode due to its benefits as a transparent contact whose work function can be modulated electrostatically or chemically.

7.2.1. In-plane Photodetectors. Figure 7.1 shows the architecture for a split-gate $MoTe_2$ p-i-n diode, a common architecture used in measuring the photovoltaic response in layered TMDCs and carbon nanotubes. In this structure, 20 nm thick Pd local gates (1 μm separation) were prefabricated on a silicon wafer with a 285 nm insulating SiO_2 epilayer using electron beam lithography. H-BN, 4-layer $MoTe_2$, graphene and a top h-BN were then deposited using sequential aligned dry transfers. Electrical contact to the device was achieved through a 1-dimensional edge contact to the graphene, which is used to make a low-resistance contact to the $MoTe_2$. In this device, fabrication was done in an ambient environment and complete encapsulation was achieved in less than 30 minutes in order to minimize any degradation to the $MoTe_2$.

Figure 7.1c shows the dark I-V curves with local gate 2 fixed at -3 V while stepping local gate 1 from +1.6 V to -1.6 V. Voltage limits were placed on both gates in order to avoid

breakdown in the h-BN dielectric. Rectification, as expected, occurs when the two local gates have opposite polarity. In order to map the generation of photocurrent as a function of position, we use piezo-controlled mirrors to raster a 600 nm laser spot (40x objective; NA=), while simultaneously measuring current generated under the zero bias condition. Figure 7.1d shows the photovoltaic response of the device in units of responsivity (mA/W). It is clear from the map that the response is narrowly confined within the junction defined by the two local gates.

Next we examine the photoresponse as a function of wavelength. Figure 7.2 (left) shows the I-V curves under 200 nW (measured at the objective) illumination of the junction as a function of wavelength from 450 nm to 675 nm. Figure 7.2 (right) shows the corresponding short circuit currents and open circuit voltages. The device shows a peak response at a photon energy of around 1.9 eV. This peak corresponds with a direct optical transition labeled as the A' peak in the absorption spectra measured by Ruppert *et al.* [98].

Figures 7.3 a) through c) show the I-V curves under illumination by 500 nm, 600 nm, and 725 nm light, respectively, as a function of incident power. Figures 7.3d shows the corresponding short circuit current and open circuit voltages. It can be seen that the short circuit current begins to saturate at an incident power of approximately 2 μW. This could, perhaps, be attributed to saturable absorption caused by increased carrier-carrier and carrier-phonon interactions that limit the overall efficiency at high power densities. This effect has been observed in other TMDC photodetectors, albeit at much higher power densities. It could also be a result of local heating caused by absorption of the Pd local gates. In Figure 7.4, we plot the external quantum efficiency (EQE) of the device as a function of power and wavelength. The device exhibits a peak EQE at roughly 5.3% for 600 nm at 100 nW. This is comparable to devices reported with similar architectures with other TMDCs; however, it is likely far too low to be technologically relevant. This, in addition to the inherent fabrication challenges and small device active area, probably preclude this architecture from industrial applications.

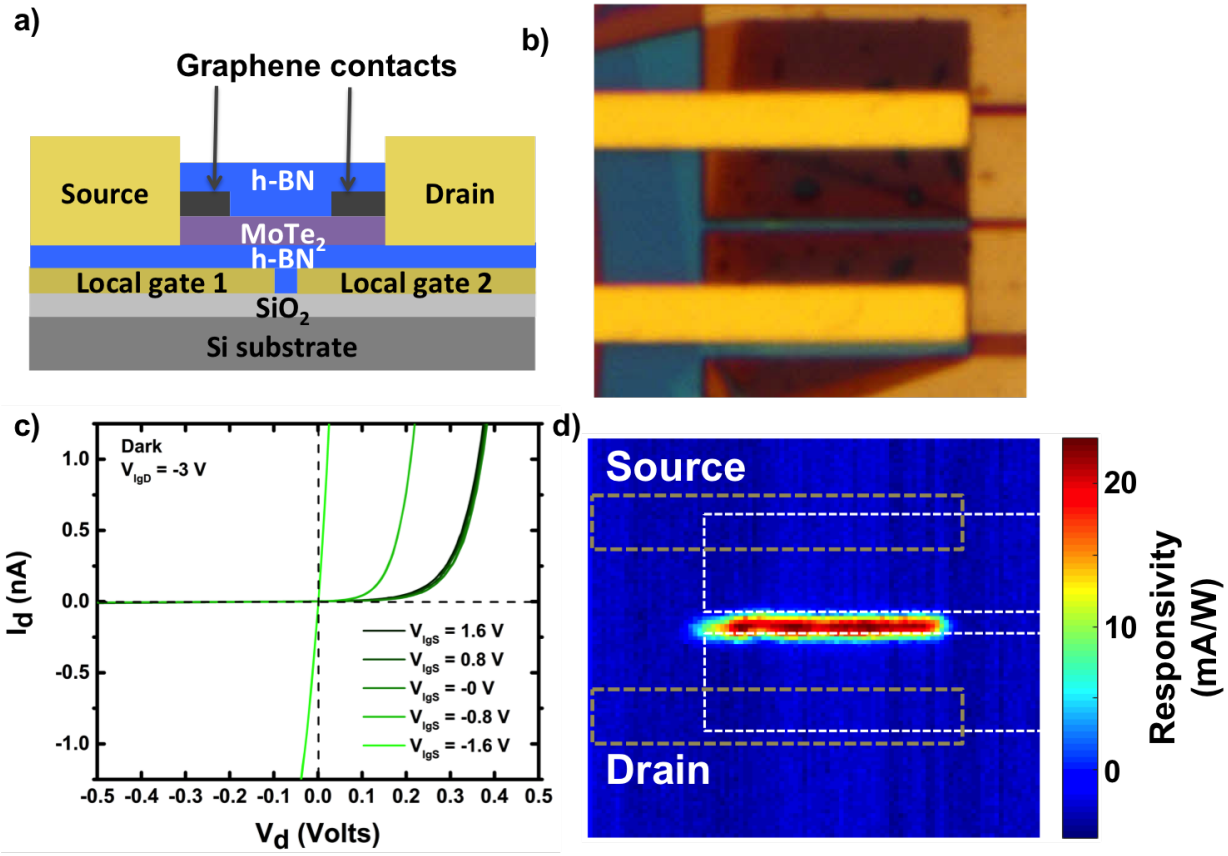

FIGURE 7.1. Device architecture for split-gate p-i-n diode. a) Schematic of the device. b) Optical image of the device. $MoTe_2$ was 4 layers thick, graphene was approximately 4 layers thick, and the bottom and top h-BN layers were approximately 20 nm and 15 nm, respectively. c) Dark IV characteristics. The local gate next to the drain is fixed at -3 V while the local gate next to the source electrode is stepped from +1.6 to -1.6 V. d) Photocurrent map displaying the device responsivity (measured at 0V bias) under illumination by a 600 nm laser spot through a 40x objective (NA=0.6) with a power of 200 nW (measured at the objective).

7.2.2. Out-of-plane Photodetectors. We next characterize the performance of out-of-plane (vertical) photodetectors. Figure 7.5a shows an optical micrograph of a vertical device fabricated by all dry transfer techniques (see Figure 7.5b for cross-section schematic). Once again, in order to avoid degradation of the $MoTe_2$, complete encapsulation was achieved within 30 minutes after exfoliation. The exfoliation of graphene onto SiO_2 is expected to produced moderate p-doping. Figure 7.5c shows the transfer curve of both the bottom

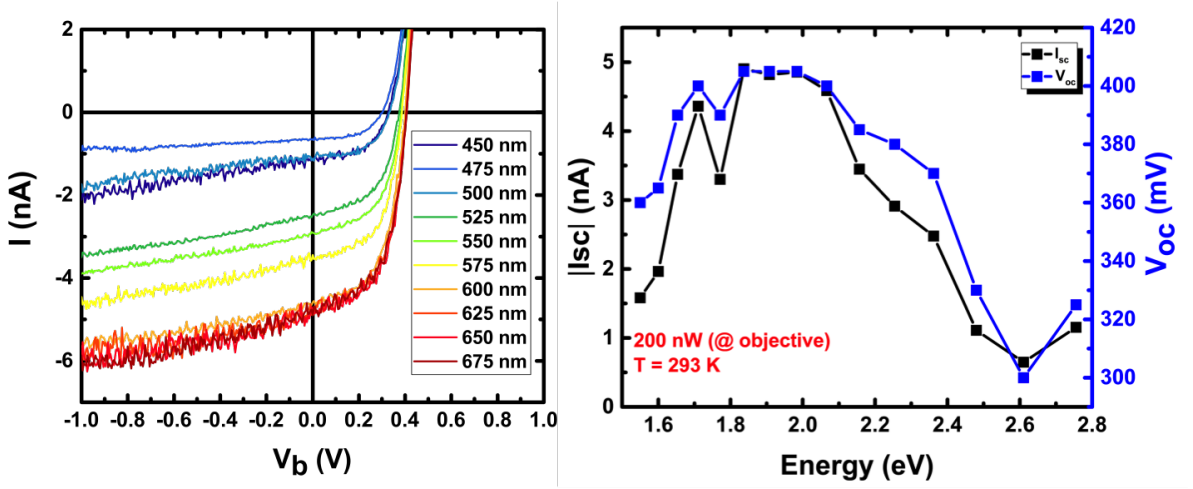

FIGURE 7.2. Photoresponse at a constant 200 nW through a 10x objective with laser spot center over the junction. (left) I-V curves as a function of wavelength. Left) I-V curves as a function of wavelength. Right) Short circuit current and open circuit voltage as a function of photon energy. The graph shows a peak response at an energy of ~1.9 eV.

graphene by itself (blue curve) and through the vertical device (red). The blue curve is typical of p-doped graphene with a charge neutrality point at V_{bg} = 50 V. The red curve displays 2 peaks in the resistance. It is expected that the bottom graphene only partially screens the electric field created by the gate bias. Therefore, the peak in resistance at V_{bg} = 0 V is likely due to a convolution of the very lightly-doped $MoTe_2$and top graphene, while the peak at positive gate bias can be attributed to the bottom p-doped graphene.

Next, we examine the photoresponse of the device by mapping the short circuit current as a function of backgate voltage under 633 nm illumination. Figure 7.6b shows the short circuit current maps as a function of V_{bg}. It can be seen that the device produces a substantial photoresponse even in the absence of an applied gate bias, owing to the efficacy of the moderate p-doping induced by the substrate. The responsivity increases from approximately -100 mA/W at V_{bg} = 0 V to -200 mA/W at V_{bg} = -60 V. Once V_{bg} reaches 40-50 V, and the bottom graphene reaches its charge neutrality point, the photoresponse decreases to zero and then changes sign with higher positive gate voltages. This can also be observed in Figure

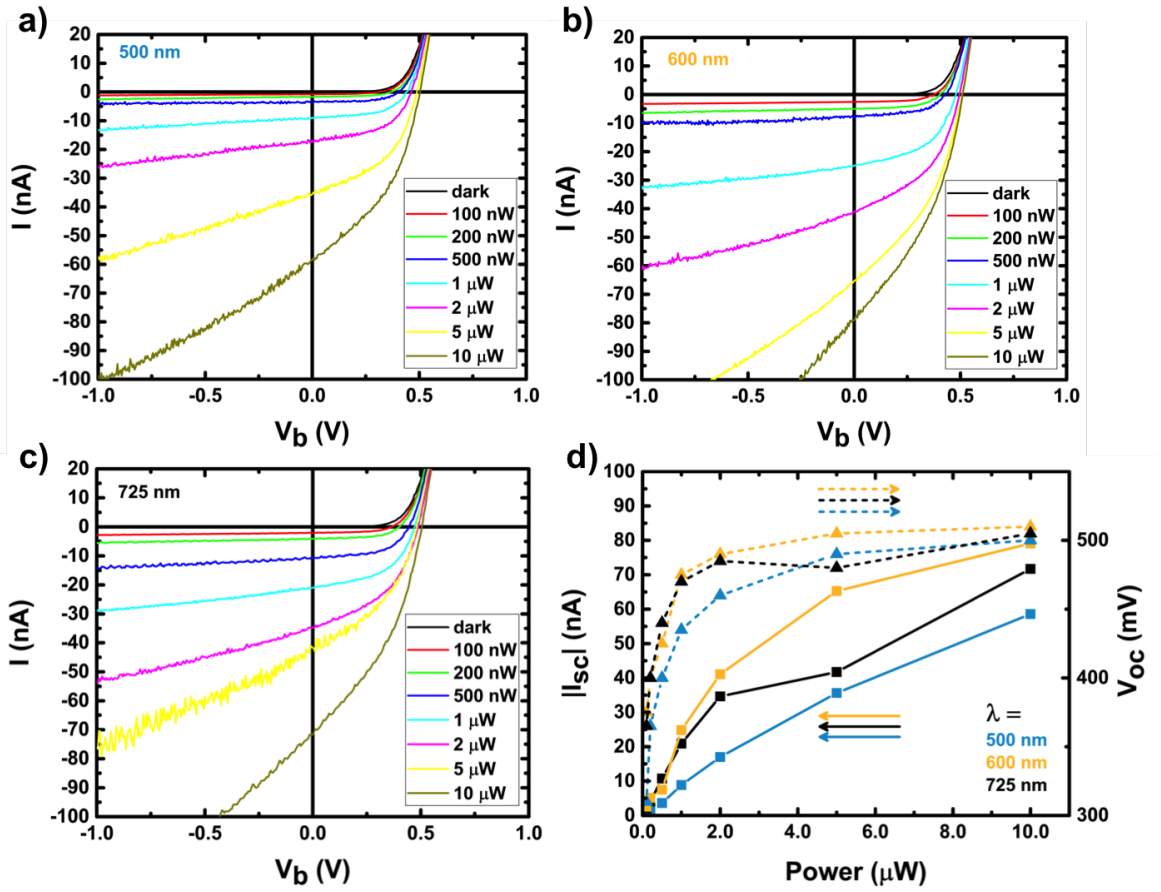

FIGURE 7.3. a) IV curve under illumination as a function of power for $\lambda = 500$ nm. b) IV curve under illumination as a function of power for $\lambda = 600$ nm. c) IV curve under illumination as a function of power for $\lambda = 725$ nm. d) Short circuit currents and open circuit voltages as a function of power and wavelength.

7.6c where the normalized short circuit current (black triangles) crosses through the right y-axis when the bottom graphene is at the charge neutrality point.

Next we examine the performance of the device as a function of incident power. Figure 7.7 shows that the short circuit current is linear throughout the entire range measured up to 5 μW. Moreover, the device possesses a significantly higher external quantum efficiency than observed in the in-plane device.

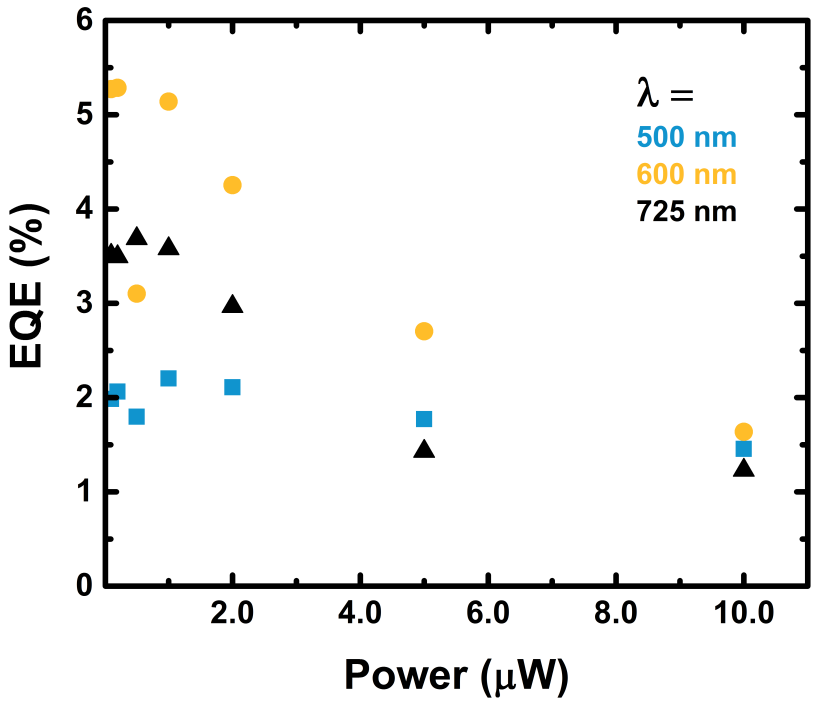

FIGURE 7.4. External quantum efficiency as a function of power and wavelength.

7.2.3. Conclusion and Future Work. We have demonstrated both in-plane and out-of-plane photodetectors in encapsulated $MoTe_2$. Furthermore, we have demonstrated that out-of-plane photodetectors can exhibit significantly higher external quantum efficiencies. There are, however, many aspects that remain unexplored and should be characterized, such as thickness dependence, intrinsic speed, and more controllable and permanent methods of doping graphene contacts in order to create the asymmetry required for operation of vertical TMDC photodetectors. In order to pursue high speed operation, devices that do not require a gate are highly-desired so as to limit parasitics and reduce the RC time constant. Additionally, while this vertical architecture has now been demonstrated in $MoTe_2$, a more technologically relevant material would be black phosphorus due to its low bandgap and potential operation at telecom wavelengths.

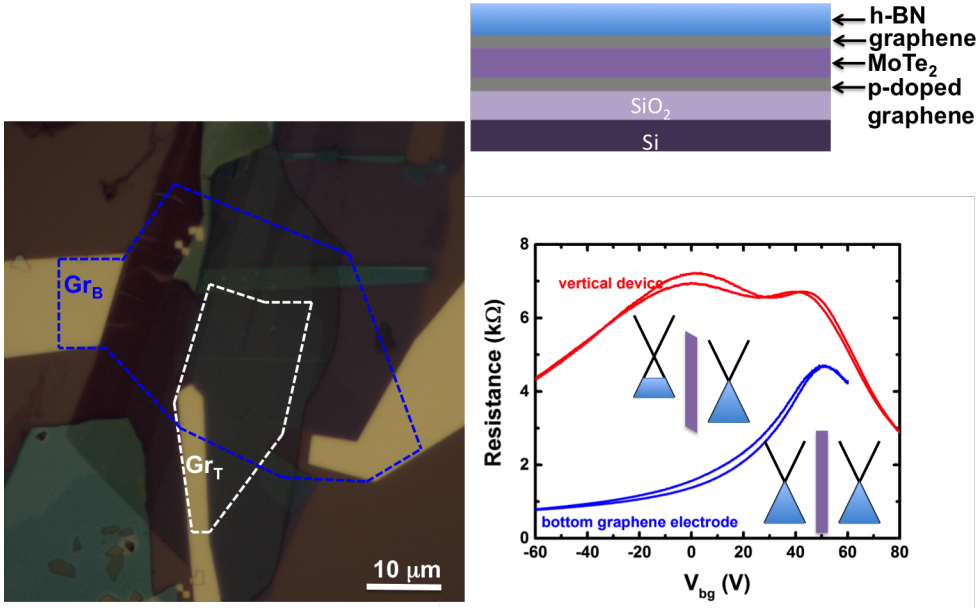

FIGURE 7.5. Vertical $Gr_B/MoTe_2/Gr_T$/h-BN photodetector architecture. a) Optical micrograph of device. The bottom graphene is outlined in blue and the top graphene is outlined in white. The active device area is defined by the overlap region between the two. b) Cross-section schematic of the device. c) Resistance vs. backgate voltage curve for just the bottom graphene (blue) and measuring between both graphene through the $MoTe_2$ (red).

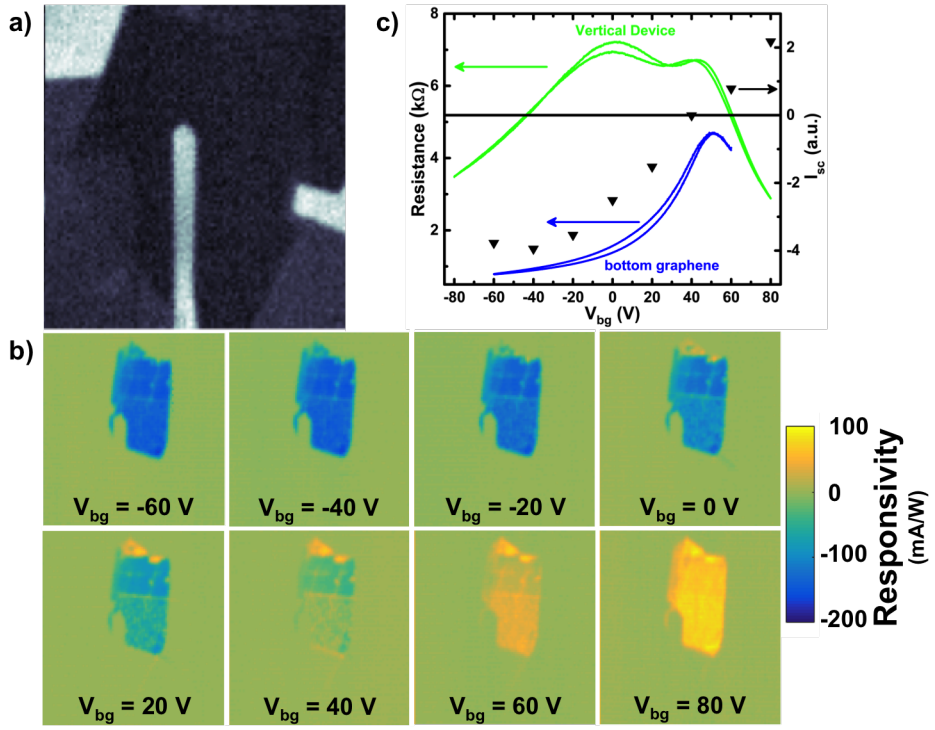

FIGURE 7.6. Photocurrent maps under 633 nm illumination on the vertical $MoTe_2$ device. a) Reflection image collected by silicon diode at same time of photocurrent map. b) Transfer curve (left y-axis) of bottom graphene (blue curve) and vertical device (green curve) collected while sweeping the backgate. Right y-axis shows the short circuit current collected at several backgate voltages (black triangles). c) Several photocurrent maps showing the responsivity of the device as a function of the backgate voltage.

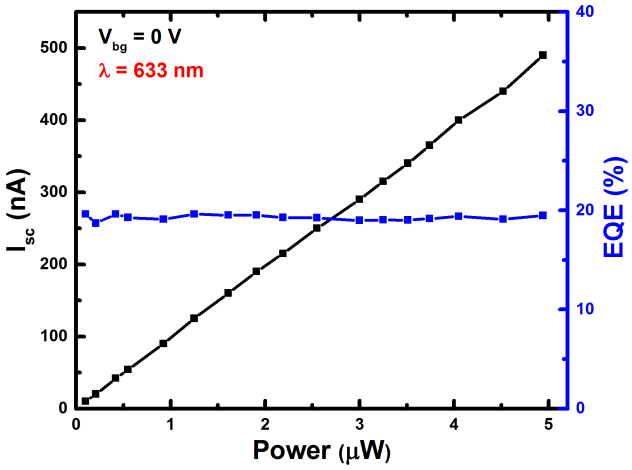

FIGURE 7.7. Short circuit current (black) and EQE (blue) as a function of power under 633 nm illumination and $V_{bg} = 0$ V.

Bibliography

[1] Deji Akinwande, Nicholas Petrone, and James Hone. Two-dimensional flexible nanoelectronics. *Nature Communications*, 5:5678, December 2014.

[2] Ozgur Burak Aslan, Daniel A Chenet, Arend M van der Zande, James C Hone, and Tony F Heinz. Linearly Polarized Excitons in Single- and Few-Layer ReS2 Crystals. *ACS Photonics*, 3(1):96–101, December 2015.

[3] A Avsar, J Y Tan, T Taychatanapat, J Balakrishnan, G K W Koon, Y Yeo, J Lahiri, A Carvalho, A S Rodin, E C T O'Farrell, G Eda, A H Castro Neto, and B Özyilmaz. Spin–orbit proximity effect in graphene. *Nature Communications*, 5:4875, September 2014.

[4] Britton W H Baugher, Hugh O H Churchill, Yafang Yang, and Pablo Jarillo-Herrero. Optoelectronic devices based on electrically tunable p-n diodes in a monolayer dichalcogenide. *Nature nanotechnology*, 9(4):262–267, April 2014.

[5] L Britnell, R V Gorbachev, R Jalil, B D Belle, F Schedin, A Mishchenko, T Georgiou, M I Katsnelson, L Eaves, S V Morozov, N M R Peres, J Leist, A K Geim, K S Novoselov, and L A Ponomarenko. Field-Effect Tunneling Transistor Based on Vertical Graphene Heterostructures. *Science*, 335(6071):947–950, February 2012.

[6] L Britnell, R M Ribeiro, A Eckmann, R Jalil, B D Belle, A Mishchenko, Y J Kim, R V Gorbachev, T Georgiou, S V Morozov, A N Grigorenko, A K Geim, C Casiraghi, A H Castro Neto, and K S Novoselov. Strong Light-Matter Interactions in Heterostructures of Atomically Thin Films. *Science*, 340(6138):1311–1314, June 2013.

[7] Jacopo Brivio, Duncan T L Alexander, and Andras Kis. Ripples and Layers in Ultrathin MoS2 Membranes. *Nano Letters*, 11(12):5148–5153, October 2011.

[8] Lola Brown, Robert Hovden, Pinshane Huang, Michal Wojcik, David A Muller, and Jiwoong Park. Twinning and Twisting of Tri- and Bilayer Graphene. *Nano Letters*, 12 (3):1609–1615, February 2012.

[9] Michele Buscema, Dirk J Groenendijk, Gary A Steele, Herre S J van der Zant, and Andres Castellanos-Gomez. Photovoltaic effect in few-layer black phosphorus PN junctions defined by local electrostatic gating. *Nature Communications*, 5:4651, August 2014.

[10] Line S Byskov, Jens K Nørskov, Bjerne S Clausen, and Henrik Topsøe. Edge termination of MoS2 and CoMoS catalyst particles. *Catalysis letters*, 64(2-4):95–99, 2000.

[11] Bin Chen, Hasan Sahin, Aslihan Suslu, Laura Ding, Mariana I Bertoni, F M Peeters, and Sefaattin Tongay. Environmental Changes in MoTe2 Excitonic Dynamics by Defects-Activated Molecular Interaction. *ACS Nano*, 9(5):5326–5332, April 2015.

[12] Daniel A Chenet, O Burak Aslan, Pinshane Y Huang, Chris Fan, Arend M van der Zande, Tony F Heinz, and James C Hone. In-Plane Anisotropy in Mono- and Few-Layer ReS2 Probed by Raman Spectroscopy and Scanning Transmission Electron Microscopy. *Nano Letters*, 15(9):5667–5672, August 2015.

[13] Manish Chhowalla, Hyeon Suk Shin, Goki Eda, Lain-Jong Li, Kian Ping Loh, and Hua Zhang. The chemistry of two-dimensional layered transition metal dichalcogenide nanosheets. *Nature Chemistry*, 5(4):263–275, April 2013.

[14] Hiram J Conley, Bin Wang, Jed I Ziegler, Jr Richard F Haglund, Sokrates T Pantelides, and Kirill I Bolotin. Bandgap Engineering of Strained Monolayer and Bilayer MoS2. *Nano Letters*, 13(8):3626–3630, July 2013.

[15] Chris M Corbet, Connor McClellan, Amritesh Rai, Sushant Sudam Sonde, Emanuel Tutuc, and Sanjay K Banerjee. Field Effect Transistors with Current Saturation and Voltage Gain in Ultrathin ReS2. *ACS Nano*, page 141224131942008, December 2014.

[16] Saptarshi Das, Hong-Yan Chen, Ashish Verma Penumatcha, and Joerg Appenzeller. High Performance Multilayer MoS2 Transistors with Scandium Contacts. *Nano Letters*, 13(1):100–105, December 2012.

[17] C R Dean, A F Young, I Meric, C Lee, L Wang, S Sorgenfrei, K Watanabe, T Taniguchi, P Kim, K L Shepard, and J Hone. Boron nitride substrates for high-quality graphene

electronics. *Nature nanotechnology*, 5(10):722–726, October 2010.

[18] Rostislav A Doganov, Eoin C T O'Farrell, Steven P Koenig, Yuting Yeo, Angelo Ziletti, Alexandra Carvalho, David K Campbell, David F Coker, Kenji Watanabe, Takashi Taniguchi, Antonio H Castro Neto, and Barbaros Özyilmaz. Transport properties of pristine few-layer black phosphorus by van der Waals passivation in an inert atmosphere. *Nature Communications*, 6:6647, April 2015.

[19] Karel-Alexander N Duerloo and Evan J Reed. Structural Phase Transitions by Design in Monolayer Alloys. *ACS Nano*, 10(1):289–297, December 2015.

[20] Karel-Alexander N Duerloo, Mitchell T Ong, and Evan J Reed. Intrinsic Piezoelectricity in Two-Dimensional Materials. *The Journal of Physical Chemistry Letters*, 3(19): 2871–2876, September 2012.

[21] Karel-Alexander N Duerloo, Yao Li, and Evan J Reed. Structural phase transitions in two-dimensional Mo- and W-dichalcogenide monolayers. *Nature Communications*, 5, July 2014.

[22] D O Dumcenco, Y S Huang, C H Liang, and K K Tiong. Optical characterization of niobium-doped rhenium disulphide single crystals. *Journal of Applied Physics*, 102(8): 083523, 2007.

[23] Goki Eda, Takeshi Fujita, Hisato Yamaguchi, Damien Voiry, Mingwei Chen, and Manish Chhowalla. Coherent Atomic and Electronic Heterostructures of Single-Layer MoS2. *ACS Nano*, 6(8):7311–7317, July 2012.

[24] C M Fang, G A Wiegers, C Haas, and R A de Groot. Electronic structures of , and in the real and the hypothetical undistorted structures. *Journal of Physics: Condensed Matter*, 9(21):4411–4424, May 1997.

[25] Qingliang Feng, Nannan Mao, Juanxia Wu, Hua Xu, Chunming Wang, Jin Zhang, and Liming Xie. Growth of MoS2(1–x)Se2x (x = 0.41–1.00) Monolayer Alloys with Controlled Morphology by Physical Vapor Deposition. *ACS Nano*, 9(7):7450–7455, June 2015.

[Fontana et al.] M Fontana, T Deppe, A K Boyd, M Rinzan, and A Y Liu. Photovoltaic effect in gated MoS2 Schottky junctions.

[26] K Friemelt, M Ch Lux-Steiner, and E Bucher. Optical properties of the layered transition-metal-dichalcogenide ReS2: Anisotropy in the van der Waals plane. *Journal of Applied Physics*, 74(8):5266, 1993.

[27] Guillaume Froehlicher, Etienne Lorchat, François Fernique, Chaitanya Joshi, Alejandro Molina-Sánchez, Ludger Wirtz, and Stéphane Berciaud. Unified Description of the Optical Phonon Modes in N-Layer MoTe2. *Nano Letters*, 15(10):6481–6489, September 2015.

[28] Anand P S Gaur, Satyaprakash Sahoo, J F Scott, and Ram S Katiyar. Electron–Phonon Interaction and Double-Resonance Raman Studies in Monolayer WS2. *The Journal of Physical Chemistry C*, 119(9):5146–5151, February 2015.

[29] Paolo Giannozzi, Stefano Baroni, Nicola Bonini, Matteo Calandra, Roberto Car, Carlo Cavazzoni, Davide Ceresoli, Guido L Chiarotti, Matteo Cococcioni, Ismaila Dabo, Andrea Dal Corso, Stefano de Gironcoli, Stefano Fabris, Guido Fratesi, Ralph Gebauer, Uwe Gerstmann, Christos Gougoussis, Anton Kokalj, Michele Lazzeri, Layla Martin-Samos, Nicola Marzari, Francesco Mauri, Riccardo Mazzarello, Stefano Paolini, Alfredo Pasquarello, Lorenzo Paulatto, Carlo Sbraccia, Sandro Scandolo, Gabriele Sclauzero, Ari P Seitsonen, Alexander Smogunov, Paolo Umari, and Renata M Wentzcovitch. QUANTUM ESPRESSO: a modular and open-source software project for quantum simulations of materials. *Journal of Physics: Condensed Matter*, 21(39):395502, September 2009.

[30] Yongji Gong, Junhao Lin, Xingli Wang, Gang Shi, Sidong Lei, Zhong Lin, Xiaolong Zou, Gonglan Ye, Robert Vajtai, Boris I Yakobson, Humberto Terrones, Mauricio Terrones, Beng Kang Tay, Jun Lou, Sokrates T Pantelides, Zheng Liu, Wu Zhou, and Pulickel M Ajayan. Vertical and in-plane heterostructures from WS2/MoS2 monolayers. *Nature materials*, 13(12):1135–1142, December 2014.

[31] Huaihong Guo, Teng Yang, Mahito Yamamoto, Lin Zhou, Ryo Ishikawa, Keiji Ueno, Kazuhito Tsukagoshi, Zhidong Zhang, Mildred S Dresselhaus, and Riichiro Saito. Double resonance Raman modes in monolayer and few-layer MoTe2. *Physical Review B*, 91(20):205415, May 2015.

[32] Humberto R Gutiérrez, Nestor Perea-López, Ana Laura Elías, Ayse Berkdemir, Bei Wang, Ruitao Lv, Florentino López-Urías, Vincent H Crespi, Humberto Terrones, and Mauricio Terrones. Extraordinary Room-Temperature Photoluminescence in Triangular WS2 Monolayers. *Nano Letters*, 13(8):3447–3454, December 2012.

[33] P B Hirsch, A Howie, R B Nicholson, and D W Pashley. *Electron microscopy of thin crystals*. 1965, 1966.

[34] C H Ho and C E Huang. Optical property of the near band-edge transitions in rhenium disulfide and diselenide. *Journal of alloys and compounds*, 383(1-2):74–79, November 2004.

[35] C H Ho, Y S Huang, K K Tiong, and P C Liao. In-plane anisotropy of the optical and electrical properties of layered ReS2 crystals. *Journal of Physics: Condensed Matter*, 11(27):5367–5375, July 1999.

[36] Ching-Hwa Ho. Dichroic Electro-Optical Behavior of Rhenium Sulfide Layered Crystal. *Crystal Structure Theory and Applications*, 02(02):65–69, June 2013.

[37] Tu Hong, Bhim Chamlagain, Wenzhi Lin, Hsun-Jen Chuang, Minghu Pan, Zhixian Zhou, and Ya-Qiong Xu. Polarized photocurrent response in black phosphorus field-effect transistors. *Nanoscale*, 2014.

[38] J M Howe. Interfaces in materials: atomic structure, thermodynamics and kinetics of solid-vapor, solid-liquid and solid-solid interfaces, 1997.

[39] Jing-Kai Huang, Jiang Pu, Chang-Lung Hsu, Ming-Hui Chiu, Zhen-Yu Juang, Yung-Huang Chang, Wen-Hao Chang, Yoshihiro Iwasa, Taishi Takenobu, and Lain-Jong Li. Large-Area Synthesis of Highly Crystalline WSe2 Monolayers and Device Applications. *ACS Nano*, 8(1):923–930, December 2013.

[40] Mingyuan Huang, Hugen Yan, Tony F Heinz, and James Hone. Probing Strain-Induced Electronic Structure Change in Graphene by Raman Spectroscopy. *Nano Letters*, 10 (10):4074–4079, August 2010.

[41] Pinshane Y Huang, Carlos S Ruiz-Vargas, Arend M van der Zande, William S Whitney, Mark P Levendorf, Joshua W Kevek, Shivank Garg, Jonathan S Alden, Caleb J Hustedt, Ye Zhu, Jiwoong Park, Paul L McEuen, and David A Muller. Grains and grain boundaries in single-layer graphene atomic patchwork quilts. *Nature*, 469(7330): 389–392, January 2011.

[42] Pinshane Y Huang, Jannik C Meyer, and David A Muller. From atoms to grains: Transmission electron microscopy of graphene. *MRS bulletin*, 37(12):1214–1221, December 2012.

[43] Y C Jiang, J Gao, and L Wang. Raman fingerprint for semi-metal WTe2 evolving from bulk to monolayer. *Scientific reports*, 6:19624, January 2016.

[44] Wencan Jin, Po-Chun Yeh, Nader Zaki, Datong Zhang, Jerzy T Sadowski, Abdullah Al-Mahboob, Arend M van der Zande, Daniel A Chenet, Jerry I Dadap, Irving P Herman, Peter Sutter, James Hone, and Jr Richard M Osgood. Direct Measurement of the Thickness-Dependent Electronic Band Structure of MoS2 Using Angle-Resolved Photoemission Spectroscopy. *Physical Review Letters*, 111(10):106801, September 2013.

[45] A M Jones, H Yu, N J Ghimire, S Wu, and G Aivazian. Optical generation of excitonic valley coherence in monolayer WSe2. *Nature*, 2013.

[46] Dong Hoon Keum, Suyeon Cho, Jung Ho Kim, Duk-Hyun Choe, Ha-Jun Sung, Min Kan, Haeyong Kang, Jae-Yeol Hwang, Sung Wng Kim, Heejun Yang, K J Chang, and Young Hee Lee. Bandgap opening in few-layered monoclinic MoTe2. *Nature Physics*, 11(6):482–486, June 2015.

[47] Kwanpyo Kim, Zonghoon Lee, William Regan, C Kisielowski, M F Crommie, and A Zettl. Grain Boundary Mapping in Polycrystalline Graphene. *ACS Nano*, 5(3): 2142–2146, January 2011.

[48] G Kioseoglou, A T Hanbicki, M Currie, A L Friedman, D Gunlycke, and B T Jonker. Valley polarization and intervalley scattering in monolayer MoS2. *Applied Physics Letters*, 101(22):221907, November 2012.

[49] C Kittel. Introduction to solid state physics, 2005.

[50] Velveth Klee, Edwin Preciado, David Barroso, Ariana E Nguyen, Chris Lee, Kristopher J Erickson, Mark Triplett, Brandon Davis, I-Hsi Lu, Sarah Bobek, Jessica McKinley, Joseph P Martinez, John Mann, A Alec Talin, Ludwig Bartels, and François Léonard. Superlinear Composition-Dependent Photocurrent in CVD-Grown Monolayer MoS2(1–x)Se2x Alloy Devices. *Nano Letters*, 15(4):2612–2619, March 2015.

[51] C F Klingshirn. Semiconductor optics, 2012.

[52] Yu Kobayashi, Shohei Mori, Yutaka Maniwa, and Yasumitsu Miyata. Bandgap-tunable lateral and vertical heterostructures based on monolayer Mo1-x W x S2 alloys. *Nano Research*, 8(10):3261–3271, 2015.

[53] W D Kong, S F Wu, P Richard, C S Lian, J T Wang, C L Yang, Y G Shi, and H Ding. Raman scattering investigation of large positive magnetoresistance material WTe2. *Applied Physics Letters*, 106(8):081906, February 2015.

[54] Ondrej L Krivanek, Matthew F Chisholm, Valeria Nicolosi, Timothy J Pennycook, George J Corbin, Niklas Dellby, Matthew F Murfitt, Christopher S Own, Zoltan S Szilagyi, Mark P Oxley, Sokrates T Pantelides, and Stephen J Pennycook. Atom-by-atom structural and chemical analysis by annular dark-field electron microscopy. *Nature*, 464(7288):571–574, March 2010.

[55] Jayeeta Lahiri, You Lin, Pinar Bozkurt, Ivan I Oleynik, and Matthias Batzill. An extended defect in graphene as a metallic wire. *Nature nanotechnology*, 5(5):326–329, May 2010.

[56] D J Late, B Liu, HSSR Matte, V P Dravid, and CNR Rao. Hysteresis in single-layer MoS2 field effect transistors. *ACS Nano*, 2012.

[57] J V Lauritsen, J Kibsgaard, S Helveg, and H Topsøe. Size-dependent structure of MoS2 nanocrystals. *Nature*, 2007.

[58] Changgu Lee, Xiaoding Wei, Jeffrey W Kysar, and James Hone. Measurement of the Elastic Properties and Intrinsic Strength of Monolayer Graphene. *Science*, 321(5887): 385–388, July 2008.

[59] Changgu Lee, Hugen Yan, Louis E Brus, Tony F Heinz, James Hone, and Sunmin Ryu. Anomalous Lattice Vibrations of Single- and Few-Layer MoS2. *ACS Nano*, 4(5): 2695–2700, April 2010.

[60] Chia-Hui Lee, Eduardo Cruz Silva, Lazaro Calderin, Minh An T Nguyen, Matthew J Hollander, Brian Bersch, Thomas E Mallouk, and Joshua A Robinson. Tungsten Ditelluride: a layered semimetal. *Scientific reports*, 5:10013, June 2015.

[61] Gwan-Hyoung Lee, Ryan C Cooper, Sung Joo An, Sunwoo Lee, Arend van der Zande, Nicholas Petrone, Alexandra G Hammerberg, Changgu Lee, Bryan Crawford, Warren Oliver, Jeffrey W Kysar, and James Hone. High-Strength Chemical-Vapor–Deposited Graphene and Grain Boundaries. *Science*, 340(6136):1073–1076, May 2013.

[62] Gwan-Hyoung Lee, Young-Jun Yu, Xu Cui, Nicholas Petrone, Chul-Ho Lee, Min Sup Choi, Dae-Yeong Lee, Changgu Lee, Won Jong Yoo, Kenji Watanabe, Takashi Taniguchi, Colin Nuckolls, Philip Kim, and James Hone. Flexible and Transparent MoS2 Field-Effect Transistors on Hexagonal Boron Nitride-Graphene Heterostructures. *ACS Nano*, 7(9):7931–7936, August 2013.

[63] Gwan-Hyoung Lee, Xu Cui, Young Duck Kim, Ghidewon Arefe, Xian Zhang, Chul-Ho Lee, Fan Ye, Kenji Watanabe, Takashi Taniguchi, Philip Kim, and James Hone. Highly Stable, Dual-Gated MoS2 Transistors Encapsulated by Hexagonal Boron Nitride with Gate-Controllable Contact, Resistance, and Threshold Voltage. *ACS Nano*, 9(7):7019–7026, June 2015.

[64] Jaesung Lee, Zenghui Wang, Keliang He, Jie Shan, and Philip X L Feng. High Frequency MoS2 Nanomechanical Resonators. *ACS Nano*, 7(7):6086–6091, June 2013.

[65] Jieun Lee, Kin Fai Mak, and Jie Shan. Electrical control of the valley Hall effect in bilayer MoS2 transistors. *ArXiV*, August 2015.

[66] Yi Hsien Lee, Xin Quan Zhang, Wenjing Zhang, Mu Tung Chang, Cheng Te Lin, Kai Di Chang, Ya Chu Yu, Jacob Tse Wei Wang, Chia Seng Chang, Lain-Jong Li, and Tsung Wu Lin. Synthesis of Large-Area MoS2 Atomic Layers with Chemical Vapor Deposition. *Advanced Materials*, 24(17):2320–2325, May 2012.

[67] Honglai Li, Xidong Duan, Xueping Wu, Xiujuan Zhuang, Hong Zhou, Qinglin Zhang, Xiaoli Zhu, Wei Hu, Pinyun Ren, Pengfei Guo, Liang Ma, Xiaopeng Fan, Xiaoxia Wang, Jinyou Xu, Anlian Pan, and Xiangfeng Duan. Growth of Alloy MoS2xSe2(1–x) Nanosheets with Fully Tunable Chemical Compositions and Optical Properties. *Journal of the American Chemical Society*, 136(10):3756–3759, February 2014.

[68] Yao Li, Karel-Alexander N Duerloo, Kerry Wauson, and Evan J Reed. Structural Semiconductor-to-Semimetal Phase Transition in Two-Dimensional Materials Induced by Electrostatic Gating. January 2016.

[69] Yilei Li, Yi Rao, Kin Fai Mak, YuMeng You, Shuyuan Wang, Cory R Dean, and Tony F Heinz. Probing Symmetry Properties of Few-Layer MoS2 and h-BN by Optical Second-Harmonic Generation. *Nano Letters*, 13(7):3329–3333, June 2013.

[70] Yilei Li, Alexey Chernikov, Xian Zhang, Albert Rigosi, Heather M Hill, Arend M van der Zande, Daniel A Chenet, En-Min Shih, James Hone, and Tony F Heinz. Measurement of the optical dielectric function of monolayer transition-metal dichalcogenides: MoS2, MoSe2, WS2, and WSe2. *Physical Review B*, 90(20):205422, November 2014.

[71] Der Yuh Lin, Tung Pai Huang, Fan Lei Wu, Chih Ming Lin, Ying Sheng Huang, and Kwong Kau Tiong. Anisotropy of Photoluminescence in Layered Semiconductors ReS2 and ReS2:Au. *Solid State Phenomena*, 170:135–138, March 2011.

[72] Yung-Chang Lin, Dumitru O Dumcenco, Ying Sheng Huang, and Kazu Suenaga. Atomic mechanism of the semiconducting-to-metallic phase transition in single-layered

MoS2. *Nature nanotechnology*, 9(5):391–396, May 2014.

[73] Chang-Hua Liu, In Soo Kim, and Lincoln J Lauhon. Optical Control of Mechanical Mode-Coupling within a MoS2 Resonator in the Strong-Coupling Regime. *Nano Letters*, 15(10):6727–6731, September 2015.

[74] Erfu Liu, Yajun Fu, Yaojia Wang, Yanqing Feng, Huimei Liu, Xiangang Wan, Wei Zhou, Baigeng Wang, Lubin Shao, Ching-Hwa Ho, Ying Sheng Huang, Zhengyi Cao, Laiguo Wang, Aidong Li, Junwen Zeng, Fengqi Song, Xinran Wang, Yi Shi, Hongtao Yuan, Harold Y Hwang, Yi Cui, Feng Miao, and Dingyu Xing. Integrated digital inverters based on two-dimensional anisotropic ReS2 field-effect transistors. *Nature Communications*, 6:6991, May 2015.

[75] Kai Liu, Qimin Yan, Michelle Chen, Wen Fan, Yinghui Sun, Joonki Suh, Deyi Fu, Sangwook Lee, Jian Zhou, Sefaattin Tongay, Jie Ji, Jeffrey B Neaton, and Junqiao Wu. Elastic Properties of Chemical-Vapor-Deposited Monolayer MoS2, WS2, and Their Bilayer Heterostructures. *Nano Letters*, 14(9):5097–5103, August 2014.

[76] Keng-Ku Liu, Wenjing Zhang, Yi Hsien Lee, Yu-Chuan Lin, Mu Tung Chang, Ching-Yuan Su, Chia Seng Chang, Hai Li, Yumeng Shi, Hua Zhang, Chao-Sung Lai, and Lain-Jong Li. Growth of Large-Area and Highly Crystalline MoS2 Thin Layers on Insulating Substrates. *Nano Letters*, 12(3):1538–1544, March 2012.

[77] Tony Low, Michael Engel, Mathias Steiner, and Phaedon Avouris. Origin of photoresponse in black phosphorus phototransistors. *Physical Review B*, 90(8):081408, August 2014.

[78] Kin Fai Mak, Matthew Y Sfeir, Yang Wu, Chun Hung Lui, James A Misewich, and Tony F Heinz. Measurement of the Optical Conductivity of Graphene. *Physical Review Letters*, 101(19):196405, November 2008.

[79] Kin Fai Mak, Changgu Lee, James Hone, Jie Shan, and Tony F Heinz. Atomically Thin MoS2: A New Direct-Gap Semiconductor. *Physical Review Letters*, 105(13):136805, September 2010.

[80] Kin Fai Mak, Keliang He, Jie Shan, and Tony F Heinz. Control of valley polarization in monolayer MoS2 by optical helicity. *Nature nanotechnology*, 7(8):494–498, August 2012.

[81] Kin Fai Mak, Keliang He, Jie Shan, and Tony F Heinz. Control of valley polarization in monolayer MoS2 by optical helicity. *Nature nanotechnology*, 7(8):494–498, August 2012.

[82] Kin Fai Mak, Keliang He, Changgu Lee, Gwan-Hyoung Lee, James Hone, Tony F Heinz, and Jie Shan. Tightly bound trions in monolayer MoS2. *Nature materials*, 12 (3):207–211, March 2013.

[83] M Massicotte, P Schmidt, F Vialla, K G Schädler, A Reserbat-Plantey, K Watanabe, T Taniguchi, K J Tielrooij, and F H L Koppens. Picosecond photoresponse in van der Waals heterostructures. *Nature nanotechnology*, 11(1):42–46, January 2016.

[84] Mathieu Massicotte, Peter Schmidt, Fabien Vialla, Kenji Watanabe, Takashi Taniguchi, Klaas-Jan Tielrooij, and Frank H L Koppens. Photo-thermionic effect in vertical graphene heterostructures. January 2016.

[85] Shahriar Memaran, Nihar R Pradhan, Zhengguang Lu, Daniel Rhodes, Jonathan Ludwig, Qiong Zhou, Omotola Ogunsolu, Pulickel M Ajayan, Dmitry Smirnov, Antonio I Fernández-Domínguez, Francisco J García-Vidal, and Luis Balicas. Pronounced Photovoltaic Response from Multilayered Transition-Metal Dichalcogenides PN-Junctions. *Nano Letters*, 15(11):7532–7538, November 2015.

[86] K Momma and F Izumi. VESTA 3 for three-dimensional visualization of crystal, volumetric and morphology data. *Journal of Applied Crystallography*, 2011.

[87] Sina Najmaei, Zheng Liu, Wu Zhou, Xiaolong Zou, Gang Shi, Sidong Lei, Boris I Yakobson, Juan-Carlos Idrobo, Pulickel M Ajayan, and Jun Lou. Vapour phase growth and grain boundary structure of molybdenum disulphide atomic layers. *Nature materials*, 12(8):754–759, August 2013.

[88] K S Novoselov, A K Geim, S V Morozov, D Jiang, M I Katsnelson, I V Grigorieva,

S V Dubonos, and A A Firsov. Two-dimensional gas of massless Dirac fermions in graphene. *Nature*, 438(7065):197–200, November 2005.

[89] K S Novoselov, D Jiang, T Booth, V V Khotkevich, S M Morozov, and A K Geim. Two Dimensional Atomic Crystals. *Proc. Natl. Acad. Sci. U. S. A.*, 102(cond-mat/0503533): 10451. 4 p, March 2005.

[90] J I Pankove. *Optical Processes in.* Semiconductors, 1971.

[91] Sokrates T Pantelides. The electronic structure of impurities and other point defects in semiconductors. *Reviews of Modern Physics*, 50(4):797–858, October 1978.

[92] S Perkowitz. Optical characterization of semiconductors: infrared, Raman, and photoluminescence spectroscopy, 2012.

[93] Andreas Pospischil, Marco M Furchi, and Thomas Mueller. Solar-energy conversion and light emission in an atomic monolayer p-n diode. *Nature nanotechnology*, 9(4): 257–261, April 2014.

[94] Hao Qiu, Lijia Pan, Zongni Yao, Junjie Li, Yi Shi, and Xinran Wang. Electrical characterization of back-gated bi-layer MoS2 field-effect transistors and the effect of ambient on their performances. *Applied Physics Letters*, 100(12):123104, March 2012.

[95] B Radisavljevic, A Radenovic, J Brivio, V Giacometti, and A Kis. Single-layer MoS2 transistors. *Nature nanotechnology*, 6(3):147–150, March 2011.

[96] Alex W Robertson, Alicja Bachmatiuk, Yimin A Wu, Franziska Schäffel, Bernd Rellinghaus, Bernd Büchner, Mark H Rümmeli, and Jamie H Warner. Atomic Structure of Interconnected Few-Layer Graphene Domains. *ACS Nano*, 5(8):6610–6618, August 2011.

[97] Jason S Ross, Philip Klement, Aaron M Jones, Nirmal J Ghimire, Jiaqiang Yan, D G Mandrus, Takashi Taniguchi, Kenji Watanabe, Kenji Kitamura, Wang Yao, David H Cobden, and Xiaodong Xu. Electrically tunable excitonic light-emitting diodes based on monolayer WSe2 p-n junctions. *Nature nanotechnology*, 9(4):268–272, April 2014.

[98] Claudia Ruppert, Ozgur Burak Aslan, and Tony F Heinz. Optical Properties and

Band Gap of Single- and Few-Layer MoTe2 Crystals. *Nano Letters*, 14(11):6231–6236, October 2014.

[99] Claudia Ruppert, Ozgur Burak Aslan, and Tony F Heinz. Optical Properties and Band Gap of Single- and Few-Layer MoTe2 Crystals. *Nano Letters*, 14(11):6231–6236, October 2014.

[100] H Sahin, S Tongay, S Horzum, W Fan, J Zhou, J Li, J Wu, and F Peeters. Anomalous Raman spectra and thickness-dependent electronic properties of WSe2. *Physical Review B*, 87(16):165409, April 2013.

[101] Deblina Sarkar, Xuejun Xie, Wei Liu, Wei Cao, Jiahao Kang, Yongji Gong, Stephan Kraemer, Pulickel M Ajayan, and Kaustav Banerjee. A subthermionic tunnel field-effect transistor with an atomically thin channel. *Nature*, 526(7571):91–95, October 2015.

[102] Emilio Scalise, Michel Houssa, Geoffrey Pourtois, Valery Afanas'ev, and André Stesmans. Strain-induced semiconductor to metal transition in the two-dimensional honeycomb structure of MoS2. *Nano Research*, 5(1):43–48, 2012.

[103] Alexey A Soluyanov, Dominik Gresch, Zhijun Wang, QuanSheng Wu, Matthias Troyer, Xi Dai, and B Andrei Bernevig. Type-II Weyl semimetals. *Nature*, 527(7579):495–498, November 2015.

[104] Andrea Splendiani, Liang Sun, Yuanbo Zhang, Tianshu Li, Jonghwan Kim, Chi-Yung Chim, Giulia Galli, and Feng Wang. Emerging Photoluminescence in Monolayer MoS2. *Nano Letters*, 10(4):1271–1275, March 2010.

[105] Yan Sun, Shu-Chun Wu, Mazhar N Ali, Claudia Felser, and Binghai Yan. Prediction of Weyl semimetal in orthorhombic MoTe2. *Physical Review B*, 92(16):161107, October 2015.

[106] R Suzuki, M Sakano, Y J Zhang, R Akashi, D Morikawa, A Harasawa, K Yaji, K Kuroda, K Miyamoto, T Okuda, K Ishizaka, R Arita, and Y Iwasa. Valley-dependent spin polarization in bulk MoS2 with broken inversion symmetry. *Nature nanotechnol-*

ogy, 9(8):611–617, August 2014.

[107] Jin Chong Tan and Anthony K Cheetham. Mechanical properties of hybrid inorganic–organic framework materials: establishing fundamental structure–property relationships. *Chemical Society Reviews*, 40(2):1059–1080, 2011.

[108] M Tinkham. Group theory and quantum mechanics, 2003.

[109] T Tite, C J Lee, and Y M Chang. Polarization Raman spectroscopy of GaN nanorod bundles. *Journal of Applied Physics*, 108(3):033504, August 2010.

[110] Sefaattin Tongay, Hasan Sahin, Changhyun Ko, Alex Luce, Wen Fan, Kai Liu, Jian Zhou, Ying Sheng Huang, Ching-Hwa Ho, Jinyuan Yan, D Frank Ogletree, Shaul Aloni, Jie Ji, Shushen Li, Jingbo Li, F M Peeters, and Junqiao Wu. Monolayer behaviour in bulk ReS2 due to electronic and vibrational decoupling. *Nature Communications*, 5, February 2014.

[111] Adam W Tsen, Lola Brown, Mark P Levendorf, Fereshte Ghahari, Pinshane Y Huang, Robin W Havener, Carlos S Ruiz-Vargas, David A Muller, Philip Kim, and Jiwoong Park. Tailoring Electrical Transport Across Grain Boundaries in Polycrystalline Graphene. *Science*, 336(6085):1143–1146, June 2012.

[112] Arend M van der Zande, Pinshane Y Huang, Daniel A Chenet, Timothy C Berkelbach, YuMeng You, Gwan-Hyoung Lee, Tony F Heinz, David R Reichman, David A Muller, and James C Hone. Grains and grain boundaries in highly crystalline monolayer molybdenum disulphide. *Nature materials*, 12(6):554–561, June 2013.

[113] Arend M van der Zande, Jens Kunstmann, Alexey Chernikov, Daniel A Chenet, YuMeng You, XiaoXiao Zhang, Pinshane Y Huang, Timothy C Berkelbach, Lei Wang, Fan Zhang, Mark S Hybertsen, David A Muller, David R Reichman, Tony F Heinz, and James C Hone. Tailoring the Electronic Structure in Bilayer Molybdenum Disulfide via Interlayer Twist. *Nano Letters*, 14(7):3869–3875, June 2014.

[114] R van Leeuwen, A Castellanos-Gomez, G A Steele, H S J van der Zant, and W J Venstra. Time-domain response of atomically thin MoS2 nanomechanical resonators.

Applied Physics Letters, 105(4):041911, July 2014.

[115] Han Wang, Xiaomu Wang, Fengnian Xia, Luhao Wang, Hao Jiang, Qiangfei Xia, Matthew L Chin, Madan Dubey, and Shu-jen Han. Black Phosphorus Radio-Frequency Transistors. *Nano Letters*, 14(11):6424–6429, November 2014.

[116] L Wang, I Meric, P Y Huang, Q Gao, Y Gao, H Tran, T Taniguchi, K Watanabe, L M Campos, D A Muller, J Guo, P Kim, J Hone, K L Shepard, and C R Dean. One-Dimensional Electrical Contact to a Two-Dimensional Material. *Science*, 342(6158): 614–617, November 2013.

[117] J C Wildervanck and F Jellinek. The dichalcogenides of technetium and rhenium. *Journal of the Less Common Metals*, 24(1):73–81, May 1971.

[118] Daniel Wolverson, Simon Crampin, Asieh S Kazemi, Adelina Ilie, and Simon J Bending. Raman Spectra of Monolayer, Few-Layer, and Bulk ReSe2: An Anisotropic Layered Semiconductor. *ACS Nano*, 8(11):11154–11164, November 2014.

[119] Juanxia Wu, Nannan Mao, Liming Xie, Hua Xu, and Jin Zhang. Identifying the Crystalline Orientation of Black Phosphorus Using Angle-Resolved Polarized Raman Spectroscopy. *Angewandte Chemie*, 127(8):2396–2399, February 2015.

[120] Sanfeng Wu, Jason S Ross, Gui-Bin Liu, Grant Aivazian, Aaron Jones, Zaiyao Fei, Wenguang Zhu, Di Xiao, Wang Yao, David Cobden, and Xiaodong Xu. Electrical tuning of valley magnetic moment through symmetry control in bilayer MoS2. *Nature Physics*, 9(3):149–153, March 2013.

[121] Wenzhuo Wu, Lei Wang, Yilei Li, Fan Zhang, Long Lin, Simiao Niu, Daniel Chenet, Xian Zhang, Yufeng Hao, Tony F Heinz, James Hone, and Zhong Lin Wang. Piezoelectricity of single-atomic-layer MoS2 for energy conversion and piezotronics. *Nature*, 514(7523):470–474, October 2014.

[122] Fengnian Xia, Han Wang, and Yichen Jia. Rediscovering black phosphorus as an anisotropic layered material for optoelectronics and electronics. *Nature Communications*, 5, July 2014.

[123] Mahito Yamamoto, Sheng Tsung Wang, Meiyan Ni, Yen-Fu Lin, Song-Lin Li, Shinya Aikawa, Wen-Bin Jian, Keiji Ueno, Katsunori Wakabayashi, and Kazuhito Tsukagoshi. Strong Enhancement of Raman Scattering from a Bulk-Inactive Vibrational Mode in Few-Layer MoTe2. *ACS Nano*, 8(4):3895–3903, March 2014.

[124] Zongyou Yin, Hai Li, Hong Li, H Li, Lin Jiang, Yumeng Shi, Yinghui Sun, Gang Lu, Qing Zhang, Xiaodong Chen, and Hua Zhang. Single-Layer MoS2 Phototransistors. *ACS Nano*, 6(1):74–80, December 2011.

[125] Youngki Yoon, Kartik Ganapathi, and Sayeef Salahuddin. How Good Can Monolayer MoS2 Transistors Be? *Nano Letters*, 11(9):3768–3773, August 2011.

[126] Woo Jong Yu, Yuan Liu, Hailong Zhou, Anxiang Yin, Zheng Li, Yu Huang, and Xiangfeng Duan. Highly efficient gate-tunable photocurrent generation in vertical heterostructures of layered materials. *Nature nanotechnology*, 8(12):952–958, December 2013.

[127] Hualing Zeng, Junfeng Dai, Wang Yao, Di Xiao, and Xiaodong Cui. Valley polarization in MoS2 monolayers by optical pumping. *Nature nanotechnology*, 7(8):490–493, August 2012.

[128] Yongjie Zhan, Zheng Liu, Sina Najmaei, Pulickel M Ajayan, and Jun Lou. Large-Area Vapor-Phase Growth and Characterization of MoS2 Atomic Layers on a SiO2 Substrate. *Small*, 8(7):966–971, April 2012.

[129] Haitao Zhang, Don-Hyung Ha, Robert Hovden, Lena Fitting Kourkoutis, and Richard D Robinson. Controlled Synthesis of Uniform Cobalt Phosphide Hyperbranched Nanocrystals Using Tri-n-octylphosphine Oxide as a Phosphorus Source. *Nano Letters*, 11(1):188–197, December 2010.

[130] Wenjing Zhang, Jing-Kai Huang, Chang Hsiao Chen, Yung-Huang Chang, Yuh Jen Cheng, and Lain-Jong Li. High-Gain Phototransistors Based on a CVD MoS2 Monolayer. *Advanced Materials*, 25(25):3456–3461, July 2013.

[131] Hanyu Zhu, Yuan Wang, Jun Xiao, Ming Liu, Shaomin Xiong, Zi Jing Wong, Ziliang

Ye, Yu Ye, Xiaobo Yin, and Xiang Zhang. Observation of piezoelectricity in free-standing monolayer MoS2. *Nature nanotechnology*, 10(2):151–155, February 2015.

[132] Weinan Zhu, Maruthi N Yogeesh, Shixuan Yang, Sandra H Aldave, Joon-Seok Kim, Sushant Sonde, Li Tao, Nanshu Lu, and Deji Akinwande. Flexible Black Phosphorus Ambipolar Transistors, Circuits and AM Demodulator. *Nano Letters*, 15(3):1883–1890, March 2015.

[133] Xiaolong Zou, Yuanyue Liu, and Boris I Yakobson. Predicting Dislocations and Grain Boundaries in Two-Dimensional Metal-Disulfides from the First Principles. *Nano Letters*, 13(1):253–258, December 2012.